

Stability and Solvation Properties of Organosilicon Electrolytes for Lithium-Ion Batteries

By

Sarah Lucienne Guillot

A dissertation submitted in partial fulfillment of
the requirements for the degree of

Doctor of Philosophy

(Chemistry)

at the

UNIVERSITY OF WISCONSIN-MADISON

2019

Date of final oral examination: 3/3/2019

The dissertation is approved by the following members of the Final Oral Committee:

Robert J. Hamers, Professor, Chemistry
Kyoung-Shin Choi, Professor, Chemistry
Clark Landis, Professor, Chemistry
Charles Fry, Staff, Chemistry

Stability and Solvation Properties of Organosilicon Electrolytes for Lithium-Ion Batteries

Sarah Lucienne Guillot

Under the Supervision of Professor Robert J. Hamers

University of Wisconsin-Madison

Abstract

Lithium-ion batteries are increasingly used for energy storage today due to their excellent energy capacity and voltage characteristics. However, the limited window of electrochemical stability for conventional carbonate-based lithium-ion battery electrolytes constrains the development of devices with higher voltages and longer lifetimes. One method used to achieve desirable electrolyte performance is through mixing multiple electrolyte solvents with different properties; however, increasing solution complexity can lead to unexpected synergies and an inadequate functional understanding of the solution components. Therefore, innovating electrolyte systems with increased thermal and electrochemical stability, and understanding the nature of solvent behavior in mixed electrolytes, are relevant issues in battery development.

Organosilicon solvents for battery electrolytes, developed by Silatronix, Inc. with the University of Wisconsin-Madison, have demonstrated improved oxidative stability, reduced gassing, and increased thermal stability. This dissertation investigates the mechanisms and structure-function relationships between organosilicon solvents for lithium-ion batteries and their superior thermal and electrochemical stability, in addition to quantifying competitive solvation in mixed organosilicon-carbonate electrolytes.

We studied a series of organosilicon electrolytes with differing nitrile, glycol, and fluorine functional substituents to understand the structural origins of thermal stability. The thermal and hydrolytic stability of organosilicon and carbonate solvents with LiPF_6 was probed by storage at high temperatures and with added water. Quantitative monitoring of organosilicon and carbonate electrolyte decomposition products over time using Nuclear Magnetic

Resonance (NMR) spectroscopy revealed mechanisms of degradation and led to the discovery of a key PF₅-complex that forms in organosilicon electrolytes to inhibit further salt breakdown.

Next, we investigated organosilicon nitrile-based electrolytes for lithium-ion batteries at highly anodic potentials to gain a mechanistic understanding of electrochemical stability. Voltammetry shows superior intrinsic oxidative stability of electrolytes with organosilicon nitrile solvents compared to carbonate solvents against inert platinum electrodes. Studies on a series of nonfluorinated to trifluorinated organosilicon nitriles demonstrate that fluorination at the silicon atom decreases the electrolyte oxidation potential. Density functional theory (DFT) calculations, NMR spectroscopy, and x-ray photoelectron spectroscopy (XPS) analyses were used to determine the mechanisms of stability and understand the trend of fluorination and oxidation potential. DFT and NMR showed that the preferred oxidation pathway is a coupled fluorination-oxidation resulting in Si-C bond cleavage to form a fluorosilane in solution, and XPS showed that a thin (<4 nm) nitrogen-containing surface film forms simultaneously. Our results suggest a self-limited surface film forms at moderate oxidizing potentials in organosilicon nitriles that inhibits further oxidation and enables high-potential stability.

Finally, we investigated the nature of lithium solvation in organosilicon (OSN) and mixed OSN-ethylene carbonate (EC) and OSN-diethyl carbonate (DEC) electrolytes. DFT, FTIR, and NMR were used to analyze how the degree of lithium coordination of each solvent changes with the addition of a second solvent species, and to begin to quantitate the degree of lithium solvation and percentage of each solvent component involved in the solvation shell. The relative degree of ionic dissociation in different electrolyte mixtures was also calculated through diffusion NMR measurements. The FTIR and NMR results agreed that the carbonate composes a greater fraction of the solvation shell than the organosilicon in binary electrolytes, with EC a strong majority in the solvation shell (63% in 1:1 mol:mol EC:OSN) and DEC sharing the solvation shell more with OSN (57% DEC in 1:1 mol:mol DEC:OSN). Despite a

lower solvation shell contribution, OSN is still present in the solvation shell (5-8%) even when only 9 mol% of the solution composition. Furthermore, addition of OSN to the carbonate electrolytes increases ionic dissociation and decreases the solvation number, showing that OSN has a significant impact on the solvation properties. These studies unveil the subtleties of analyzing even simple electrolyte solutions and provide a foundation of techniques and solvation structure that can be used in understanding electrolyte systems of greater complexity and application.

This work advances the fundamental understanding of novel organosilicon-containing lithium-ion electrolytes, to enable their use in high-performance batteries, and the rational design of future ultra-stable functional organosilicon solvents and additives.

Acknowledgements

A PhD thesis represents the work of one person, supported and boosted and led by hundreds of hands. It takes a village to raise a dissertation. It's impossible to distill down to a few pages all the gratitude I have for the people who helped me get to where I am, but I'll do my best!

My family has been a constant source of support, love, and advice throughout my life. Thank you to Mom, Dad, and Rachel for teaching me that it's okay to do things that other people would think are crazy. Thank you for late night phone calls about Big Life Decisions, for amazing trips to Scandinavia and to Door County, for traveling to cheer me on at Nationals, and for being here with me to celebrate my PhD. It means so much to me to get to share these moments with you. Thank you for the best hugs, goofy big grins, and for being the role models that I aspire to be and to make proud. Rachel: thank you for being the perfect big sister and my best friend and the awesomest most amazing person I know. Phone calls from you while you're stuck in 5 mph traffic are the best, and you will always be my favorite running partner.

To Bob, thank you for your belief in me. More than anything else I think that helped me get through the hills and valleys of this dissertation journey. Thank you for achieving the perfect balance of mentoring support and freedom. Thank you for your positivity and excitement about science, and all your advice and guidance on research and life. I have really enjoyed being part of your research group the past five years, and I can't imagine having done this with anyone else as an advisor.

I have been incredibly, astonishingly fortunate in mentors in my science career. I have so much gratitude for their generosity, thoughtfulness, and support; they have literally shaped my life. Stewart Williamson, I think my chemistry career really started the first day of high school chemistry when I watched you climb the classroom wall whilst describing adhesion and cohesion. Thank you for introducing me to this world. Chris Goh, you made a deep and lasting impact on a young scientist, the extent of which I'm still discovering today. Not only are your lessons things that I will remember and use throughout but life, but the scientist and person you are inspires me to live my own life in a way that will make the world and people around me better. To all the chemistry faculty at Williams College, especially Sarah Goh, David Richardson, and Lee Y. Park, thank you for the guidance you've given me, as well as the caring and rich learning environment you have created. Jeff Blackburn, thank you for putting me on the path of a career in sustainable energy and helping me to transition from a student researcher to a more independent scientist. Also for beer-in-hand kickball leagues and science meetings while watching the World Cup.

A huge thank you to everyone at Silatronix: you made my PhD possible. Thank you to Deb Gilbert for your guidance and kindness. You are a truly inspiring role model. Last but not most, thank you to Monica Usrey and Adrián Peña-Hueso. You have taught me so much. Many of my favorite science moments from the past five years are our discussions, usually filled with lots of laughter but also brilliant breakthroughs. It's been an honor and a learning experience to work with two people who are so smart, so passionate, and so accomplished.

Oh, the Hamers Group. You are simply the best. From terrace outings to whiteboard science to trivia and rope courses, I have had the most fun with you. I am constantly impressed with the level of kindness and support within our group. Thank you to all the former Hamers Group members, you were great role models and mentors. Special thanks to the old battery vanguard Shuyu Fang and Laura Slaymaker, and the new battery cadre Zhifei Li and Louis

Morris. Thank you to Arielle Mensch, for continuing to be an awesome friend and mentor even after graduating! (I have your thesis open right now for inspiration as I write.) Here's to the Dream Beam Team, the Foggy Goggles, the Yellow Paiges, and Graphs; Offices 3341 and 3335(a and b). (Thank you to 3335a for letting me interject comments randomly from the inner office.) Thank you to Liz, Jaya, Zack, and Paige. You make me laugh and think deeply and inspire me on a daily basis. Thank you for being a bright part of every day, and for really fun dinner parties. Especially to the lovely Jaya, thank you for countless occasions of sharing your soul and letting me share mine.

To Kelly, I love you. You have been by my side (literally, my eternal desk neighbor) through this whole journey, and just seeing your face makes me happy to be at work. It breaks my heart a little that we will be leaving each other soon, but I'm really excited for the next chapter in your career because you are the most amazing scientist I know, and the most beautiful person. I can't wait to see what you achieve.

For my favorite Ephs, a million thanks for late nights at Schow and rooftop adventures. Michael and Peter, my first-year adventure buddies in chemistry and beyond. Olivia, Maddie, and Alex, for so many things but to name a few, Senior Year C2C and the magnificent, magical Mustachioed Animals. Erica, best friends and bridesmaids and roomies forever, you are the best person to be on a 'Free Cuddlez' poster with and I'm very excited for your badass lawyer career. Dr. Menghan, thank you for some of the best photos of my college years, for your kindness and silliness and loveliness, and for the opportunity to be part of objectively the most fun wedding ever.

The Wisconsin Triathlon Team has been a big part of my life the past 5 years. I think I would have a little (more) crazy if I hadn't been able to escape the chemistry building occasionally to go for 60 mile bike rides to Blue Mounds, swim across Devil's Lake and back, and run every weekend with the dedicated Saturday Morning Run Crew. Special kudos and gratitude to Jumana and Allie, you are amazing and inspiring and my time with you at practices and beyond has been so very special. Gracias a Pedro, el Chileno, el tiburón, mi compañero de capitanear Ragnar, por estar a mi lado cuando nadé, corrí, y ciclé lo más largo que nunca, y por inspirarme con tu indómito espíritu de Ironman. Thank you also to Coach TK's Movin' Shoes Track Club, especially my group 2 comrades! There's no one I'd rather do a brutal 3 sets of double-800s with!

Thank you Rachel, Steph, and Evan, the most brilliant trivia masters and Golden Globe ballot winners, for showing me how to do a PhD right and letting me be part of the cutest proposal ever. Thank you Rachel for being my very first new friend in Madison and an awesome roommate, and Steph and Evan for an unforgettable trip to Colorado (reunion trip someday??) and many discussions of triathlon and baking.

To Cari, my potato-loving breeder, job-search twin, workout buddy, support system: what a journey, right? It's too bad we both got jobs and won't be able to go bike touring through Europe together. ☺ Someday! I love you and I'm incredibly proud and excited for you to start the next chapter as I do! Lean in, plant down, grow up.

To Devlin, thank you for being the most supportive and lovely boyfriend I could ask for, and especially for hours upon hours of Great British Bakeoff, very very delicious foods, and so many passionate movie discoveries and discussions.

Table of Contents

Abstract.....	i
Acknowledgements.....	iv
Table of Contents.....	vi
Chapter 1: Background and Introduction.....	1
1.1 Lithium-ion battery overview.....	1
1.2 Electrolytes for lithium-ion batteries.....	3
1.2.1 Thermal stability of electrolytes.....	5
1.2.2 Electrochemical stability of electrolytes.....	6
1.3 Organosilicon electrolytes for lithium-ion batteries.....	7
1.4 Scope of thesis.....	8
1.5 References.....	11
Chapter 2. Thermal and hydrolytic decomposition mechanisms of organosilicon electrolytes with enhanced thermal stability for lithium-ion batteries.....	14
2.1 Introduction.....	14
2.2 Materials and Methods.....	16
2.2.1 Chemicals.....	16
2.2.2 Thermal stability and NMR analysis.....	16
2.3 Results and Discussion.....	17
2.3.1 Organosilicon electrolytes decomposition.....	18
2.3.2 Carbonate electrolytes decomposition.....	31
2.4 Conclusion.....	33
2.5 Figures.....	35
2.6 References.....	54
Chapter 3. Mechanistic Insights into High Oxidative Stability of Organosilicon Nitrile Electrolytes for Lithium-ion Batteries.....	58
3.1 Introduction.....	58
3.2 Materials and Methods.....	60
3.2.1 Chemicals.....	60
3.2.2 DFT Calculation Methods.....	60
3.2.3 Electrochemical tests.....	61
3.2.4 Nuclear Magnetic Resonance (NMR) Spectroscopy.....	61
3.2.5 X-ray Photoelectron Spectroscopy (XPS).....	62
3.3 Results and Discussion.....	62

3.3.1 Computation of organosilicon oxidation potentials.....	62
3.3.2 Linear Sweep Voltammetry analysis.....	65
3.3.3 Voltage hold analysis of oxidation degradation mechanisms	65
3.3.4 Electrode surface species analysis by XPS.....	66
3.4 Conclusions	71
3.5 Figures.....	76
3.6 References	95
Chapter 4. Competitive Solvation in Mixed Organosilicon and Carbonate Electrolytes	100
4.1 Introduction	100
4.2 Materials and Methods	101
4.2.1 Chemicals	101
4.2.2 Fourier Transform Infrared Spectroscopy (FTIR).....	101
4.2.3 Nuclear Magnetic Resonance (NMR) Spectroscopy.....	102
4.2.4 DFT calculation methods.....	103
4.3 Results and discussion.....	103
4.3.1 Computation	103
4.3.2 ⁶ Li- NMR assessment of the solvation sphere.....	106
4.3.3 Calculation of Ionic Dissociation	108
4.3.4 Fourier transform infrared spectroscopy qualitative analysis of solvation.....	110
4.3.4 Fourier transform infrared spectroscopy quantitative analysis of solvation.....	113
4.4 Conclusions	116
4.5 Figures.....	119
4.6 References	134
Chapter 5. Conclusions and Future Directions	137

Chapter 1: Background and Introduction

1.1 Lithium-ion battery overview

As the energy storage needs of today's society increase, there is a corresponding need for the development of higher-power, longer-lasting, more stable battery technologies. Lithium-ion batteries (LIBs) are currently the technology of choice to meet the majority of the energy needs for mobile electronics¹⁻² and electric vehicles²⁻³ due to their high potentials and high gravimetric capacity.⁴ The first announcement of commercial lithium-ion technology was by Sony in 1991,^{2,5-6} and since then has been adopted world-wide.

Lithium-ion batteries are secondary (reversible) batteries that operate by establishing a potential gradient due to the intrinsic chemical potential difference between two solid materials (electrodes) separated by a lithium-ion-conducting material (electrolyte). In the discharging state, the negative electrode (defined in LIBs as the anode) will undergo oxidation, releasing lithium into the electrolyte and passing electrons through the current collector into an electrical connection. Lithium is transported to the positive electrode (cathode) through the electrolyte, concurrent with the transport of electrons from the anode electrode externally through an electrical circuit. The movement of these electrons from the anode produce electrical energy by routing their transport through an electrical load (Figure 1.1). An essential characteristic of LIBs is their ability to reverse this process during charging when an electricity source is supplied, such that the battery can undergo many charge/discharge cycles over a long period of time.

The choice of lithium-ion for many energy needs is motivated by LIBs' high-voltage and high-capacity capabilities, which lead to high energy density cells.⁷ The theoretical voltage of the battery, V_{cell} , is determined by the difference in chemical potentials between the anode and cathode (Equation 1.1).

$$V_{\text{cell}} = V_{\text{cathode}} - V_{\text{anode}} \quad (1.1)$$

The strong reducing power of lithium at -3.04 V vs SHE facilitates the development of high voltage batteries based on lithium chemistry. Today, technological advances have resulted in the development of high-voltage LIBs that operate at 4.5 V vs Li/Li⁺ and above.⁸⁻¹¹ Many energy applications have a need for batteries that have a high energy-to-weight ratio, which is provided by the intrinsically high gravimetric capacity of lithium at 3850 mAh/g.¹² The theoretical capacity of a full battery cell is defined by the amount of charge that can be stored in the limiting electrode through Faraday's Law (Equation 1.2). Here, C_{cell} is the battery capacity in units of mAh/g, z is the number of electrons passing per molecular weight of the cathode material (for electrodes other than lithium metal, this is the stoichiometric amount of lithium in the fully lithiated electrode material), F is Faraday's constant 96485 C mol⁻¹, and m is the molecular weight of the active electrode material in g mol⁻¹.

$$C_{\text{cell}} \text{ (mAh/g)} = \frac{z * F * 1000}{m * 3600} \quad (1.2)$$

Additional important characteristics of the battery are cycle lifetime (ability to withstand capacity, voltage fade over time or over many cycles) and safety (minimization of flammability, reduction of short circuits). For all these properties, the electrolyte plays an integral role in the ultimate battery metrics, performance and safety.

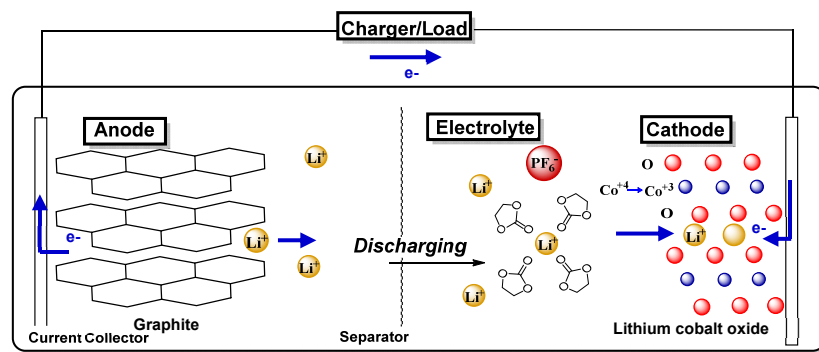
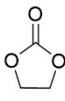
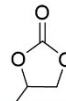
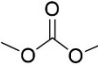
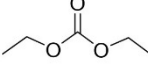
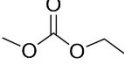


Figure 1.1 Mechanism of electrical energy generation from a discharging lithium-ion battery

1.2 Electrolytes for lithium-ion batteries

The electrolyte has several key characteristics that can determine battery performance. In the solution bulk, the conductivity of an electrolyte is a major factor in the availability of lithium ions to carry and store charge.¹³ The thermal stability of the electrolyte is also an important parameter to consider. High temperatures or small amounts of water result in cascades of catalytic electrolyte degradation processes.¹⁴⁻¹⁵ When the solvated lithium ion reaches an electrode interface, the desolvation energy of the lithium has been determined to be the rate limiting step of lithium intercalation into the graphite anode, in turn limiting battery charging rates.¹⁶ Also at this electrode-electrolyte interface, the electrolyte components are exposed to high electrochemical potentials that lead to solvent and salt degradation, forming surface films that further impact resistivity of lithium intercalation, in addition to resulting in capacity loss from trapped lithium.¹⁷ Therefore, beyond economic considerations, the ideal material properties of lithium-ion battery electrolytes are i) high conductivity; ii) resistance to thermal degradation; and iii) wide electrochemical window of stability.

Table 1.1 Physical and Electrochemical Properties of Cyclic and Linear Carbonates

	Cyclic carbonates		Linear carbonates		
	EC	PC	DMC	DEC	EMC
					
Molecular weight (g/mol)	88.06	102.09	90.08	118.13	104.11
Dielectric constant	90	65	3.1	2.8	3.0
Melting point (°C)	36	-49	5	-74	-53
Flashpoint (°C)	143	138	17	25	23
Density (g/mL)	1.32 ^a	1.20	1.06	0.975	1.01
Viscosity (mPa·s)	1.9 ^a	2.5	0.59	0.65	0.75
E _{ox} (V vs Li/Li ⁺)	+6.2	+6.6	+6.5	+6.7	+6.7
E _{red} (V vs Li/Li ⁺)	0	0	0	0	0

^a40 °C ^b1 M Et₄NBF₄, GC, 5 mV/s, 1 mA/cm² ^c0.65 M Bu₄NBF₄, GC, 5 mV/s, 1 mA/cm²

In commercial lithium ion batteries today, the most common electrolyte system is a combination of linear and cyclic carbonates with lithium hexafluorophosphate (LiPF₆) as the lithium salt. Table 1.1 shows some examples of cyclic and linear carbonates with their corresponding molecular weights, dielectric constants, melting points, flashpoints, densities, oxidation potentials, and reduction potentials. Examples of cyclic carbonates include ethylene carbonate (EC) and propylene carbonate (PC).¹⁸ Linear carbonates can include dimethyl carbonate (DMC), diethyl carbonate (DEC), and ethyl methyl carbonate (EMC). The choice of LiPF₆ as the lithium salt is motivated by its high ionic dissociation and high salt solubility, as well as its stability against corrosion of the aluminum current collector typically used for the cathode.¹⁹

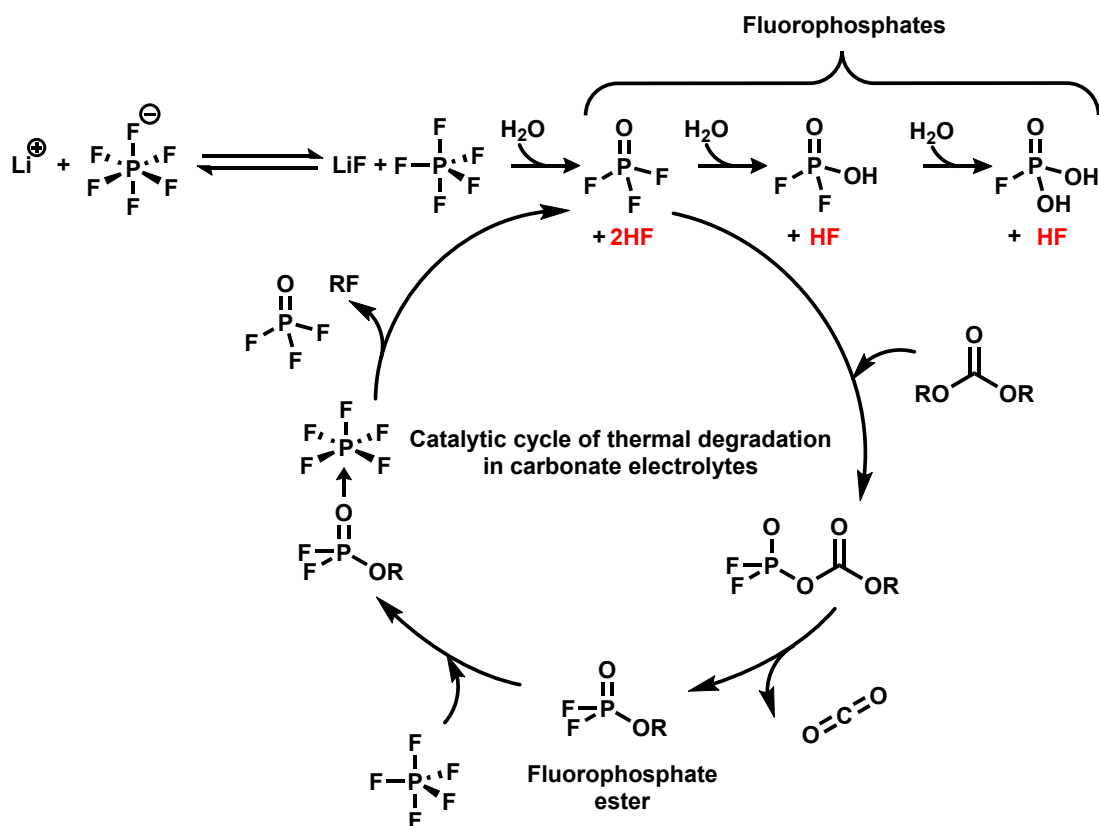


Figure 1.2 Thermal degradation in lithium hexafluorophosphate-carbonate electrolytes

1.2.1 Thermal stability of electrolytes

The thermal stability of LiPF_6 has long been known to be poor in carbonate solvents. At even moderately elevated temperatures, LiPF_6 will dissociate into LiF and PF_5 , the latter a strong Lewis acid that reacts with trace amounts of water and initiates a catalytic cycle of degradation that produces HF , alkyl fluorides, fluorophosphates, fluorophosphate esters, and gases such as ethylene and carbon dioxide (Figure 1.2).^{15,20-21}

The poor thermal stability LiPF_6 is a major concern in battery performance and safety for several reasons: i) the loss of capacity due to the irreversible trapping of lithium as insoluble LiF ;²²⁻
²³ ii) HF -induced degradation of the metal oxide cathode;²⁴⁻²⁵ and iii) the danger of gaseous products within the battery cell due to the potential for explosion in combination with a flammable

electrolyte.²⁶⁻²⁸ *Therefore, there is a need for electrolytes or electrolyte additives that can mitigate the thermal degradation of LiPF₆.*

1.2.2 Electrochemical stability of electrolytes

The theoretical voltage of the battery is determined by the difference in chemical potentials between the anode and cathode. Due to the desire for high-voltage, high-power battery cells, technological advances have resulted in the continuous increase of cell voltage/development of batteries that operate at 4.5 V vs Li/Li⁺ and above. The operating voltage of the battery is in fact determined by the electrochemical window of stability of the electrolyte.^{17, 29} The windows of electrochemical stability of 6.2-6.7 V shown in Table 1.1 represent the largest possible electrochemical range, against inert glassy carbon or platinum electrodes. In contact with the catalytically active complex metal oxide and layered graphite battery-relevant electrode materials, the onset of oxidation and reduction can occur at lower oxidation or higher reduction potentials.³⁰

The formation of passivating surface layers on the electrodes is therefore essential towards enabling multiple cycles of a battery cell without excessive consumption of solvent and salt in parasitic redox reactions.³¹ The surface layer formed on the anode is termed the Solid-Electrolyte Interphase (SEI), and the layer formed on the cathode is often called the Cathode Electrolyte Interphase (CEI). A multitude of electrolyte additives have been developed with the goal of creating a highly lithium-ion-conducting, electrically-insulating, chemically and mechanically stable SEI.^{13, 32} Some of the most common film-forming additives include vinylene carbonate (VC), fluoroethylene carbonate (FEC), lithium bis(oxalato)borate (LiBOB), and sulfur-containing molecules.^{13, 32} Despite the progress in additive development, the formation of passivating SEI layers is rarely ideal, and parasitic electrolytic reactions have been shown to continue even after the initial SEI formation cycles.³³⁻³⁴ *These results show that to mitigate parasitic, degrading side*

reactions, the development of advanced a high-electrochemical-stability solvents or additives is necessary for the future performance improvements of lithium-ion batteries.

1.3 Organosilicon electrolytes for lithium-ion batteries

Organosilicon solvents have shown promise as enhanced-stability, low-flammability solvents for lithium-ion battery electrolytes. Relative to carbonates, organosilicon-based electrolytes have a wider electrochemical window of stability, higher flash points than linear carbonates, reduced gas evolution, and comparable viscosities and conductivities.³⁵⁻³⁷ In 2007, the start-up company Silatronix, Inc. was developed on the foundation of this organosilicon technology, and all science research on organosilicons since that time has been the product of a continuing collaboration between UW-Madison Chemistry and Silatronix, Inc. Zhang et al. demonstrated that the Si atom in siloxane glycols imparted greater oxidative stability when compared with analogous carbon and germanium molecules (Figure 1.3).²⁵ Moreover, silicon-containing glycols exhibited impressive hydrolytic stability even at 20% v/v added water when a propyl spacer was added between the silicon and electronegative functionality.³⁶ Previous studies showed that organosiloxane (R_3Si-OR) electrolytes exhibit good stability, with only minor decomposition of organosiloxane with 1M $LiPF_6$ up to 100 °C.¹⁷ Yet, some degradation was observed arising from hydrolysis of the Si-O bond. More recent studies showed that increased resistance to hydrolysis could be achieved by introducing a short alkyl linker ($R_3Si(CH_2)_n-OR$) and using LiTFSI instead of $LiPF_6$.³⁶ The prior studies of organosilicon-based electrolytes suggest that the thermal and hydrolytic stability can be improved through changes in the molecular structure.

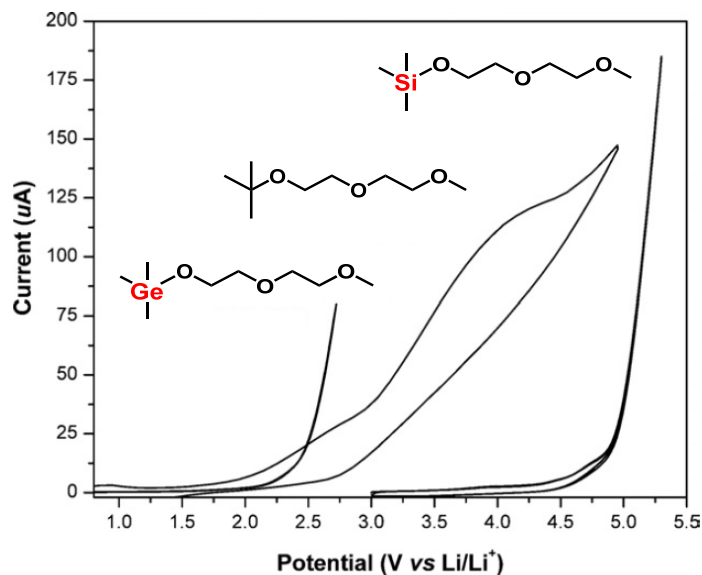


Figure 1.3 Silicon-containing glycol molecules demonstrate higher oxidative stability than their germanium or carbon analogues³⁵

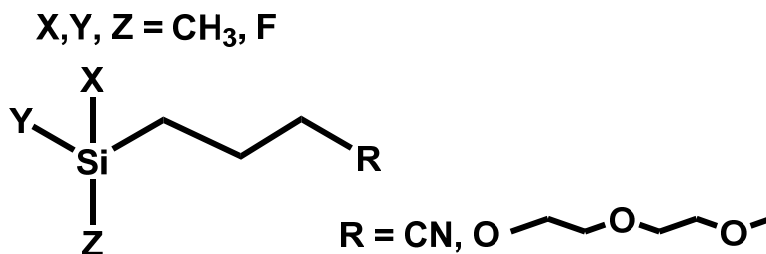


Figure 1.4 Scope of Organosilicon Solvents Studied in this dissertation

1.4 Scope of thesis

The continuing need for high-energy, longer-lasting energy storage is driving the development of new battery materials that can facilitate high-capacity, high-voltage, long-lasting devices while not failing under extreme electrochemical and thermal stresses of these demanding requirements. Organosilicon electrolytes represent a promising new electrolyte system that could

enable the next generation of lithium-ion battery technology. However, the fundamental origin of thermal, electrochemical, and solvation properties of organosilicon-based electrolytes has never been investigated on a molecular level until now.

Chapter 2 explores the structure-function relationship between organosilicon solvents for lithium-ion battery electrolytes and their thermal stability compared with conventional carbonate electrolytes.³⁸ The organosilicon electrolytes studied include molecules with a nitrile or glycol terminal substituent, as well as, within the nitrile-containing molecules, a series of molecules with varying fluorination at the silicon atom. This series of organosilicon solvents, formulated as an electrolyte with 1 M LiPF₆, was used to understand the impact of different molecular moieties on thermal stability. The electrolytes of interest were treated to 100 °C and the thermal degradation species were analyzed and monitored by nuclear magnetic resonance spectroscopy (NMR) over the course of several weeks. The products of thermal degradation were used to map out a mechanism of LiPF₆ thermal protection in organosilicons that explains the superior thermal stability of organosilicon electrolytes relative to carbonate electrolytes.

In Chapter 3, we discuss the electrochemical stability of organosilicon-based electrolytes, and the relationship of this property to the structure of the organosilicon solvent molecule. This study looked at the impact of fluorination at the silicon atom for organosilicon nitrile solvents. Electrochemical properties were assessed with voltammetry, while the molecular origin of the observed electrochemical behavior was determined by a combination of density functional theory (DFT) calculations, NMR analyses of oxidation degradation products, and x-ray photoelectron spectroscopy (XPS) analysis of the electrode surface species. The impact of fluorination at the silicon atom is found to significantly impact the oxidative stability of organosilicon nitriles. Regardless of the degree of fluorination, the oxidative stability of organosilicon electrolytes is

significantly higher than the carbonate electrolyte studied. This high oxidative stability was attributed to the formation of a thin, nitrogen-containing protective electrode surface film at a moderate oxidizing voltage that inhibited further oxidative degradation of the electrolyte.

Chapter 4 covers an investigation of the nature of the lithium solvation sphere in organosilicon-containing electrolytes. We use DFT calculations, Fourier Transform Infrared Spectroscopy (FTIR), and NMR to understand lithium solvation in single solvents (ethylene carbonate [EC], diethyl carbonate [DEC], monofluorinated organosilicon nitrile [1F-OSN]) and how solvation changes in mixed EC/1F-OSN and DEC/1F-OSN electrolytes. These data show that addition of organosilicon to DEC in a mixed electrolyte allows for greater ion dissociation, and solvation of the lithium ion is shared by DEC and 1F-OSN with a greater fraction of DEC. Mixtures of EC and 1F-OSN show EC is more significantly the major component in the solvation shell, but with a solvating fraction of 1F-OSN present even when at <10 mol% of the solution composition. Implications of the organosilicon impact on solvation in mixed solvents and future directions in the correlation between solvation behavior and electrolyte battery performance are discussed.

This dissertation attempts to uncover the structure-function relationships between organosilicon solvents for lithium-ion batteries and their superior thermal and electrochemical stability, and to further combine these findings with studies of mixed-solvent solvation to understand the behavior and impact of organosilicon solvents as single solvent, co-solvent, and additive components of high performance lithium-ion battery electrolytes.

1.5 References

1. Tarascon, J.-M., *Nature* **2001**, 414.
2. Whittingham, M. S., History, Evolution, and Future Status of Energy Storage. *Proceedings of the IEEE* **2012**, 100 (Special Centennial Issue), 1518-1534.
3. Warner, J., 7 - Lithium-Ion Battery Packs for EVs. In *Lithium-Ion Batteries*, Pistoia, G., Ed. Elsevier: Amsterdam, 2014; pp 127-150.
4. Tarascon, J. M.; Armand, M., Issues and challenges facing rechargeable lithium batteries. *Nature* **2001**, 414 (6861), 359-367.
5. Julien, C.; Mauger, A.; Vijn, A.; Zaghbi, K., *Lithium Batteries: Science and Technology*. Springer: 2016.
6. Brandt, K., Historical development of secondary lithium batteries. *Solid State Ionics* **1994**, 69 (3), 173-183.
7. Zubi, G.; Dufo-López, R.; Carvalho, M.; Pasaoglu, G., The lithium-ion battery: State of the art and future perspectives. *Renewable and Sustainable Energy Reviews* **2018**, 89, 292-308.
8. Hu, M.; Pang, X.; Zhou, Z., Recent progress in high-voltage lithium ion batteries. *Journal of Power Sources* **2013**, 237, 229-242.
9. Xu, X.; Deng, S.; Wang, H.; Liu, J.; Yan, H., Research Progress in Improving the Cycling Stability of High-Voltage LiNi_{0.5}Mn_{1.5}O₄ Cathode in Lithium-Ion Battery. *Nano-Micro Letters* **2017**, 9 (2), 22.
10. Su, C.-C.; He, M.; Redfern, P. C.; Curtiss, L. A.; Shkrob, I. A.; Zhang, Z., Oxidatively stable fluorinated sulfone electrolytes for high voltage high energy lithium-ion batteries. *Energy & Environmental Science* **2017**, 10 (4), 900-904.
11. Wang, J.; Yamada, Y.; Sodeyama, K.; Chiang, C. H.; Tateyama, Y.; Yamada, A., Superconcentrated electrolytes for a high-voltage lithium-ion battery. *Nature Communications* **2016**, 7, 12032.
12. Liu, C.; Neale, Z. G.; Cao, G., Understanding electrochemical potentials and cathode materials in rechargeable batteries. *Materials Today* **2016**, 19 (2), 109-123.
13. Xu, K., Electrolytes and Interphases in Li-Ion Batteries and Beyond. *Chemical Reviews* **2014**, 114 (23), 11503-11618.
14. Campion, C. L.; Li, W.; Euler, W. B.; Lucht, B. L.; Ravdel, B.; DiCarlo, J. F.; Gitzendanner, R.; Abraham, K. M., Suppression of Toxic Compounds Produced in the Decomposition of Lithium-Ion Battery Electrolytes. *Electrochemical and Solid-State Letters* **2004**, 7 (7), A194-A197.

15. Campion, C. L.; Li, W.; Lucht, B. L., Thermal Decomposition of LiPF₆-Based Electrolytes for Lithium-Ion Batteries. *Journal of The Electrochemical Society* **2005**, *152* (12), A2327-A2334.
16. Abe, T.; Kawabata, N.; Mizutani, Y.; Inaba, M.; Ogumi, Z., Correlation Between Cointercalation of Solvents and Electrochemical Intercalation of Lithium into Graphite in Propylene Carbonate Solution. *Journal of The Electrochemical Society* **2003**, *150* (3), A257-A261.
17. Goodenough, J. B.; Kim, Y., Challenges for Rechargeable Li Batteries. *Chemistry of Materials* **2010**, *22* (3), 587-603.
18. Ue, M.; Sasaki, Y.; Tanaka, Y.; Morita, M., Nonaqueous Electrolytes with Advanced in Solvents. In *Electrolytes for Lithium and Lithium-Ion Batteries*, Jow, T. R.; Xu, K.; Borodin, O.; Ue, M., Eds. Springer: 2014.
19. Henderson, W. A., Nonaqueous Electrolytes: Advanced in Electrolyte Salts. In *Electrolytes for Lithium and Lithium-Ion Batteries*, Jow, T. R.; Xu, K.; Borodin, O.; Ue, M., Eds. Springer: 2014.
20. Plakhotnyk, A. V.; Ernst, L.; Schmutzler, R., Hydrolysis in the system LiPF₆—propylene carbonate—dimethyl carbonate—H₂O. *Journal of Fluorine Chemistry* **2005**, *126* (1), 27-31.
21. Aurbach, D.; Gamolsky, K.; Markovsky, B.; Salitra, G.; Gofer, Y.; Heider, U.; Oesten, R.; Schmidt, M., The Study of Surface Phenomena Related to Electrochemical Lithium Intercalation into Li_xMO_y Host Materials (M = Ni, Mn). *Journal of The Electrochemical Society* **2000**, *147* (4), 1322-1331.
22. Lin, Y.-X.; Liu, Z.; Leung, K.; Chen, L.-Q.; Lu, P.; Qi, Y., Connecting the irreversible capacity loss in Li-ion batteries with the electronic insulating properties of solid electrolyte interphase (SEI) components. *Journal of Power Sources* **2016**, *309*, 221-230.
23. Sun, Y.; Lee, H.-W.; Zheng, G.; Seh, Z. W.; Sun, J.; Li, Y.; Cui, Y., In Situ Chemical Synthesis of Lithium Fluoride/Metal Nanocomposite for High Capacity Prelithiation of Cathodes. *Nano Letters* **2016**, *16* (2), 1497-1501.
24. Tebbe, J. L.; Holder, A. M.; Musgrave, C. B., Mechanisms of LiCoO₂ Cathode Degradation by Reaction with HF and Protection by Thin Oxide Coatings. *ACS Applied Materials & Interfaces* **2015**, *7* (43), 24265-24278.
25. Markevich, E.; Sharabi, R.; Gottlieb, H.; Borgel, V.; Fridman, K.; Salitra, G.; Aurbach, D.; Semrau, G.; Schmidt, M. A.; Schall, N.; Bruenig, C., Reasons for capacity fading of LiCoPO₄ cathodes in LiPF₆ containing electrolyte solutions. *Electrochemistry Communications* **2012**, *15* (1), 22-25.
26. Wang, Q.; Ping, P.; Zhao, X.; Chu, G.; Sun, J.; Chen, C., Thermal runaway caused fire and explosion of lithium ion battery. *Journal of Power Sources* **2012**, *208*, 210-224.

27. Yao, X. L.; Xie, S.; Chen, C. H.; Wang, Q. S.; Sun, J. H.; Li, Y. L.; Lu, S. X., Comparative study of trimethyl phosphite and trimethyl phosphate as electrolyte additives in lithium ion batteries. *Journal of Power Sources* **2005**, *144* (1), 170-175.
28. Lisbona, D.; Snee, T., A review of hazards associated with primary lithium and lithium-ion batteries. *Process Safety and Environmental Protection* **2011**, *89* (6), 434-442.
29. Aurbach, D.; Talyosef, Y.; Markovsky, B.; Markevich, E.; Zinigrad, E.; Asraf, L.; Gnanaraj, J. S.; Kim, H.-J., Design of electrolyte solutions for Li and Li-ion batteries: a review. *Electrochimica Acta* **2004**, *50* (2-3), 246-253.
30. Xu, K., Nonaqueous Liquid Electrolytes for Lithium-Based Rechargeable Batteries. *Chemical Reviews* **2004**, *104* (10), 4303-4418.
31. Xu, K.; Lam, Y.; Zhang, S. S.; Jow, T. R.; Curtis, T. B., Solvation Sheath of Li⁺ in Nonaqueous Electrolytes and Its Implication of Graphite/Electrolyte Interface Chemistry. *The Journal of Physical Chemistry C* **2007**, *111* (20), 7411-7421.
32. Abe, K., Nonaqueous Electrolytes and Advances in Additives. In *Electrolytes for Lithium and Lithium-Ion Batteries*, Jow, T. R.; Xu, K.; Borodin, O.; Ue, M., Eds. Springer: New York, 2014; pp 167-210.
33. Smith, A. J.; Burns, J. C.; Zhao, X.; Xiong, D.; Dahn, J. R., A High Precision Coulometry Study of the SEI Growth in Li/Graphite Cells. *Journal of The Electrochemical Society* **2011**, *158* (5), A447-A452.
34. Smith, A. J.; Burns, J. C.; Dahn, J. R., A High Precision Study of the Coulombic Efficiency of Li-Ion Batteries. *Electrochemical and Solid-State Letters* **2010**, *13* (12), A177-A179.
35. Zhang, L.; Zhang, Z.; Haring, S.; Straughan, M.; Butorac, R.; Chen, Z.; Lyons, L.; Amine, K.; West, R., Highly conductive trimethylsilyl oligo(ethylene oxide) electrolytes for energy storage applications. *J. Mater. Chem.* **2008**, *18* (31), 3713-3717.
36. Zhang, L.; Lyons, L.; Newhouse, J.; Zhang, Z.; Straughan, M.; Chen, Z.; Amine, K.; Hamers, R. J.; West, R., Synthesis and characterization of alkylsilane ethers with oligo(ethylene oxide) substituents for safe electrolytes in lithium-ion batteries. *J. Mater. Chem.* **2010**, *20* (38), 8224-8226.
37. Chen, X.; Usrey, M.; Peña-Hueso, A.; West, R.; Hamers, R. J., Thermal and electrochemical stability of organosilicon electrolytes for lithium-ion batteries. *Journal of Power Sources* **2013**, *241*, 311-319.
38. Guillot, S. L.; Peña-Hueso, A.; Usrey, M. L.; Hamers, R. J., Thermal and Hydrolytic Decomposition Mechanisms of Organosilicon Electrolytes with Enhanced Thermal Stability for Lithium-Ion Batteries. *Journal of The Electrochemical Society* **2017**, *164* (9), A1907-A1917.

Chapter 2. Thermal and hydrolytic decomposition mechanisms of organosilicon electrolytes with enhanced thermal stability for lithium-ion batteries

2.1 Introduction

As the ubiquity of portable electronics and electric vehicles increases, the need for high-capacity energy storage devices grows correspondingly. The high energy density of lithium-ion electrochemistry have established these batteries at the forefront of meeting these growing energy storage needs.¹⁻⁴

Despite their promise as energy storage devices, several challenges remain to fully optimize the performance and safety of LIBs. The most commonly used electrolyte is composed of lithium hexafluorophosphate (LiPF_6) salt and a blend of carbonate solvents, together with additional additives to stabilize the electrode surfaces. These solvents, particularly dimethyl carbonate, have high vapor pressures and low flash points, presenting a flammability hazard.^{5, 6} Studies have also shown that cycling at elevated temperatures leads to capacity fade and performance degradation.⁷⁻¹⁰ The thermal instability of carbonate- and LiPF_6 -based electrolytes is a significant obstacle to achieving longer performance lifetimes and safer battery operation. Despite these drawbacks, LiPF_6 is the industry standard lithium salt because of its low cost, high solubility in organic solvents, and absence of corrosion when in contact with aluminum, which is typically used as the cathode current collector.¹¹

Often, the electrolyte degradation at elevated temperatures is initiated by protic impurities such as trace amounts of water. The water may come from incomplete drying of the electrolyte or from atmospheric absorption, due to the highly hygroscopic nature of LiPF_6 .^{12, 13} It is generally accepted that decomposition of LiPF_6 initiates with the formation of lithium fluoride (LiF) and phosphorus pentafluoride (PF_5) followed rapidly by reaction of PF_5 with water to form

trifluorophosphine oxide (POF_3) and hydrofluoric acid (HF).¹³ These (shown in Equation 2.1) can continue to react in the electrolyte with trace amounts of water and with solvent molecules in a catalytic cycle that leads to decomposition of the solvent and salt in amounts far exceeding the amount of water originally present. It is thus important to design an electrolyte with resistance to decomposition at elevated temperatures and in the presence of water to enable electrolyte systems with improved safety and performance.

Organosilicon solvents have shown promise as enhanced stability, non-flammable solvents for lithium-ion battery electrolytes. Relative to carbonates, organosilicon-based electrolytes have a wider electrochemical window of stability, higher flash points, reduced gas evolution, and comparable viscosities and conductivities.¹⁴⁻¹⁶ Previous studies showed that organosiloxane ($\text{R}_3\text{Si-OR}$) electrolytes exhibit good stability, with only minor decomposition of organosiloxane with 1 M LiPF_6 up to 100 °C.¹⁶ Yet, some degradation was observed arising from hydrolysis of the Si-O bond. More recent studies showed that increased resistance to hydrolysis could be achieved by introducing a short alkyl linker ($\text{R}_3\text{Si}(\text{CH}_2)_n\text{-OR}$) and using LiTFSI instead of LiPF_6 .¹⁵ The prior studies of organosilicon-based electrolytes suggest that the thermal and hydrolytic stability can be improved through changes in the molecular structure. However, to achieve rational design of improved molecules it is necessary to have an improved understanding of the fundamental pathways of electrolyte thermal decomposition. In this study, we have used NMR spectroscopy to identify the molecular-level mechanisms of decomposition of organosilicon electrolytes. With a silicon headgroup and three-carbon linker as the base structure, we investigate the impact of glycol or nitrile functional tail groups and the extent of fluorination of the silicon headgroup on thermal hydrolysis. We use the decomposition of a standard carbonate electrolyte under the same experimental conditions as a benchmark for these results. Our results demonstrate that dramatic

improvements in thermal and hydrolytic stability can be achieved through specific modifications of the organosilicon molecular structure.

2.2 Materials and Methods

2.2.1 Chemicals

Ethylene carbonate and diethyl carbonate were purchased from SoulBrain. Lithium hexafluorophosphate was purchased from BASF. All organosilicon compounds were received from Silatronix. Added water was from a NanoPure system ($\geq 18.0 \text{ M}\Omega\text{-cm}$).

2.2.2 Thermal stability and NMR analysis

Samples for NMR analysis were prepared in an argon-atmosphere glovebox. The samples were filled in FEP 5 mm tube liners (Wilma LabGlass). The liners were then heat-sealed and placed in 9" 5mm standard NMR tubes. The tubes were transferred to a vacuum manifold using air-free NMR tube-Schlenk line adapters, and the NMR tubes were carefully flame-sealed. Flame-sealing the liners at the same time as the NMR tubes resulted in various FEP decomposition products visible in the ^{19}F -NMR spectra. These peaks disappeared with the addition of the liner heat-sealing step before flame-sealing. Heated samples were stored in an oven at $100 \text{ }^\circ\text{C}$. Storage at $100 \text{ }^\circ\text{C}$ for more than a week causes some of the carbonate samples to explode, so all samples were wrapped with aluminum foil for safety. Samples were analyzed with a Bruker Avance III 500 MHz spectrometer using a CryoProbe ProdigyTM probe or BBFO PLUS probe. All spectra were referenced using a substitution reference standard of 1% TMS in CDCl_3 and processed with MestreNova 9.1.0. The calibration was applied by absolute referencing. The decomposition of LiPF_6 was quantified by setting the ^{19}F -NMR peak integration of PF_6^- to 6 and subsequently integrating the peaks of all downstream decomposition products of PF_6^- (fluorophosphates and alkyl fluorophosphates), normalizing each peak integration by the number of fluorines of the given species. Since the initial concentration of LiPF_6 is 1 molar, the concentration of PF_6^- in mol % was

calculated by dividing 1 M by (1 + sum of integrations of all PF₆ decomposition products) and multiplying by 100. The concentration of any PF₆ decomposition species can be calculated in mol % by dividing the integration of the given species (normalized by number of fluorines) by (1+ sum of integrations of all PF₆ decomposition products) and multiplying by 100. This method of calculating concentration assumes that all PF₆⁻ decomposition products are visible in the solution-phase ¹⁹F-NMR. The quantification of decomposition uses the integration of the NMR peaks, which for the fluorine spectrum reliably allows a detection limit of a peak that is at least 0.01% of the LiPF₆ peak. Given that the decomposition species LiF is known to precipitate out of solution, and decomposition species POF₃ and HF could exist in the system as gases, the calculations provide best estimates of the concentration in mol %. The quantitation may therefore slightly underestimate the extent of decomposition; this would be the case for all samples studied. The vertical axis expansion of the ¹⁹F-NMR spectra figures are all reported relative to the spectrum normalized to the LiPF₆ peak.

2.3 Results and Discussion

The goal of this study was to identify how specific molecular structural changes influenced the decomposition of organosilicon-based battery electrolytes under conditions of elevated temperature and added water. The thermal decomposition of the novel organosilicon solvents **1-4** shown in Figure 2.1 has not been investigated previously. To provide a benchmark for these samples, we utilized the same conditions to study the decomposition of the industry-standard electrolyte solvent system diethyl carbonate (DEC)/ethylene carbonate (EC) (3:7 by volume). We used ¹H-, ¹³C-, ¹⁹F-, and ³¹P-NMR spectroscopy to analyze the solution-phase decomposition of carbonate and organosilicon samples. We stored electrolyte samples at 100 °C for up to 20 days and tested the effects adding 1000 ppm (v/v) excess water, with control samples having no added

water. We also performed similar experiments at room temperature and found that the major products observed at elevated temperature were also observed in smaller amount after storage at room temperature. Because many of the products are present at low concentrations that yield signals near the detection limit of NMR, we present here primarily the results at elevated temperature where concentrations can be more accurately determined. Our results indicate that the same products are formed at both temperatures, but the use of elevated temperatures to accelerate the decompositions leads to concentrations more readily detectable by NMR. Similarly, while an intact battery would typically have water concentrations <30 ppm, the introduction of higher amounts of water accelerates the reactions and makes the products more clearly detectable.

2.3.1 Organosilicon electrolytes decomposition

Figure 2.1 shows the organosilicon solvents **1-4** in this study and highlights the different structural features under investigation. Each electrolyte was formulated as a single solvent with 1 M LiPF₆, and the formation of thermal degradation products over time was monitored by storage at 100°C and periodic NMR spectroscopy analyses for ~20 days. While previous work suggested that adding an alkyl spacer between the Si atom and the glycol group (as in compound **1**) reduced decomposition,¹⁴ the influence of the Li-chelating R tail group and of fluorination of the Si atom on stability have not been investigated. To assess the importance of these structural features on the thermal stability of these electrolytes, we compared electrolyte solvents **1** (3-[diethylene glycol monomethyl ether]propylfluorodimethylsilane) and **3** (3-cyanopropylfluorodimethylsilane) to probe the differences between glycol vs nitrile tail functional groups respectively. A comparison of cyanopropylsilanes bearing trimethyl silicon (**2**), monofluorodimethyl silicon (**3**) and difluoromonomethyl silicon (**4**) groups was used to determine the impact of silicon fluorination on thermal decomposition mechanisms.

The storage of carbonate electrolytes at elevated temperatures results in the appearance of new peaks in the spectra of ^1H , ^{13}C , ^{19}F , and ^{31}P -NMR indicative of electrolyte reactions and the formation of new products.^{12, 13, 17} We used ^{19}F and ^{31}P spectra to identify and quantify all degradation products formed from breakdown of the PF_6^- anion, since all downstream products of PF_6^- degradation must contain one of these nuclei. Each product was identified using its chemical shift, multiplet splitting pattern, and spin-spin coupling constant, and by correlating splittings and peak areas between ^{19}F and ^{31}P spectra across many different samples and experimental conditions.

2.3.1.1 Impact of organosilicon tail group on thermal stability

Both glycol and nitrile organosilicons were initially formulated with 1 M LiPF_6 . PF_6^- appears in organosilicon electrolytes as a doublet in ^{19}F at -71.9 ppm, with a phosphorus-fluorine coupling constant of 710 Hz, and a septet in ^{31}P at -144.1 ppm ($J_{\text{P-F}} = 710$ Hz). Prior to any thermal treatment and/or intentional addition of water, each sample was analyzed as-formulated. Table 2.1 summarizes the identifying features of each fluorine-containing species in the as-formulated and thermally treated sample. Note that while fluorophosphates are reported here as anions, they are likely involved in an equilibrium between the protonated and deprotonated forms.¹³ Our results show that for all common degradation species, the chemical shift of the same species changes only minimally (< 1.5 ppm difference) between the different organosilicon electrolyte solutions 1-4.

The as-formulated electrolyte solution of **1** has three small ^{19}F doublets arising from initial decomposition products. The first doublet at -83.2 ppm ($J_{\text{P-F}} = 928$ Hz) has a corresponding ^{31}P triplet with the same coupling constant. Based on the triplet phosphorus splitting (indicating a difluorinated species) and chemical shifts previously reported for this species,^{12, 13, 18} we attribute these peaks to PO_2F_2^- . The third doublet at -89.0 ppm correlates to a quartet in ^{31}P , and we therefore assign this to the trifluorophosphine oxide POF_3 . The as-formulated electrolyte solution of **3** also

had two sets of doublets; we attribute these features to PO_2F_2^- and POF_3 respectively, due to their correspondence of chemical shift and coupling with the peaks in electrolyte **1**. The presence of these fluorophosphates indicates that trace amounts of water were present in the as-formulated electrolyte and induced decomposition of minor amounts ($< 0.4\%$) of the PF_6^- before any thermal treatment or intentional addition of water. The presence of trace amounts of water in electrolytes is unavoidable and has also been reported in previous studies of carbonate electrolytes.^{13, 19} The source of this water may come from both the solvent and the salt, as LiPF_6 is known to be highly hygroscopic and the solvent requires drying after synthesis.

Figure 2.2 shows the ^{19}F -NMR spectra of electrolytes **1** and **3** after the addition of 1000 ppm (v/v) water and storage at 100°C for three weeks. Electrolyte **1** (Figure 2.2a) shows an increase of the PO_2F_2^- peak and simultaneous disappearance of the POF_3 peak, indicating the successive hydrolysis of PF_6^- degradation products. The formation of these fluorophosphates indicates progressive hydrolysis of PF_6^- via the reactions 1-3. LiPF_6 dissociates to form the reactive Lewis acid PF_5 . PF_5 reacts with water to form POF_3 , which reacts further with water to form the fluorophosphate PO_2F_2^- . This mechanism is consistent with the known hydrolysis mechanisms of PF_6^- with water in carbonate solvents.^{12, 13, 19, 20} In contrast, electrolyte **3** (Figure 2.2b) shows only minimal growth of the PF_6^- decomposition peaks, and even after three weeks of thermal treatment with excess added water, there is still POF_3 present that has not been hydrolyzed to PO_2F_2^- .



After identifying all PF_6^- degradation products, we compared the extent of PF_6^- decomposition between **1** and **3**. The decomposition of PF_6^- in the ^{19}F spectra was quantified by integrating the NMR peak areas of all the PF_6^- decomposition products. To interpret the data in terms of concentrations of different chemical species, the peak of each species was normalized to the number of F atoms in the species, via the equation:

$$\text{Concentration of species } i \text{ (mol/L)} = X_i = \frac{\frac{A_i}{n_i}}{\sum \frac{A_p}{n_p}} \quad (2.4)$$

where A_i is the NMR peak area corresponding to species i and n_i is the number of fluorine atoms of species i . Species p are PF_6^- and all its fluorophosphate decomposition products; since the initial concentration of PF_6^- is 1 molar, dividing the normalized area of any species i by this sum gives the concentration of species i in mole/L. Given the small headspace of the sealed NMR sample tube, we assume that the loss of fluorophosphate products to the gas phase is negligible relative to the concentration remaining in solution. There is no evidence of the complete hydrolysis of fluorophosphates to form phosphoric acid/phosphate ion in the ^{31}P -NMR (singlet near 0 ppm),²¹ therefore the complete quantification of PF_6^- degradation can be achieved through the ^{19}F spectra.²²

Figure 2.3 shows the concentration of PF_6^- in solvents **1** and **3** as a function of time while stored at 100°C ; data are shown for as-formulated samples (with no water added, Figure 2.3a) and samples with 1000 ppm (v/v) added water (Figure 2.3b). Multiple trials are shown to demonstrate the reproducibility of thermal decomposition for each sample. For both organosilicon electrolytes **1** and **3** in Figure 2.3a, PF_6^- shows exceptional thermal stability for the as-formulated sample (< 5% decomposition). For the sample with water added (Figure 2.3b), organosilicon glycol **1** shows

5-10% decomposition of PF_6^- during the first 330 hours of storage at 100°C . In organosilicon nitrile **3**, the decomposition of PF_6^- is significantly less, with a concentration loss of less than 4%. The PF_6^- decomposition in organosilicon glycol **1** is therefore more sensitive to water concentration than organosilicon nitrile **3**.

In addition to hydrolysis of the PF_6^- anion, we investigated the thermal and hydrolytic reaction mechanisms of the solvents themselves. Every solution-phase species resulting from solvent reactions can be observed and identified with a combination of ^1H , ^{19}F , and ^{13}C -NMR spectroscopy.

Glycol tail group decomposition mechanisms

Molecules with glycol functionalities have been investigated previously as battery electrolyte solvents due to the ability of the oxygen lone pairs to chelate lithium ions, enhancing electrolyte conductivity.^{23, 24} Furthermore, the flammability of these solvents can be tuned by the number of alkyl ether groups in the glycol chain, with an increasing chain length corresponding to a higher solvent flashpoint.²⁴ Zhang et al. showed that organosilicon glycols also have enhanced conductivity and reduced flammability compared with carbonate solvents.^{14, 15}

Figure 2.4a shows the ^{19}F -NMR spectra of solvent **1** + 1 M LiPF_6 + 1000 ppm (v/v) water, in the case immediately after water addition and after the samples were stored at 100°C for two weeks. Figure 2.4b shows the corresponding ^{13}C spectrum for the latter sample. In Figure 2.4a, the as-formulated sample has a primary peak at -160.6 ppm. Based on the silicon satellites and a nonet fluorine-hydrogen splitting pattern this peak is assigned to solvent **1**. After two weeks of high temperature storage a new septet appears at -130.7 ppm; this splitting indicates a species coupled to six hydrogens. From the splitting pattern in ^{19}F and the corresponding triplet that appears

concurrently at -3.7 ppm in the ^{13}C spectrum (Figure 2.4b), this species is assigned as difluorodimethylsilane. As the only source of silicon is **1**, formation of difluorodimethylsilane must result from the cleavage of the silicon-methylene bond in **1** and fluorination of the silicon fragment. Pentacoordinated silicon species as intermediates in substitution reactions are well-documented in the literature, particularly when a source of fluoride is present, due to the Lewis acidic nature of silicon.^{25,26} Based on this precedent, we propose that difluorodimethylsilane forms via a hypervalent silicon intermediate as depicted in Scheme 2.1. Due to the structural similarity of the byproduct (diethylene glycol propyl methyl ether) to **1**, this product would be expected to appear in the ^{13}C spectra as a series of peaks with chemical shifts close to those of the main solvent peaks. Indeed, the corresponding ^{13}C NMR spectrum in Figure 2.4a shows several small peaks (highlighted by arrows) whose chemical shifts are similar to those expected for diethylene glycol propyl methyl ether. However, since these peaks would be similar for most alkyl glycol ether species,²⁷ specific assignments cannot be determined with certainty. Furthermore, we anticipate that any ethylene glycol propyl methyl ether might continue to break down further. This is supported by the ^{13}C spectrum (Figure 2.4b) showing the presence of propene. We therefore simply conclude that several different alkyl glycol products likely form as breakdown products of **1**.

Figure 2.4b shows the corresponding ^{13}C spectrum for the sample of **1** with added water and then stored at 100°C; the ^{13}C spectrum shows a significant new peak at 67.1 ppm. Based on known chemical shifts in the literature,²⁸ we assign this peak to 1,4-dioxane. A known method of 1,4-dioxane formation is through acid-catalyzed intramolecular cyclodehydration.²⁹ Furthermore, glycol species similar to **1** have been shown to yield 1,4-dioxane in the presence of an acid catalyst.²⁹ The mechanism in that study produces methanol as a side product when a methyl ether is the starting reagent. However, we find no evidence of methanol (chemical shift expected at 50

ppm)²⁸ in the ¹³C spectra of **1**. In Scheme 2.2, we propose that the formation of 1,4-dioxane proceeds via acid-catalyzed intramolecular cyclization of the glycol tail group, which would transfer the methyl ether to the silane to give fluoro(3-methoxypropyl)dimethylsilane in addition to the dioxane. This product results from transfer of the terminal methyl group to the silane oxygen closest to the silicon.

While the intensity of the 1,4-dioxane peak in Figure 2.4b appears to indicate that the concentrations of 1,4-dioxane and **1** are nearly equal (indicating 50% decomposition of the electrolyte solvent), the single 1,4-dioxane peak represents four equivalent carbons. While these ¹³C spectra are not quantitative, the relative concentration of 1,4-dioxane can be estimated by dividing the peak intensity by four. Even considering this qualitative normalization, it is clear that the concentration of 1,4-dioxane exceeds that of any other decomposition product in the ¹³C spectrum. We hypothesize that either the formation of 1,4-dioxane from **1** proceeds via several different mechanisms or that the other products formed with 1,4-dioxane are unstable and break down further. For example, in Figure 2.4b, three small septets appear immediately downfield of the peak for **1** in the ¹³C spectrum. These peaks are consistent with any monofluorodimethyl alkyl silane product similar to **1**, such as the silane byproduct formed in Scheme 2.2.

Figure 2.4c shows similar data to 4b, except that the experiment was performed at room temperature for 21 days with 500 ppm added water. In this case the same products are observed as in Fig. 2.4b but the concentrations are lower, leading to signal levels that are close to the signal-to-noise limit of the NMR instrument.

The above experiments identified two main decomposition mechanisms for the thermal degradation of **1**. The primary degradation pathway is acid-catalyzed cleavage of the glycol tail group to produce 1,4-dioxane, likely by the pathway depicted in Scheme 2.2. A second, minor

pathway arises from cleavage of the silicon-fluorine bond, producing difluorodimethylsilane by the pathway depicted in Scheme 2.1. These results suggest that the thermal stability of organosilicons can be improved by altering the nature of the tail group.

Nitrile tail group decomposition mechanisms

Organic nitrile molecules have previously been investigated for use in battery electrolytes because of their high oxidative stability due to the strong electron-withdrawing nature of the nitrile substituent.³⁰⁻³² The electronegative nitrile group also promotes solvation of the lithium ion.^{31, 33} These promising properties led us to investigate the thermal stability of organosilicon electrolytes with nitrile tail groups, beginning with a comparison of **3** with the analogous glycol molecule **1**.

Figure 2.5a shows the ¹⁹F-NMR spectrum of the as-formulated sample of **3** + 1 M LiPF₆ and the same sample after storage at 100 °C for 18 days; Figure 2.5b shows the corresponding ¹H-NMR spectra. A comparison of the as-formulated and heat-treated ¹⁹F spectra in Figure 2.5a shows that storage at elevated temperatures does not lead to any new peaks. Even when magnified, the spectrum does not show evidence for any new products. The absence of detectable difluorodimethylsilane formation shows that the organosilicon nitrile **3** resists the silicon-methylene bond cleavage suffered by glycol groups (Scheme 2.2). When the Li-chelating group is changed from glycol in **1** to nitrile in **3**, the silicon-methylene bond therefore becomes less susceptible to cleavage at high temperatures.

While the ¹⁹F spectra show that **3** appears to be completely resistant to degradation, the corresponding ¹H spectra in Figure 2.5b shows storage at high temperatures leads to the appearance of at least one new species, which appears as a triplet at 2.72 ppm and peaks that appear to correspond to a doublet with individual peaks at 8.3 and 8.6 ppm. This peak separation (~150 Hz) is greater than ¹H-¹H coupling constants, which fall within the range of < 1-45 Hz.^{34, 35} Although

^{19}F - ^1H or ^{31}P - ^1H coupling constants could fall in this range (typically 115-140 Hz for $J_{\text{P-H}}$ ³⁶ and up to 130 Hz for vicinal $J_{\text{F-H}}$ ³⁷), the absence of a corresponding peak in the ^{19}F or ^{31}P spectra with the same coupling constant excludes this possibility. Consequently, we conclude that the ‘doublet’ is likely a set of two singlets. Primary amide hydrogens often appear as a set of two singlets due to the partial double bond nature of the carbon-nitrogen bond, making the primary hydrogens chemically inequivalent.³⁸ We therefore assign the two singlets to the hydrogens of a primary amide, and the triplet at 3.2 ppm to a methylene group primary to carbonyl of an amide (Figure 2.5b inset). The absence of other visible ^1H peaks associated with this amide suggests that they are too similar to the corresponding nitrile structure of **3**, evidence that the amide forms as a direct hydrolysis of the nitrile group of **3** as shown in Scheme 2.3. The concentration of the organosilicon amide is too low to be visible in the ^{13}C spectra. As Figure 2.5a shows, no additional fluorine species are seen in ^{19}F spectrum; we hypothesize that the fluorine peaks of **3** and its amide analog are too close to resolve due to their structural similarities. Despite the small amount of amide that is formed, Scheme 2.3 is important in understanding electrolyte decomposition processes in electrolyte **3**. This reaction provides an alternative mechanism for the consumption of water, which may explain the decreased decomposition of PF_6^- seen in Figure 2.3 for the nitrile organosilicon electrolyte. Similar experiments show that 1,4-dioxane and difluorodimethylsilane are also observed at room temperature but at lower concentrations; this indicates that the pathways outline in Scheme 2.3 and Scheme 2.4 are valid at both temperatures, and the primary effect of elevated temperature is to accelerates the rates and thereby makes the products more readily detectable.

In summary, by changing the glycol tail group to the nitrile, the cleavage of the silicon-carbon bond is eliminated. The nitrile tail group reacts with water to form the corresponding amide, resulting in less PF_6^- hydrolysis than in the glycol electrolyte. These results show that the nature

of the tail group of these organosilicon solvents significantly impacts the extent and mechanisms of electrolyte decomposition, and suggest that further variation of the solvent structure can effect additional tuning of the thermal properties.

2.3.1.2 Impact of organosilicon fluorination on thermal stability

Fluorination of organic molecules such as carbonates, esters, and ethers have been shown to stabilize the highest-occupied molecular orbital (HOMO) levels of these compounds, resulting in greater stability against oxidation.^{39, 40}

The effect of fluorination of the silicon atom on solvent stability was investigated by comparing the stability of the non-fluorinated solvent **2** with the mono-fluorinated compound **3** and the difluorinated solvent **4**. The fluorinated electrolytes **3** and **4** both show the same fluorophosphate decomposition products observed for the non-fluorinated molecule (**3**, Figure 2.2b). Figure 2.6 shows the mole % PF₆ remaining in all three nitrile-based electrolytes (3-5). All three nitrile-based electrolytes show < 5% PF₆ decomposition even after more than 400 hours stored at 100 °C. Furthermore, the comparison of Figure 2.6a and 2.6b show that electrolyte systems with solvents **2-4** did not show any significant change upon intentional addition of 1000 ppm (v/v) water. Thus, we conclude that the protection of PF₆⁻ against degradation via thermal hydrolysis (Equations 2.1-2.3) occurs for organosilicon nitrile solvents regardless of the extent of silicon fluorination.

Figure 2.7 shows the ¹⁹F-NMR spectra of difluorinated electrolyte **4** before and after storage at 100°C for 19 days. These spectra are focused on the organosilane region of the chemical shift range. The main peak is a sextet at -135.5 ppm (Figure 2.7a inset) with silicon satellites and split by the methyl and methylene groups adjacent to the silicon. This peak has the expected splitting and chemical shift for the solvent **4** fluorine peak. Identical to **3** in Figure 2.5, no new peaks are observed when **4** is stored at high temperature, indicating the absence of detectable silicon-methylene bond

cleavage. Figure 2.8 shows the same chemical shift region for electrolyte **2**. Since **2** is non-fluorinated, there should be no peaks in this region. However, even in the as-formulated sample in Figure 2.8a, there is a significant nonet peak at -161.3 ppm and a small peak at -156.7 ppm. The peak at -161.3 has silicon satellites and the identical line shape and chemical shift as **3** and was therefore assigned as such, indicating that the mono-fluorinated analog of **2** (which is species **3**) is an impurity found as low levels in the pristine solution of **2**. The small peak at -156.7 ppm in Figure 2.8a could not initially be identified, but after the growth of this species at high temperatures (Figure 2.8b) it is clearly split into a multiplet by nine coupled hydrogens and has silicon satellites. From the chemical shift and multiplicity we assign this species as fluorotrimethylsilane, an assignment that is confirmed by NMR reports in the literature.⁴¹ In addition to an increase in the presence of fluorotrimethylsilane, storage at 100 °C results in an increase in fluorination of **2** (as evidenced by growth of the peak assigned to **3**) and appearance of a small amount of dimethyldifluorosilane at -130.5 ppm.

The presence of fluorotrimethylsilane indicates cleavage of the silicon-methylene bond in **2**, while formation of **3** from the fluorination of **2** must result from breaking a silicon-methyl bond. Difluorodimethylsilane is a ‘secondary’ decomposition product and could occur either through fluorination of fluorotrimethylsilane or fluorination of solvent **3** resulting in silicon-methylene bond cleavage. However, the absence of difluorodimethylsilane in the samples of **3** suggests that it forms solely from fluorotrimethylsilane. Scheme 2.4 shows the proposed reactions to form the three thermal decomposition species of **3**, proceeding via penta-coordinated siliconate intermediates as proposed in Scheme 2.1. The driving force for the formation of fluorinated organosilicons might be the greatly increased stability of the silicon-fluorine bond (~135 kcal/mol) relative to silicon-carbon (~70 kcal/mol).⁴²

From the investigation of varying fluorination of the organosilicon solvents, we observe the greater thermal stability of fluorinated electrolytes **3** and **4** over the non-fluorinated organosilicon electrolyte **2**. There is no apparent thermal stability difference in the mono-fluorinated and di-fluorinated species under our experimental conditions.

2.3.1.3 Stabilization of PF₅ in organosilicon electrolytes

In addition to the peaks assigned to the decomposition species described above, in every organosilicon solvent stored at 100 °C, a series of doublet of doublets appears in the chemical shift range -58 ppm to -65 ppm. Figure 2.9 shows the ¹⁹F-NMR spectrum of **3** + 1 M LiPF₆ that has been stored at 100 °C for 22 days. Two sets of doublet of doublets appear with large coupling constants of 750-780 Hz and small coupling constants of 55-59 Hz. The values of the large coupling constants are in a range characteristic of octahedral fluorine-phosphorus species (the coupling constant of PF₆⁻ is 710 Hz).⁴³ Previous studies on PF₅ complexed to a sixth electron donor ligand has shown the same splitting with similar coupling constants and chemical shifts.¹⁸ The doublet of doublet lineshape comes from the equatorial fluorines, with a large phosphorus-equatorial fluorines splitting and a smaller splitting between the inequivalent axial and equatorial fluorines. The axial fluorines would have high multiplicity (doublet of quintets) and are often too far into the baseline to be observed; only one set of doublet of quintets can be seen in the spectrum in Figure 2.9. Based on the similar species reported in literature, we assign these peaks as two different PF₅ complexes. PF₅ complexes were observed in all organosilicon electrolytes **1-4** when stored at 100 °C for over 10 days, regardless of added water. Organosilicon nitriles **2-4** have two species as seen in Figure 2.9, while organosilicon glycol **1** forms at least four distinct complexes. The chemical shifts and coupling constants of these species, labeled ‘PF₅ Complex X’, are described in Table 2.1. In the nitriles **2-4**, we observe formation of a broadened doublet (-85.2

ppm) near the PO_2F_2^- doublet (-83.6 ppm) at precisely the same rate and quantity as the PF_5 Complex 1 peaks at -59.3 ppm. Based on this species, we assigned PF_5 Complex 1 to $\text{PF}_5\text{-PO}_2\text{F}_2^-$. The $\text{PF}_5\text{-PO(OR)F}_2$ complex has been proposed as a reactive intermediate in carbonate electrolytes but never observed.¹² $\text{PF}_5\text{-PO}_2\text{F}_2^-$ has also been observed in the synthesis of POF_4^- in CHF_3 solution, but only at temperatures of -140 °C.¹⁸ In the case of organosilicon-based electrolytes, we hypothesize that the solvent stabilizes the PF_5 complexes, which were visible in solution throughout the length of this study. Computational studies by Tasaki et al. indicated that the nature of the electrolyte solvent can greatly impact PF_5 complex formation and stabilization, supporting our hypothesis.⁴⁴ The identity of the electron donor for the second PF_5 complex in Figure 2.11 ('B') is still unknown. A number of electron-donating species that occur naturally in the electrolyte could form complexes with PF_5 including H_2O , ethers, fluorophosphates, and nitrogen-containing species.^{17, 18, 45, 46}

The strong Lewis acid PF_5 has been hypothesized as the main initiator of electrolyte degradation (polymerization, decomposition, and fluorination)(Equation 2.1).^{20, 47-49} Based on this theory, studies have investigated the addition of Lewis bases such as tris(2,2,2-trifluoroethyl)phosphite, pyridine, hexamethylphosphoramide (HMPA), hexamethoxycyclotriphosphazene (HMOPA), or dimethyl acetamide with the intention of inhibiting electrolyte degradation. The sequestration of PF_5 with these bases proved to be successful at significantly enhancing electrolyte thermal stability.^{16, 17, 47, 50} Following the same mechanism postulated by Li et al for the reversible sequestration of PF_5 by pyridine, HMPA, and HMOPA, Scheme 2.5 shows our proposed mechanism of the reversible formation of a generic PF_5 complex in organosilicon electrolytes. The spontaneous sequestration of PF_5 in organosilicons

appear to inhibit the reactivity of PF₅ and protect PF₆⁻ from further degradation, resulting in the high thermal stability of PF₆⁻ in organosilicon electrolytes as shown by Figures 2.3 and 2.6.

2.3.2 Carbonate electrolytes decomposition

As these organosilicon electrolytes are novel, we needed to benchmark our thermal stability studies against a well-known electrolyte system. Towards this end we investigated the thermal stability of the binary carbonate electrolyte EC/DEC (3:7, v:v) 1 M LiPF₆ during storage of NMR samples at 100 °C. The high degree of decomposition in carbonate electrolytes was clear because many carbonate sample NMR tubes broke when stored at 100°C, due to increased internal pressure in the sealed tubes from the gaseous decomposition products being generated. Figure 2.10 shows the ¹⁹F and ³¹P NMR spectra of some of the unbroken carbonate electrolyte samples after storage at 100°C for 17 days. The identifying details of the carbonate decomposition species observed in the ¹⁹F and ³¹P-NMR are described in Table 2.2, including chemical shifts, coupling constants, and splitting patterns.

After the high-temperature storage, in addition to an increase in PO₂F₂⁻, a similar ¹⁹F doublet forms at -85.9 ppm (*J*_{P-F} = 1006 Hz). The corresponding ³¹P peaks (identified by the corresponding coupling constant) are a triplet of triplets with splitting from two fluorines but also coupling with hydrogens (*J*_{P-H} = 9.7 Hz), consistent with the alkyl fluorophosphate PO(OCH₂CH₃)F₂. The remaining three doublets in the ¹⁹F spectra are also doublets in ³¹P, indicating monofluorinated species. The ³¹P doublet with no hydrogen coupling is assigned to PO₃F²⁻, while we assign the doublet of triplets to PO₂(OCH₂CH₃)F⁻ and the doublet of quintets to PO(OCH₂CH₃)₂F. The corresponding peaks of these fluorophosphates in ¹⁹F are identified by corresponding phosphorus-fluorine coupling constants. While it is difficult to assign the peaks to all the different possible fluorophosphates with complete confidence, the correlation of ¹⁹F and ³¹P

coupling constants and the splitting patterns provide strong evidence for the assignments stated above. Furthermore, the chemical shifts and coupling constants of PF_6^- , PO_2F_2^- , $\text{PO}_3\text{F}_2^{2-}$, $\text{PO}(\text{OCH}_2\text{CH}_3)_2\text{F}$, $\text{PO}(\text{OCH}_2\text{CH}_3)\text{F}_2$ have been reported previously and our observations agree with these known and accepted values, accounting for small chemical shift and coupling constant variation due to differences in carbonate composition.^{12, 13, 20, 51}

The successive formation of fluorophosphates PO_2F_2^- and $\text{PO}_3\text{F}_2^{2-}$ is consistent with the known and accepted hydrolysis mechanism of PF_6^- with water (Equations 2.1-2.3), as seen in the organosilicon electrolyte **1-4**. The alkyl fluorophosphates that appear ($\text{PO}(\text{OCH}_2\text{CH}_3)_2\text{F}$, $\text{PO}(\text{OCH}_2\text{CH}_3)\text{F}_2$, $\text{PO}_2(\text{OCH}_2\text{CH}_3)\text{F}^-$) are evidence of the reaction of fluorophosphates with the carbonate solvents, as previously reported.^{12, 20, 51} The mechanism proposed by Campion et al for the reaction of a linear carbonate with POF_3 produces RF and CO_2 , where R is the alkyl group on the carbonate.¹² Both CO_2 and $\text{CH}_3\text{CH}_2\text{F}$ were seen in the decomposition of the binary EC/DEC electrolyte. $\text{CH}_3\text{CH}_2\text{F}$ is also seen in the ^{19}F spectrum in Figure 2.10a at -212 ppm. These species suggest the decomposition of carbonates in our system follows the mechanisms shown in Scheme 2.6. Another alkyl fluoride appears at -226 ppm in the ^{19}F spectrum, with the triplet of quartet splitting pattern consistent with an ethylene fluoride substituent ($\text{RCH}_2\text{CH}_2\text{F}$). Wilken et al observed ($\text{PO}(\text{F}_2)(\text{OCH}_2\text{CH}_2\text{F})$) as a decomposition product resulting from the reaction of ethylene carbonate with POF_3 . While the $\text{RCH}_2\text{CH}_2\text{F}$ peak in Figure 2.10 would be consistent with this species, the lack of a corresponding doublet for the phosphorus fluorides (POF_2) suggests that if this pathway occurs it is not a major method of decomposition under our experimental conditions. The identity of $\text{RCH}_2\text{CH}_2\text{F}$ and its exact formation mechanism from carbonate breakdown remains unknown. The fluorophosphates and alkyl fluoride decomposition species identified confirm that these carbonate samples decompose via the mechanisms proposed in previous studies.^{19, 51}

The role of water in the decomposition of carbonate electrolytes was investigated by preparing samples with 1000 ppm of added water and control samples with no water added. Both samples were stored at 100°C. There were no differences in the types of decomposition species produced when excess water was added. However, extent of decomposition was increased slightly with the addition of water. In the sample with no added water, 30% of the initial concentration of LiPF₆ decomposed after 450 hours of elevated temperature storage. When water was added, the decomposition increased to 40% (Figure 2.11). These results indicate that water contributes to carbonate electrolyte decomposition, as further indicated by the observed fluorophosphate decomposition species and reaction mechanism described above. The carbonate sample with no water added most likely contains trace water impurities from incomplete drying of the electrolyte. Figure 2.11 also shows a comparison of the decomposition of LiPF₆ in carbonates and organosilicons. In both electrolytes 1 and 3, the decomposition of LiPF₆ is at most 15% and seems to reach a plateau over time. By contrast, in carbonate electrolytes, LiPF₆ rapidly decomposes by 30-40%, and appears to continue to degrade, although we were unable to test the degradation for longer experiment times due to the carbonate samples breaking. These data show the significant increase in thermal stability of the lithium salt provided by organosilicon solvents over carbonates.

2.4 Conclusions

The standard carbonate electrolytes used in lithium-ion batteries have poor thermal stability. In this study, organosilicon solvents were shown to be stable against reaction with LiPF₆, even when stored at high temperatures. Unlike carbonate solvents, the organosilicon decomposition mechanisms indicate that the salt and solvent degradations are decoupled, which leads in part to the enhanced stability of LiPF₆ in organosilicon solvents. Furthermore, the formation of PF₅ complexes in organosilicon solvents prevents further LiPF₆ degradation. The

addition of water to organosilicon electrolytes produces only a slight increase in the onset and extent of decomposition of LiPF_6 but does not introduce new types of decomposition products. Investigation of the specific impact of different organosilicon structures showed that a glycol tail group is a point of intramolecular attack, while a nitrile substituent is stable against breakdown even when stored at high temperatures. Fluorination of the silicon also leads to decreased solvent reactions and improved thermal stability.

Due to species produced at trace concentrations in carbonate and organosilicon electrolytes at high temperatures, and the production of gas-phase degradation species which were not analyzed in this study, a complete mechanistic and kinetic picture of thermal degradation in organosilicon electrolytes could not be achieved. Nevertheless, we have uncovered many important mechanisms in the decomposition processes for these novel electrolyte solvents. These studies can aid in the future design of organosilicon electrolytes with exceptional thermal stability and improved performance in battery cells. Organosilicon molecules represent a promising new class of thermally stable battery electrolyte solvents whose thermal stability can be tuned by the nature of the molecular substituents.

2.5 Figures

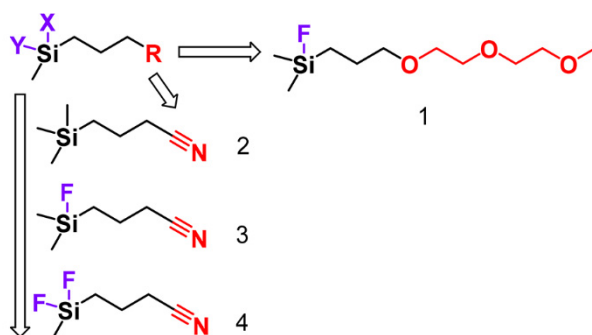


Figure 2.1 Structures of the four organosilicon solvents tested in this study. The R tail group substituent was either diethylene glycol monomethyl ether (**1**) or nitrile (**2-4**). The X and Y silicon substituents were methyl or fluorine moieties; the extent of fluorination was increased in the order **2** (non-fluorinated), **3** and **1** (monofluorinated), and **4** (difluorinated).

Table 2.1 NMR identifying features for all fluorine-containing organosilicon degradation products: chemical shifts, coupling constants, and splitting patterns.

Species	^{19}F ppm, mult (Hz)	^{31}P ppm, mult (Hz)
1	-160.6, m ($J_{\text{H-F}} = 7.3$)	-
3	-161.3, m ($J_{\text{H-F}} = 6.3$)	-
4	-135.5, m ($J_{\text{H-F}} = 6.0$)	-
PF_6^-	-72, d ($J_{\text{P-F}} = 710$)	-144, sept ($J_{\text{P-F}} = 710$)
POF_3	-89, d ($J_{\text{P-F}} = 1066$)	-35, quart ($J_{\text{P-F}} = 1066$)
PO_2F_2^-	-84, d ($J_{\text{P-F}} = 930-960$)	-20, t ($J_{\text{P-F}} = 930-960$)
PO_3F^{2-}	-76, d ($J_{\text{P-F}} = 916$)	-8.29, d ($J_{\text{P-F}} = 916$)
$\text{Si}(\text{Me}_3)\text{F}$	-156.7, m ($J_{\text{H-F}} = 7.5$)	-
$\text{Si}(\text{Me}_2)\text{F}_2$	-130.7, sept ($J_{\text{H-F}} = 6.3$)	-
PF ₅ complex 1: PO ₂ F ₂ → PF ₅ (equatorial)	-59.3, dd ($J_{\text{P-Feq}} = 755, J_{\text{Fax-Feq}} = 55$)	-
PF ₅ complex 1: PO ₂ F ₂ → PF ₅	-85.5, d ($J_{\text{P-F}} = 970$)	-
PF ₅ complex 2: B2 → PF ₅ (equatorial) ¹	-63, dd ($J_{\text{P-Feq}} = 778, J_{\text{Fax-Feq}} = 58$)	-
PF ₅ complex 3: B3 → PF ₅ (equatorial) ¹	-60.0, dd ($J_{\text{P-Feq}} = 747, J_{\text{Fax-Feq}} = 56$)	-
PF ₅ complex 4: B4 → PF ₅ (equatorial) ¹	-60.4, dd ($J_{\text{P-Feq}} = 742, J_{\text{Fax-Feq}} = 57$)	-
PF ₅ complex 5: B5 → PF ₅ (equatorial) ¹	-60.2, dd ($J_{\text{P-Feq}} = 749, J_{\text{Fax-Feq}} = 27$)	-
HF	-182 - -189, s	-

1) B represents any unknown Lewis base

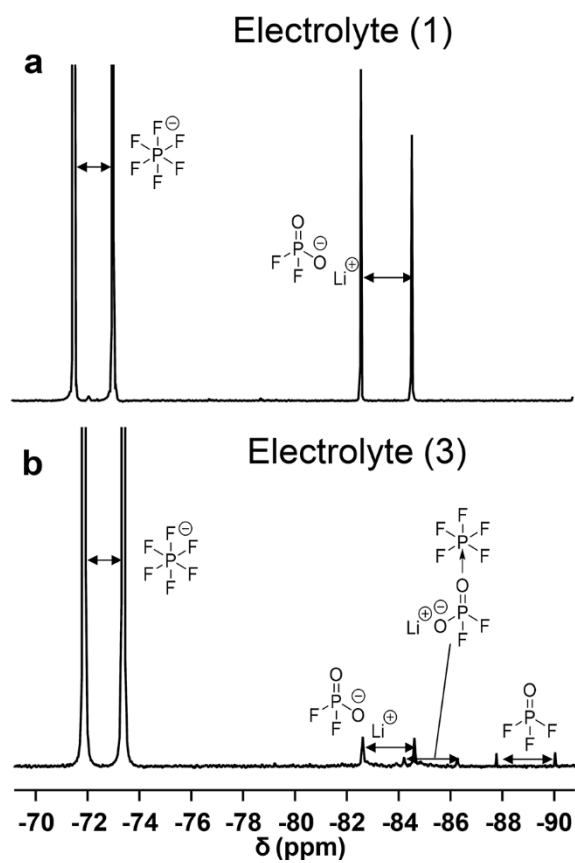


Figure 2.2 ^{19}F -NMR of decomposition species formed in a) organosilicon glycol electrolyte **1**, stored at 100°C for 19 days after adding 1000 ppm of water and b) organosilicon nitrile electrolyte **3**, stored at 100°C for 22 days after adding 1000 ppm of water.

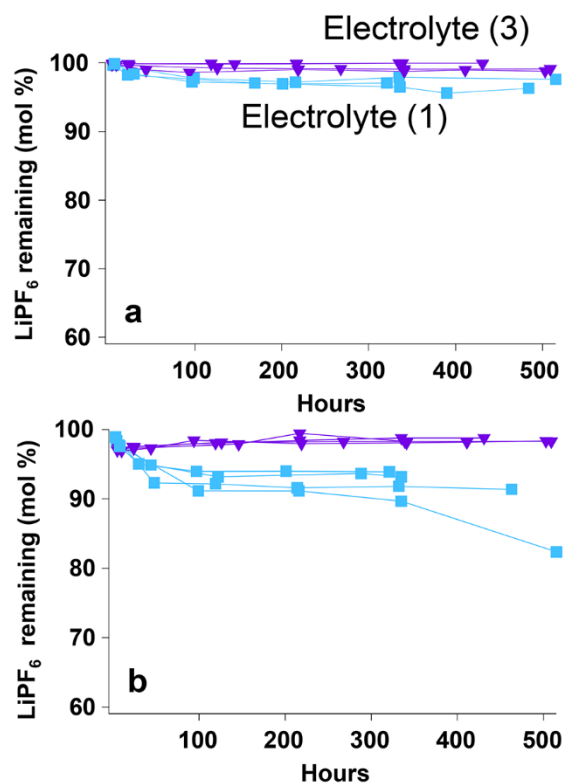


Figure 2.3 Decomposition of LiPF₆ in organosilicon electrolytes stored at 100°C with (a) no added water and (b) 1000 ppm added water. Organosilicon glycol electrolytes (**1** + 1 M LiPF₆) are light blue square markers (■) and organosilicon nitrile electrolytes (**3** + 1 M LiPF₆) are indigo triangle markers (▼). Quantification of LiPF₆ decomposition was calculated as described in the Materials and Methods.

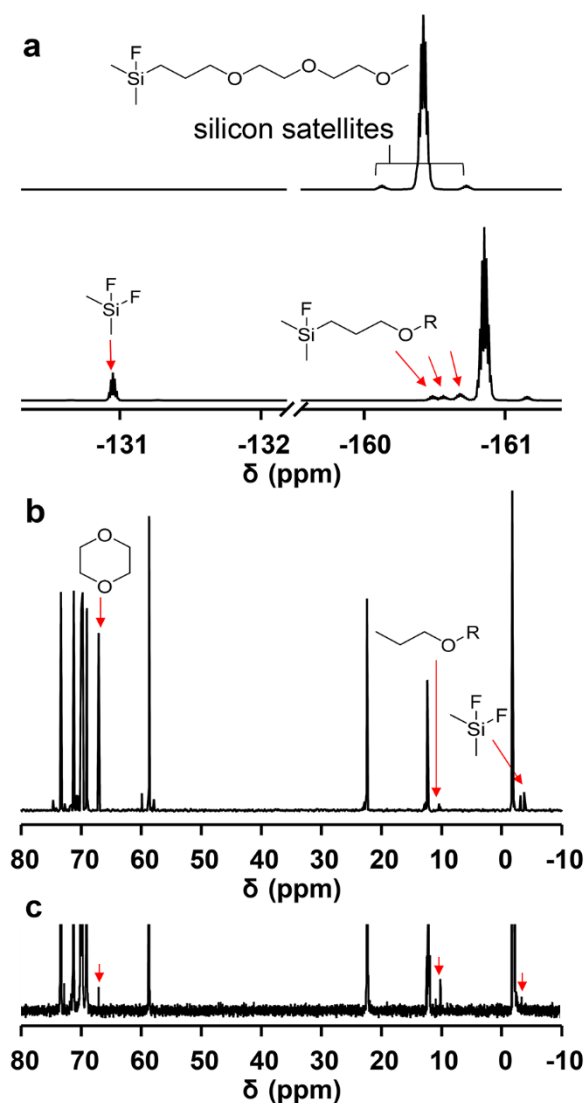
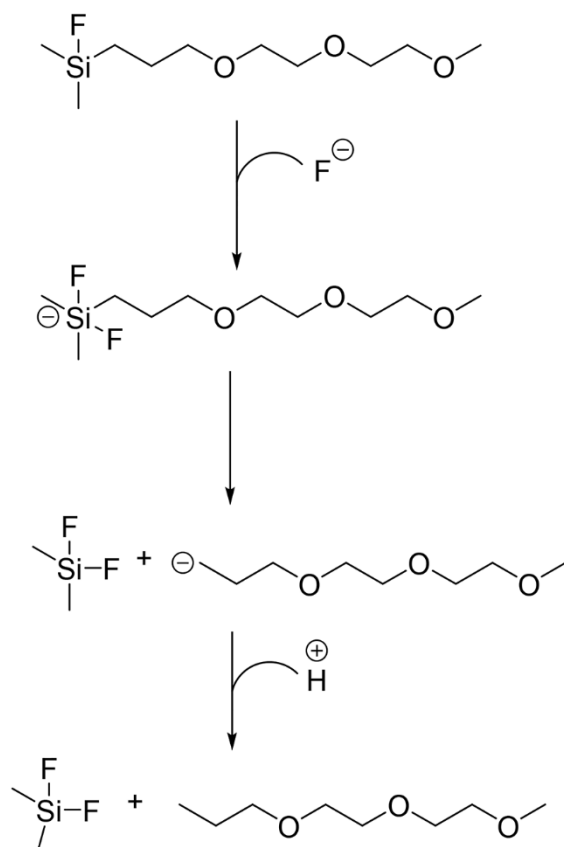
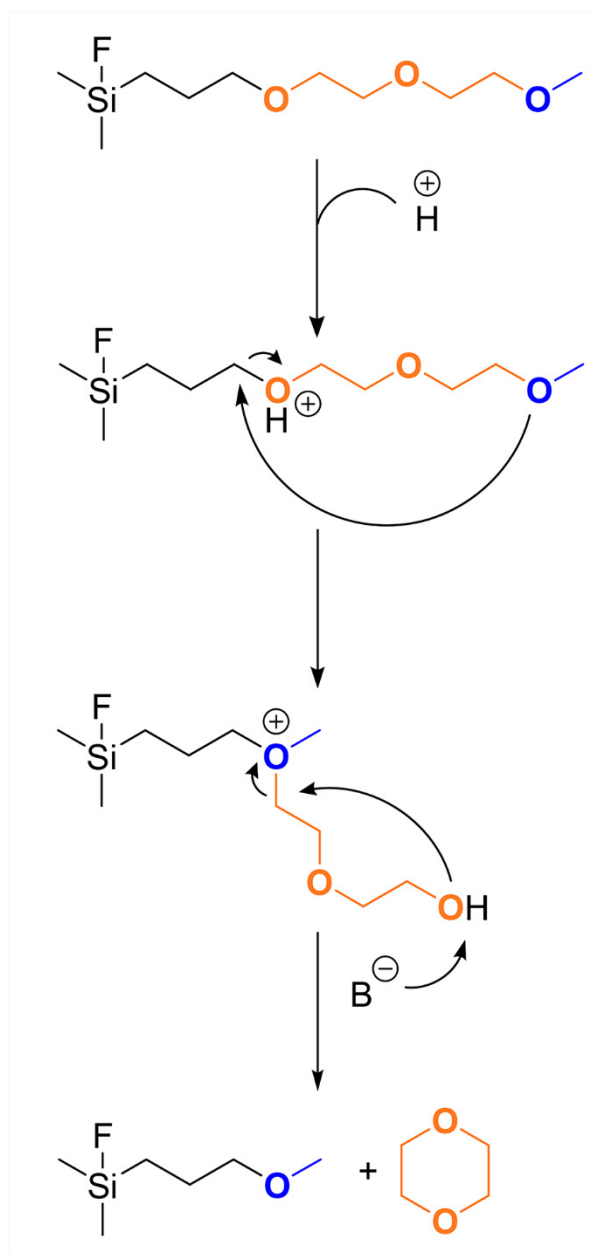


Figure 2.4 NMR spectra of **1** + 1 M LiPF₆: (a) ¹⁹F spectrum immediately after addition of 1000 ppm water (v/v) (top) and the same sample after storage at 100°C for 15 days (bottom). (b) ¹³C spectrum of the same sample after 19 days 100°C storage. Thermal decomposition products are highlighted with red arrows. (c) ¹³C spectrum of sample after 20 days at room temperature showing that the same products form, but at lower concentrations leading to NMR signals close to the signal-to-noise limit of the measurement.



Scheme 2.1 Proposed mechanism of thermal decomposition of **1** to form difluorodimethylsilane.



Scheme 2.2 Proposed mechanism of thermal decomposition of **1** to form 1,4-dioxane. B represents conjugate base of H^+ .

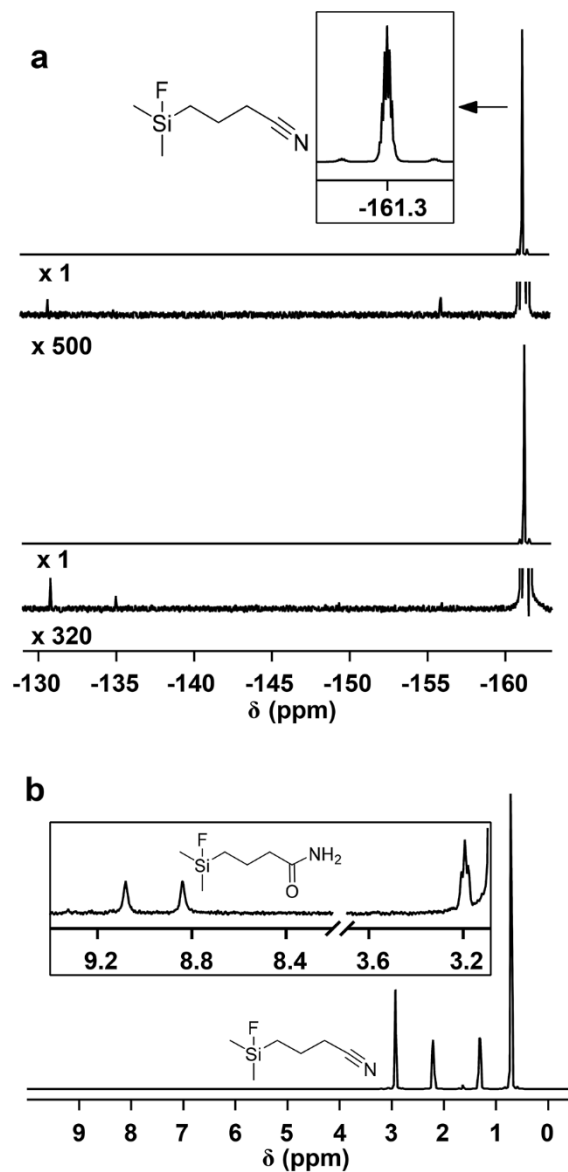
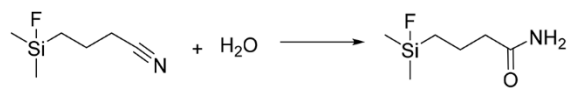


Figure 2.5 NMR spectra of **3** + 1M LiPF₆: (a) In the ¹⁹F spectrum, no thermal decomposition products are seen when comparing the solution immediately after adding 1000 ppm water (top) the same solution after storage at 100 °C for 22 days (bottom). (b) In the ¹H spectrum, Inset shows vertical and horizontal expansion of peaks in 2.5-3.5 ppm and 7.5-9.0 ppm regions, evidence of hydrolysis of **3** to organosilicon amide after storage at 100 °C for 10 days.



Scheme 2.3 Hydrolysis of **3** to form an organosilicon amide.

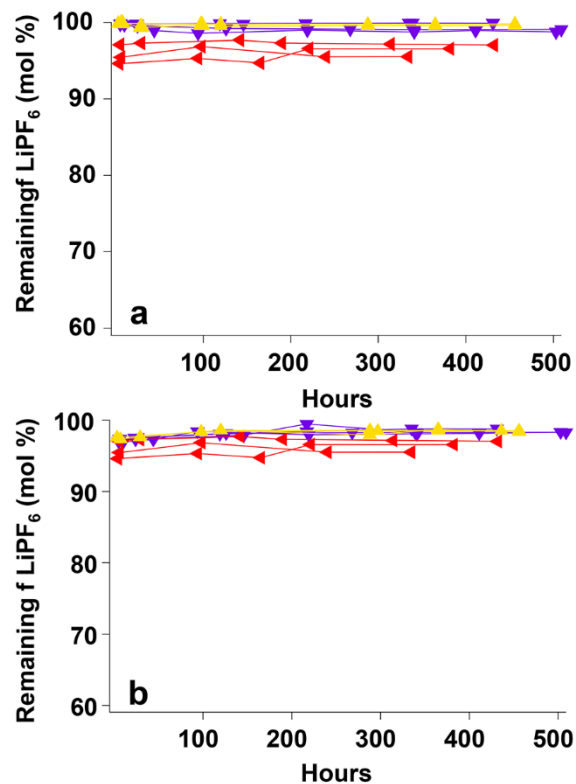


Figure 2.6 Decomposition of LiPF_6 in organosilicon electrolytes stored at 100°C with (a) no added water and (b) 1000 ppm added water. Non-fluorinated organosilicon nitrile electrolytes (**2** + 1M LiPF_6) are red triangle markers (\blacktriangleleft), monofluorinated organosilicon nitrile electrolytes (**3** + 1M LiPF_6) are indigo triangle markers (\blacktriangledown), and difluorinated organosilicon nitrile electrolytes (**4** + 1M LiPF_6) are yellow triangle markers (\blacktriangle). Quantification of LiPF_6 decomposition was calculated by $100 \times$ Equation 2.4.

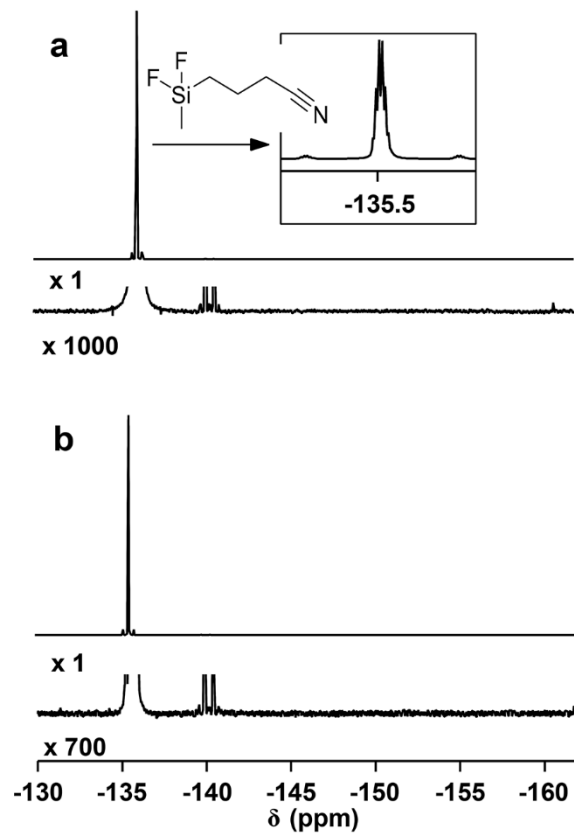


Figure 2.7 ^{19}F -NMR spectra (magnified by 5000x) of (a) an as-formulated solution of **4** + 1M LiPF_6 and (b) the same solution after storage at 100 °C for 20 days. Inset in (a) shows expansion of the main peak, representative of both spectra.

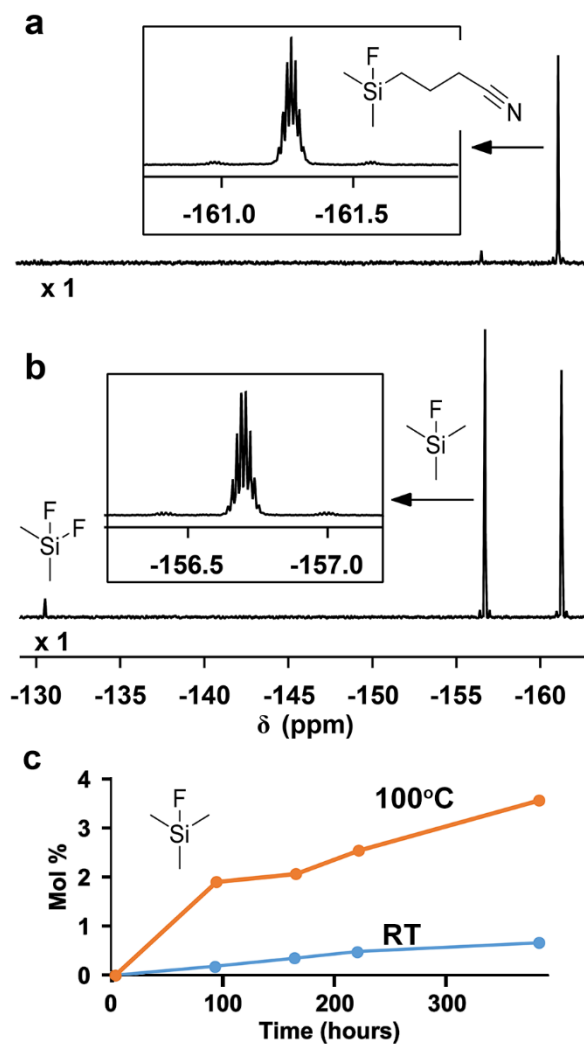
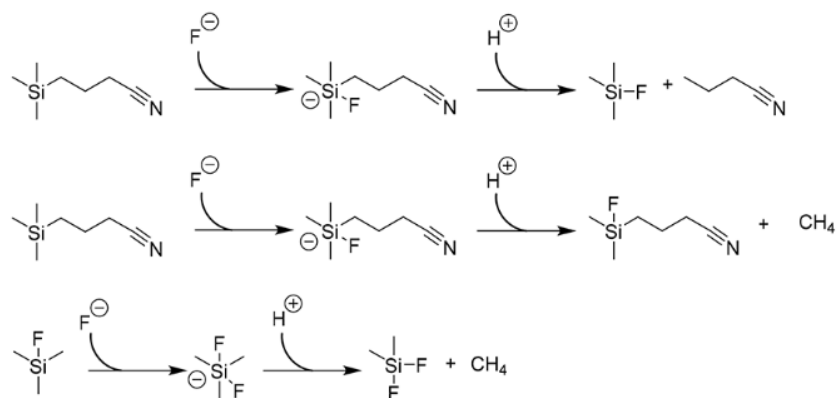


Figure 2.8 ^{19}F -NMR spectra of (a) an as-formulated solution of **2** + 1M LiPF_6 and (b) the same solution after storage at 100°C for 10 days. The inset in (a) shows the expansion of the nonet peak at -161 ppm, representative of both spectra. (c) shows monofluorosilane concentration measured at 100°C and at room temperature vs time



Scheme 2.4 Proposed mechanism of thermal fluorination of **2** via pentacoordinated silicate intermediates.

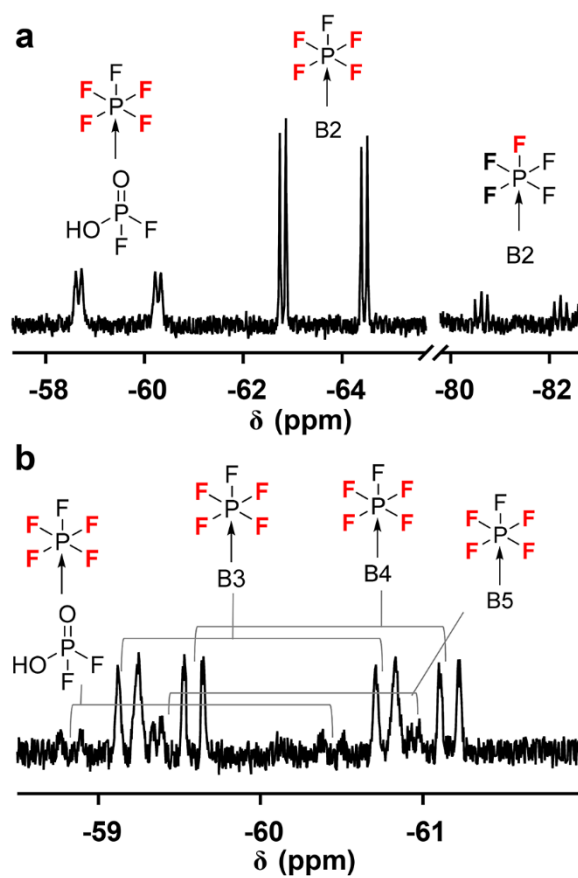
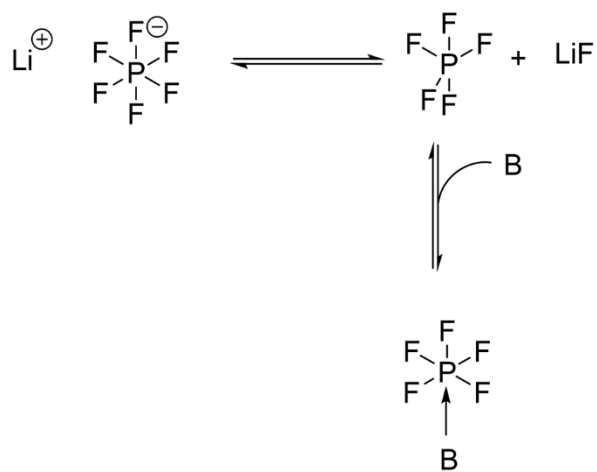


Figure 2.9 ^{19}F -NMR spectrum of PF_5 complexes formed in (a) **3** + 1 M LiPF_6 stored at 100°C for 22 days and (b) **1** + 1 M LiPF_6 stored at 100°C for 15 days. The B groups represent different unidentified Lewis base species.

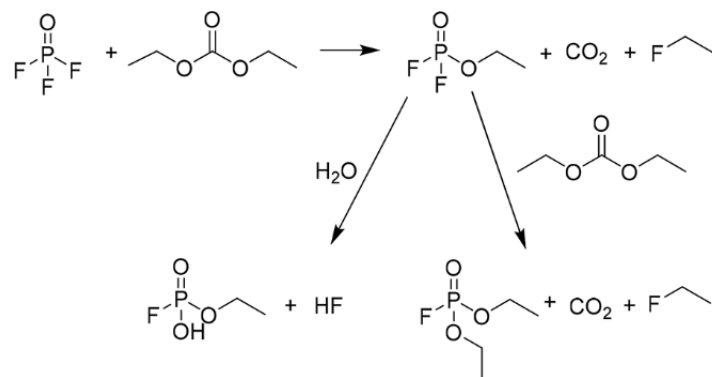


Scheme 2.5 Reversible sequestration of PF_5 by a Lewis base (B).

Table 2.2 NMR identifying features for all fluorine-containing EC/DEC degradation products:
chemical shifts, coupling constants, and splitting patterns.

Species in EC/DEC	^{19}F ppm, mult (Hz)	^{31}P ppm, mult (Hz)
PF_6^-	-74.1, d ($J_{\text{P-F}} = 708$)	-144.3, sept ($J_{\text{P-F}} = 708$)
POF_3	-89.5, d ($J_{\text{P-F}} = 1067$)	-
PO_2F_2^-	-84.8, d ($J_{\text{P-F}} = 946$)	-19.3, t ($J_{\text{P-F}} = 947$)
PO_3F^{2-}	-77.0, d ($J_{\text{P-F}} = 924$)	-9.0, d ($J_{\text{P-F}} = 924$)
$\text{PO}(\text{OCH}_2\text{CH}_3)_2\text{F}_2$	-85.9, d ($J_{\text{P-F}} = 1006$)	-20.6, tt ($J_{\text{P-F}} = 1006$)
$\text{PO}(\text{OCH}_2\text{CH}_3)_2\text{F}$	-83.1, d ($J_{\text{P-F}} = 962$)	-10.1, dp ($J_{\text{P-F}} = 961$)
$\text{PO}_2(\text{OCH}_2\text{CH}_3)\text{F}^-$	-80.7, d ($J_{\text{P-F}} = 941$)	-9.6, dt ($J_{\text{P-F}} = 941$)
HF	-189, s	-
$\text{CH}_3\text{CH}_2\text{F}$	-212.4, tq ($J_{\text{H-F}} = 47.1,$ 26.5)	-
$\text{RCH}_2\text{CH}_2\text{F}^1$	-226.3, tt ($J_{\text{H-F}} = 47.3,$ 29.3)	-

1) **R** is an unknown fragment



Scheme 2.6 Proposed mechanism for the reaction of diethyl carbonate with POF_3 to produce the observed alkyl fluorophosphates $\text{PO}(\text{OCH}_2\text{CH}_3)_2\text{F}$, $\text{PO}(\text{OCH}_2\text{CH}_3)\text{F}_2$, $\text{PO}_2(\text{OCH}_2\text{CH}_3)\text{F}^-$.

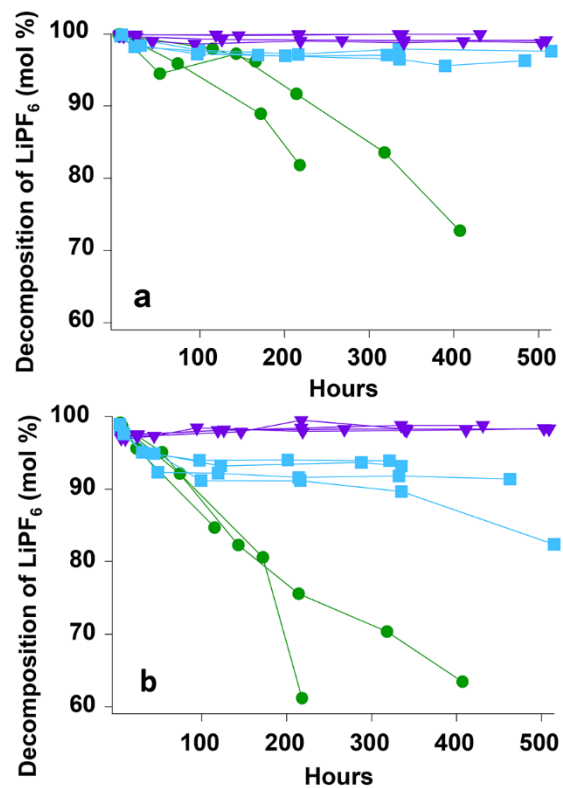


Figure 2.11 Decomposition of LiPF_6 in carbonate and organosilicon electrolytes at 100°C with (a) no added water and (b) 1000 ppm added water. Carbonate electrolytes (3:7 EC:DEC + 1 M LiPF_6) are circle markers (●), organosilicon glycol electrolytes (1 + 1 M LiPF_6) are square markers (■) and organosilicon nitrile electrolytes (3 + 1 M LiPF_6) are triangle markers (▼).

Quantification of LiPF_6 decomposition was calculated by $100 \times \text{Equation 1}$.

2.6 References

1. Brodd, R. J., Synopsis of the Lithium-Ion Battery Markets. In *Lithium-ion Batteries: Science and Technologies*, Yoshio, M.; Brodd, R. J.; Kozawa, A., Eds. Springer New York, NY, USA, 2010; pp 1-7.
2. Choi, D.; Wang, W.; Yang, Z., Lithium-ion Batteries: Advanced Materials and Technologies. In *Lithium-ion Batteries: Advanced Materials and Technologies*, Yuan, X.; Liu, H.; Zhang, J., Eds. CRC: Boca Raton, FL, USA, 2016; pp 1-51.
3. Pistoia, G., *Lithium-ion Batteries: Advances and Applications*. Elsevier: 2013.
4. Cao, C.; Wu, Y.; Ree, T. v., Applications of Lithium-Ion Batteries. In *Lithium-ion batteries: Fundamental and Applications*, Wu, Y., Ed. CRC: Boca Raton, FL, USA, 2015; pp 526-557.
5. Wang, B.; Yuan, X.; Zhao, S.; Wu, Y.; Ree, T. v., Liquid Electrolytes. In *Lithium-ion Batteries: Fundamentals and Applications*, Wu, Y., Ed. CRC Press: Boca Raton, FL, USA, 2015; pp 273-296.
6. Lex-Balducci, A.; Henderson, W.; Passerini, S., Electrolytes for Lithium-ion batteries. In *Lithium-Ion Batteries: Advanced Materials and Technologies*, Yuan, X.; Liu, H.; Zhang, J., Eds. CRC Press: Boca Raton, FL, USA, 2016; pp 147-169.
7. Belt, J. R.; Ho, C. D.; Miller, T. J.; Habib, M. A.; Duong, T. Q., The effect of temperature on capacity and power in cycled lithium ion batteries. *J. Power Sources* **2005**, *142* (1-2), 354.
8. Shim, J.; Kostecky, R.; Richardson, T.; Song, X.; Striebel, K. A., Electrochemical analysis for cycle performance and capacity fading of a lithium-ion battery cycled at elevated temperature. *J. Power Sources* **2002**, *112* (1), 222-230.
9. Aurbach, D.; Markovsky, B.; Rodkin, A.; Levi, E.; Cohen, Y. S.; Kim, H. J.; Schmidt, M., On the capacity fading of LiCoO₂ intercalation electrodes: the effect of cycling, storage, temperature, and surface film forming additives. *Electrochim. Acta* **2002**, *47* (27), 4291-4306.
10. Ramadass, P.; Haran, B.; White, R.; Popov, B. N., Capacity fade of Sony 18650 cells cycled at elevated temperatures: Part I. Cycling performance. *J. Power Sources* **2002**, *112* (2), 606-613.
11. Zhang, S. S.; Jow, T. R., Aluminum corrosion in electrolyte of Li-ion battery. *J. Power Sources* **2002**, *109* (2), 458-464.
12. Campion, C. L.; Li, W.; Lucht, B. L., Thermal Decomposition of LiPF₆-Based Electrolytes for Lithium-Ion Batteries. *J. Electrochem. Soc.* **2005**, *152* (12), A2327-A2334.
13. Plakhotnyk, A. V.; Ernst, L.; Schmutzler, R., Hydrolysis in the system LiPF₆—propylene carbonate—dimethyl carbonate—H₂O. *J. Fluorine Chem.* **2005**, *126* (1), 27-31.

14. Zhang, L.; Zhang, Z.; Haring, S.; Straughan, M.; Butorac, R.; Chen, Z.; Lyons, L.; Amine, K.; West, R., Highly conductive trimethylsilyl oligo(ethylene oxide) electrolytes for energy storage applications. *J. Mater. Chem.* **2008**, *18* (31), 3713-3717.
15. Zhang, L.; Lyons, L.; Newhouse, J.; Zhang, Z.; Straughan, M.; Chen, Z.; Amine, K.; Hamers, R. J.; West, R., Synthesis and characterization of alkylsilane ethers with oligo(ethylene oxide) substituents for safe electrolytes in lithium-ion batteries. *J. Mater. Chem.* **2010**, *20* (38), 8224-8226.
16. Chen, X.; Usrey, M.; Peña-Hueso, A.; West, R.; Hamers, R. J., Thermal and electrochemical stability of organosilicon electrolytes for lithium-ion batteries. *J. Power Sources* **2013**, *241*, 311-319.
17. Li, W.; Campion, C.; Lucht, B. L.; Ravdel, B.; DiCarlo, J.; Abraham, K. M., Additives for Stabilizing LiPF₆-Based Electrolytes Against Thermal Decomposition. *J. Electrochem. Soc.* **2005**, *152* (7), A1361-A1365.
18. Christe, K. O.; Dixon, D. A.; Schrobilgen, G. J.; Wilson, W. W., Tetrafluorophosphate Anion. *J. Am. Chem. Soc.* **1997**, *119* (17), 3918-3928.
19. Vortmann, B.; Nowak, S.; Engelhard, C., Rapid Characterization of Lithium Ion Battery Electrolytes and Thermal Aging Products by Low-Temperature Plasma Ambient Ionization High-Resolution Mass Spectrometry. *Anal. Chem.* **2013**, *85* (6), 3433-3438.
20. Campion, C. L.; Li, W.; Euler, W. B.; Lucht, B. L.; Ravdel, B.; DiCarlo, J. F.; Gitzendanner, R.; Abraham, K. M., Suppression of Toxic Compounds Produced in the Decomposition of Lithium-Ion Battery Electrolytes. *Electrochem. Solid-State Lett.* **2004**, *7* (7), A194-A197.
21. Aihara, Y.; Sonai, A.; Hattori, M.; Hayamizu, K., Ion Conduction Mechanisms and Thermal Properties of Hydrated and Anhydrous Phosphoric Acids Studied with ¹H, ²H, and ³¹P NMR. *J. Phys. Chem. B* **2006**, *110* (49), 24999-25006.
22. Cosgrove, S.; Rogers, L.; Hewage, C. M.; Malthouse, J. P. G., NMR Study of the Inhibition of Pepsin by Glyoxal Inhibitors: Mechanism of Tetrahedral Intermediate Stabilization by the Aspartyl Proteases. *Biochem.* **2007**, *46* (39), 11205-11215.
23. Fang, S.; Wang, G.; Qu, L.; Luo, D.; Yang, L.; Hirano, S.-i., A novel mixture of diethylene glycol diethylether and non-flammable methyl-nonafluorobutyl ether as a safe electrolyte for lithium ion batteries. *J. Mater. Chem. A* **2015**, *3* (42), 21159-21166.
24. Liu, Y.; Fang, S.; Luo, D.; Yang, L.; Hirano, S.-i., Safe Electrolytes for Lithium-Ion Batteries Based on Ternary Mixtures of Triethylene Glycol Dimethylether, Fluoroethylene Carbonate and Non-Flammable Methyl-Nonafluorobutyl Ether. *J. Electrochem. Soc.* **2016**, *163* (9), A1951-A1958.

25. Pietschnig, R.; Belaj, F.; Tirr e, J. J., Synthesis and Intermediates in the Formation of a Terphenyl-Substituted Silanetriol: Activation through Hypervalency. *Organometallics* **2004**, *23* (21), 4897-4901.
26. Brefort, J. L.; Corriu, R. J. P.; Guerin, C.; Henner, B. J. L.; Wong Chi Man, W. W. C., Pentacoordinated silicon anions: synthesis and reactivity. *Organometallics* **1990**, *9* (7), 2080-2085.
27. Barrelle, M.; B guin, C.; Tessier, S., Carbon-13 NMR of oxygenated derivatives of polyoxyethylenes. *Org. Magn. Resonance* **1982**, *19* (2), 102-104.
28. Gottlieb, H. E.; Kotlyar, V.; Nudelman, A., NMR Chemical Shifts of Common Laboratory Solvents as Trace Impurities. *J. Org. Chem.* **1997**, *62* (21), 7512-7515.
29. Wali, A.; Pillai, S. M.; Unnikrishnan, S.; Satish, S., HZSM-5 catalyzed cyclodehydration of diethylene glycol and its derivatives. *J. Mol. Catal. A: Chem.* **1996**, *109* (2), 149-155.
30. Rohan, R.; Kuo, T.-C.; Lin, J.-H.; Hsu, Y.-C.; Li, C.-C.; Lee, J.-T., Dinitrile–Mononitrile-Based Electrolyte System for Lithium-Ion Battery Application with the Mechanism of Reductive Decomposition of Mononitriles. *J. Phys. Chem. C* **2016**, *120* (12), 6450-6458.
31. Ue, M.; Sasaki, Y.; Tanaka, Y.; Morita, M., Nonaqueous Electrolytes with Advances in Solvents. In *Electrolytes for Lithium Ion Batteries*, Jow, T. R.; Borodin, O.; Xu, K.; Ue, M., Eds. Springer Science: New York, 2014; pp 93-166.
32. Liu, Y.; Fang, S.; Shi, P.; Luo, D.; Yang, L.; Hirano, S.-i., Ternary mixtures of nitrile-functionalized glyme, non-flammable hydrofluoroether and fluoroethylene carbonate as safe electrolytes for lithium-ion batteries. *J. Power Sources* **2016**, *331*, 445-451.
33. Ma, Q.; Mandal, B. K., Highly Conductive Electrolytes Derived from Nitrile Solvents. *J. Electrochem. Soc.* **2015**, *162* (7), A1276-A1281.
34. Pregosin, P. S., *NMR in Organometallic Chemistry*. John Wiley & Sons: Weinheim, Germany, 2012.
35. Cazes, J., *Ewing's Analytical Instrumentation Handbook*. 3rd ed.; CRC Press: Boca Raton, FL, USA, 2004.
36. Silverstein, R. M.; Webster, F. X.; Kiemle, D. J.; Bryce, D. L., *Spectrometric Identification of Organic Compounds*. John Wiley & Sons: 2014.
37. Berger, S.; Braun, S.; Kalinowski, H.-O., *NMR Spectroscopy of the Non-Metallic Elements*. Wiley: Chichester, West Sussex, UK, 1997.
38. Richards, S. A.; Hollerton, J. C., *Essential Practical NMR for Organic Chemistry*. John Wiley and Sons, ltd: 2011; p. 216. (accessed 10/05/2016).

39. Achiha, T.; Nakajima, T.; Ohzawa, Y.; Koh, M.; Yamauchi, A.; Kagawa, M.; Aoyama, H., Electrochemical Behavior of Nonflammable Organo-Fluorine Compounds for Lithium Ion Batteries. *J. Electrochem. Soc.* **2009**, *156* (6), A483-A488.
40. Achiha, T.; Nakajima, T.; Ohzawa, Y.; Koh, M.; Yamauchi, A.; Kagawa, M.; Aoyama, H., Thermal Stability and Electrochemical Properties of Fluorine Compounds as Nonflammable Solvents for Lithium-Ion Batteries. *J. Electrochem. Soc.* **2010**, *157* (6), A707-A712.
41. Suvorov, B., Intramolecular electronic interaction in a series of organosilicon compounds. *Russ. J. Gen. Chem.* **2006**, *76* (9), 1401-1406.
42. Voorhoeve, R. J. H., *Organohalosilanes: Precursors to Silicones*. Elsevier Publishing Company: Amsterdam, Netherlands, 1967.
43. Dolbier, W. R., Guide to Fluorine NMR for Organic Chemists. John Wiley and Sons: 2009; p. 256. (accessed 10/05/2016).
44. Tasaki, K.; Kanda, K.; Nakamura, S.; Ue, M., Decomposition of LiPF₆ and Stability of PF₅ in Li-Ion Battery Electrolytes: Density Functional Theory and Molecular Dynamics Studies. *J. Electrochem. Soc.* **2003**, *150* (12), A1628-A1636.
45. Janzen, A. F.; Ou, X.; Sowa, M. G., Reaction mechanisms of phosphorus fluorides: An ab initio study. *J. Fluorine Chem.* **1997**, *83* (1), 27-30.
46. Ceccarelli, G.; Andruzzi, F., ¹⁹F NMR spectroscopy of the PF₅/3-oxabicyclo [3.2.2]nonane system. *Die Makromol. Chem.* **1979**, *180* (5), 1371-1374.
47. Zhang, S. S.; Xu, K.; Jow, T. R., A Thermal Stabilizer for LiPF₆-Based Electrolytes of Li-Ion Cells. *Electrochem. Solid-State Lett.* **2002**, *5* (9), A206-A208.
48. Sloop, S. E.; Pugh, J. K.; Wang, S.; Kerr, J. B.; Kinoshita, K., Chemical Reactivity of PF₅ and LiPF₆ in Ethylene Carbonate/Dimethyl Carbonate Solutions. *Electrochem. Solid-State Lett.* **2001**, *4* (4), A42-A44.
49. Sloop, S. E.; Kerr, J. B.; Kinoshita, K., The role of Li-ion battery electrolyte reactivity in performance decline and self-discharge. *J. Power Sources* **2003**, *119-121*, 330-337.
50. Li, W.; Lucht, B. L., Inhibition of solid electrolyte interface formation on cathode particles for lithium-ion batteries. *J. Power Sources* **2007**, *168* (1), 258-264.
51. Wilken, S.; Treskow, M.; Scheers, J.; Johansson, P.; Jacobsson, P., Initial stages of thermal decomposition of LiPF₆-based lithium ion battery electrolytes by detailed Raman and NMR spectroscopy. *RSC Adv.* **2013**, *3* (37), 16359-16364.

Chapter 3. Mechanistic Insights into High Oxidative Stability of Organosilicon Nitrile Electrolytes for Lithium-ion Batteries

3.1 Introduction

The lithium-ion battery is an essential technology to meet current energy storage needs. Most consumer electronics and electric vehicles are powered by lithium-ion batteries. However, the current technology is limited by the thermal and electrochemical window of stability of the lithium-ion electrolyte.¹⁻⁴ Lithium hexafluorophosphate in carbonate solvents is the most commonly used battery electrolyte system because of its high solubility, conductivity, and minimal salt corrosion of aluminum current collectors.⁵ Despite their beneficial properties, these electrolytes are unstable at the highly reducing and oxidizing electrode interfaces.^{1-2,6-9} Although reactions between the electrolyte components and electrodes can lead to electrochemically protective solid-electrolyte interphase (SEI) layers, rarely is ideal electrode protection provided, leading to continuing parasitic electrochemical reactions even after the first few battery formation cycles that release gas, increase impedance, and lead to capacity fade.^{6,10-14} In order to advance lithium-ion technology towards greater device lifetime and safety at higher voltages, it is therefore essential to design electrolyte systems resistant to these degradation processes, and to understand the mechanisms of electrolyte degradation under high voltage electrochemical conditions.

Organosilicon solvents have previously shown promise as thermally and electrochemically stable battery electrolytes.¹⁵⁻¹⁹ Zhang et al. demonstrated that the Si atom in siloxane glycols imparted greater oxidative stability when compared with analogous carbon- and germanium-containing molecules.¹⁷ Moreover, silicon-containing glycols exhibited impressive hydrolytic stability even at 20% v/v added water when a propyl spacer was added between the silicon and electronegative functionality.¹⁶ More recently, we showed that organosilicon glycols and nitriles protect LiPF₆ against the catalytic cycle of thermal degradation that occurs in carbonates by

sequestering the reactive degradation intermediate, PF₅, via complexation.¹⁹ While these studies provided important insights into the thermal decomposition pathways of organosilicon electrolytes, in battery applications decomposition reactions can also be initiated electrochemically, necessitating the investigation of electrochemical mechanisms of degradation in organosilicon electrolytes, and how molecular functionality can be used to increase stability. Previous studies with carbonates,²⁰⁻²¹ ethers,²⁰ and sulfones²² have shown that fluorination can increase oxidative stability, suggesting one possible route towards tuning electrochemical stability in organosilicons. Since there have been no previous studies on the oxidative stability of organosilicon nitriles, it is also important to begin by understanding the intrinsic electrolyte mechanisms of oxidation through the use of a nominally inert positive electrode such as platinum.

In this paper, we describe fundamental studies of the oxidative stability of organosilicon nitriles and how that stability varies as the function of the degree of fluorination of the Si atom. Using a set of four organosilicon nitriles we characterize the intrinsic high-potential reactivities of the organosilicon nitrile fluorination series against platinum electrodes. To map out the oxidative degradation pathways when these molecules are used as electrochemical solvents, we used density functional theory (DFT) calculations, nuclear magnetic resonance (NMR) spectroscopy and x-ray photoelectron spectroscopy (XPS). Computation of the oxidation potentials of organosilicon molecules in this study indicate that thermodynamically, fluorination increases oxidative stability. Experimentally, however, we found as the degree of silicon fluorination increases, the potential of electrolyte oxidative breakdown decreases, and all organosilicon nitriles studied herein have exceptional oxidative stability (>6.8 V vs Li/Li⁺). Our results show that the electrooxidation mechanisms of organosilicon nitrile compounds are driven by organosilicon reaction with fluorine to form fluorosilane, concurrent with formation of a thin electrode surface film. We propose that

formation of this surface film delays the onset of oxidative breakdown, resulting in the observed high voltage stability of these organosilicon nitriles.

3.2 Materials and Methods

3.2.1 Chemicals

All chemicals were anhydrous or dried and stored in an argon-atmosphere glovebox immediately upon receipt. The organosilicon compounds were received from Silatronix, Inc. Lithium hexafluorophosphate was purchased from BASF. Ethylene carbonate and diethyl carbonate were purchased from SoulBrain. Anhydrous dimethyl carbonate, butyronitrile, and propionitrile were purchased from Sigma-Aldrich. All compounds were used as received.

3.2.2 DFT Calculation Methods

All calculations were performed with Gaussian 09 software²³ on the UW-Madison Chemistry Department High-Performance Computing cluster. The structures were optimized with B3LYP with a 6-31++G** basis set. Frequency analyses showed that the optimized structures had no negative eigenvalues. Enthalpies and Gibbs Free energies were calculated at 298 K. Solvent effects were tested through geometry optimization with a Polarizable Continuum Model (PCM), utilizing the dielectric constants for each solvent molecule shown in Table S3.1. Oxidation potentials were calculated and then referenced to Li/Li⁺ using the following equation:²⁴⁻²⁵

$$E_{\text{ox,Li/Li}^+}(\text{M}) = \frac{G(\text{M}^+) - G(\text{M})}{F} - 1.4 \text{ eV}$$

Where $E_{\text{ox,Li/Li}^+}(\text{M})$ is the calculated oxidation potential of species M referenced to the Li/Li⁺ voltage scale, $G(\text{M})$ is the free energy of the species M at the energy-minimized geometry, $G(\text{M}^+)$ is the free energy of the same species as a cation either at the same geometry (vertical oxidation) or after allowing molecular relaxation to a new geometric energy minimum (adiabatic oxidation),

and F is Faraday's constant. The shift of 1.4 V represents the difference in energy between the Li/Li^+ and the vacuum level.²⁶

3.2.3 Electrochemical tests

All electrochemical samples were prepared inside an argon-atmosphere glovebox. Linear Sweep Voltammetry (LSV) and Cyclic Voltammetry (CV) were performed on a Gamry Interface 1000E Potentiostat inside an argon-atmosphere glovebox. The samples were prepared in three-electrode cells with a platinum disk working electrode (1.6 mm diameter), Li foil reference electrode, and Li foil counter electrode. LSVs were started at the open circuit voltage of each sample and swept to 8 V vs Li/Li^+ at 10 mV/s. CVs were started at 3 V vs Li/Li^+ and swept past the pre-breakdown peak voltage of each electrolyte at 1 mV/s, 10 mV/s, and 100 mV/s. Voltage-hold experiments were run on an Arbin battery cycler, starting at the open circuit voltage and sweeping to the final hold voltage at 1 mV/s, followed by holding at final voltage for 24 hours. The samples were prepared in custom hermetically-sealed polyetheretherketone (PEEK) electrochemical cells with a platinum disk working electrode (0.635 cm active diameter), platinum disk counter electrode, and lithium foil reference electrode. The design of these electrochemical cells is shown in more detail in the Supporting Information (Figure S3.1). After the voltage hold, the cells were transferred back into the glovebox and the electrolyte and electrodes were removed for further analysis.

3.2.4 Nuclear Magnetic Resonance (NMR) Spectroscopy

Electrolyte for NMR analysis was extracted from the electrochemical cell in an argon-atmosphere glovebox and transferred into polytetrafluoroethylene/fluorinated ethylene polypropylene copolymer (PTFE-FEP) 5 mm tube liners (Wilmad Glass), which were placed into 7" 5 mm NMR tubes and sealed with Superior High Pressure Caps (Wilmad Glass). NMR analysis

was performed on these samples immediately after removing from the glovebox. Samples were analyzed with Bruker Avance III 500 MHz (CryoProbe Prodigy or BBFO PLUS probes) or 600 MHz (TCI-F probe) spectrometers. ^1H -NMR spectra were collected with 16 scans. ^{19}F -NMR spectra were collected with 64 scans. All spectra were referenced using a substitution reference standard of 1% TMS in CDCl_3 and processed with MestreNova 9.1.0. The calibration was applied during processing by absolute referencing.²⁷ Molar concentrations of individual species were determined by integration of peak areas, normalized by the stoichiometry-weighted sum of the areas of PF_6 and all observed PF_6 degradation products, as described previously.¹⁹

3.2.5 X-ray Photoelectron Spectroscopy (XPS)

Electrodes for XPS analysis were extracted from the electrochemical cell in an argon-atmosphere glovebox and rinsed three times with 2 mL anhydrous dimethyl carbonate and dried under vacuum. The electrodes were sealed in a Vacuum Transfer Module (Thermo Fisher) and transferred to the XPS without exposure to air. XPS analysis was performed on a Thermo Scientific K-alpha XPS with an Al x-ray source. XPS data were fit using CasaXPS software and referenced to the adventitious carbon peak at 284.8 eV. Survey spectra were collected with 92.9 eV pass energy from 0 to 1400 eV binding energy, and individual spectra were collected with 50 eV pass energy. To calculate atom percentages, all peaks in each individual spectrum were fit by CasaXPS, and the sum of these peak areas was divided by the total peak areas of all elements and multiplied by 100.

3.3 Results and Discussion

In this study, we investigated the fundamental mechanisms of high-voltage breakdown for organosilicon nitrile electrolytes, through computation of oxidation potentials and voltammetric experiments against inert platinum electrodes followed by detailed mechanistic

analysis of the oxidation breakdown products with NMR and XPS. We studied the impact of fluorination at the silicon on the electrolyte oxidation potential and mechanisms of oxidative degradation.

Previous research has shown that fluorination can significantly increase the oxidation stability of ether, carbonate, and sulfone lithium-ion battery solvents.²⁰⁻²² To discover the impact of fluorination on high-voltage stability with organosilicon nitriles, we investigated the series of four organosilicon nitriles (OSN) shown in Figure 3.1. Within this series, the organosilicon nitriles under study range from non-fluorinated organosilicon nitrile (NoF-OSN) to tri-fluorinated organosilicon nitrile (3F-OSN).

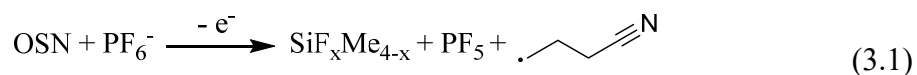
3.3.1 Computation of organosilicon oxidation potentials

Computational studies have been successfully utilized for screening potential lithium-ion electrolyte solvents based on their calculated electrochemical potentials, and understanding mechanisms of electrochemical decomposition.^{25, 28-29} We used DFT calculation methods established previously to calculate the oxidation potentials of OSN molecules, as described in detail in the experimental section. Previous studies have found that calculated oxidation potentials of solvent molecules are strongly influenced by the surrounding molecules, including other solvent molecules, the anion salt, and the lithium ion.^{25, 30-31} We calculated the vertical and adiabatic oxidation potentials of the four OSN molecules as described in the Experimental Section, and tested the influence of surrounding salt and solvent molecules on oxidation with the following cases: (1) a single isolated OSN molecule (“OSN isolated”); (2) a pair of interacting OSN molecules (“OSN+OSN”), and (3) a single OSN molecule interacting with a single PF_6^- anion (“OSN+ PF_6^- ”). Figure 3.2 shows the resulting oxidation potential $E_{\text{ox, Li/Li}^+}$ for each case.

As fluorination of the Si atom increases, a corresponding increase was calculated for all vertical and adiabatic oxidation potentials of OSN, OSN+OSN, and OSN+PF₆⁻. Each additional fluorine at the silicon adds 0.1-0.7 V to the molecule's oxidation potential. Increased oxidation potential with fluorination of a solvent molecule is consistent with previous reports on the computational calculations and experimental measurements of ether,²⁰ carbonate,^{20-21, 32} and sulfone²² solvents. This trend may be attributed to the highly electronegative nature of the fluorine atom, increasing the barrier to electron removal. Our computational results predict that increasing fluorination at the silicon should lead to organosilicon nitrile solvents with greater oxidative stability.

The energy difference between the vertical and adiabatic oxidation potentials reflects the reorganization energy contribution to the adiabatic oxidation potential, due to molecular relaxation.²⁸ For all isolated OSN and OSN+OSN cases, the vertical oxidation potentials ($E_{\text{ox, vertical}}$) are greater than the adiabatic oxidation ($E_{\text{ox, adiabatic}}$) by less than 0.9 V. The relatively small energy difference reflects the minor contribution of molecular relaxation to the oxidation energies in these cases. By contrast, for OSN+ PF₆⁻ the differences between $E_{\text{ox, vertical}}$ and $E_{\text{ox, adiabatic}}$ for OSN+PF₆⁻ are 2.0-2.6 eV, which is due to the significant reorganization energy involved in the release of a molecular fragment during adiabatic oxidation. As shown in Figure 3.3 and Equation 3.1, for all OSN+PF₆⁻, oxidation of the two adjacent molecules followed by geometry optimization leads to predicted structures in which the OSN molecules have abstracted a fluorine from PF₆⁻ and cleaved the Si-C(methylene) bond in a coupled oxidation-fluorination reaction. This reaction forms PF₅, propyl nitrile radical, and fluorosilane as products. The calculated $E_{\text{ox, adiabatic}}$ for each OSN+PF₆⁻ is more than 1.2 V lower than the $E_{\text{ox, adiabatic}}$ for the same molecule calculated in an isolated geometry (OSN) or with an adjacent solvent molecule

(OSN+OSN), indicating that when the solvent is oxidized with a neighboring PF_6^- , the mechanism of coupled oxidation-fluorination will occur at a lower potential than a mechanism where an electron is abstracted from the organosilicon nitrile molecule with no coupled fluorination.



3.3.2 Linear Sweep Voltammetry analysis

To characterize the oxidative stability experimentally, we used linear sweep voltammetry (LSV). Figure 3.4 shows the LSV of each OSN with 1 M LiPF_6 showing the onset of full electrolyte breakdown and, in the inset, smaller pre-breakdown features on an expanded vertical scale. The voltammograms were scanned from the open circuit potential to 8 V at a rate of 10 mV/s using a Pt disk working electrode and Li foil as reference and counter electrodes. We define the experimental oxidation potential as the voltage at which the current density is 1 mA/cm^2 . This density was chosen for consistency with prior studies defining characterizing the oxidation potentials of other electrolytes.³³⁻³⁴ The voltammograms in Figure 3.4 show that all OSN have high oxidative stability, with oxidation potentials above 6.8 V vs Li/Li^+ . Within the OSN fluorination series, decreasing the extent of silicon fluorination increases the oxidation potential of the organosilicon nitriles, with the oxidation of 3F-OSN at 6.9 V, 2F-OSN at 7.1 V, 1F-OSN at 7.4 V, and NoF-OSN at 8.0 V. The LSV of EC/DEC 3/7 under the same conditions oxidizes at 6.7 V (Figure S3.3), showing that all organosilicon nitriles tested here have greater oxidative stability than the carbonate control.

In addition to the onset of full electrolyte breakdown, NoF-OSN, 1F-OSN, and 2F-OSN electrolytes have small ($<0.3 \text{ mA}/\text{cm}^2$) features in the voltammograms at voltages lower than the electrolyte breakdown potential (Figure 3.4 inset). These current peaks occur at 5.2 V for NoF-

OSN, 5.6 V for 1F-OSN, and 6.2 V for 2F-OSN, and at more positive potentials the current decreases towards zero again in each electrolyte. The role these features play in the oxidation of OSN species is discussed later in this paper.

3.3.3 Voltage hold analysis of oxidation degradation mechanisms

Our observation that fluorinating the Si atom reduces the electrochemical stability toward oxidation is contrary to prior studies of most molecular systems, as fluorination typically makes molecules more resistant to oxidation.²¹⁻²² In order to understand why OS compounds exhibit the opposite trend, we made further efforts to understand the mechanism of oxidation in OSN electrolytes. We developed a custom hermetically sealed electrochemical cell (shown schematically in Figure S3.1) with an electrolyte volume of 750 μ L to enable ex situ NMR analysis of the products of oxidative degradation at different voltages. This cell used platinum working electrodes and counter electrodes and a lithium foil reference electrode. To validate that the electrochemical behavior of the electrolytes in these cells matched the behavior observed in Figure 3.1, we used linear sweep voltammetry. The results, shown in Supporting Information Figure S3.2, show that both methods show the same electrochemical behavior of the electrolyte. We analyzed the anodic degradation species generated at a given voltage by ramping the voltage of the cell from the open-circuit potential at a rate of 1 mV/s to the final voltage, and the cell was held at that voltage for 24 hours. After voltage treatment, the electrolyte sample was extracted in an argon-atmosphere glovebox and transferred to an NMR tube for analysis.

Figure S3.4 shows the full ^{19}F -NMR spectra of the NoF-OSN (S3.4a), 1F-OSN (S3.4b), and 2F-OSN (S3.4b) after voltage holds at the prebreakdown peak of each electrolyte (top spectrum of each figure), a voltage prior to the onset of prebreakdown peak current (middle spectrum), and a control electrolyte that had no voltage applied to the electrochemical cell

(bottom spectrum). These spectra show that there is a peak between -130 and -160 ppm in each electrolyte, as indicated by the red arrows, that increases right at the prebreakdown voltage. Figures 3.5a-c show each of these peaks in detail as multiplets with coupling constants $J=4-7$ Hz. As shown by the same chemical shift range and couplings constants of the solvents themselves (Table S3.2), the multiplets are in the appropriate chemical shift and coupling constant range for fluorinated organosilicons coupling to alkyl hydrogens.³⁵ Electrolytes extracted after a voltage hold lower than the prebreakdown potential (Figure S3.4 middle spectra) also show increased fluorophosphate species, as well as an increase in the peak corresponding to fluorination at the silicon with loss of a methyl group in NoF-OSN and 1F-OSN, to form 1F-OSN and 2F-OSN respectively. However, the peaks indicated by the red arrows represent the primary species that increase right at the prebreakdown voltage hold, and therefore we identified and calculated the concentration of these species as a function of voltage in order to understand their relation to the redox reaction occurring at the prebreakdown peak in each electrolyte. The results of this analysis are shown in Figure 3.5.

In NoF-OSN, the multiplet formed at the prebreakdown voltage has a chemical shift of -156.7 ppm with $J=7.5$ Hz shown in Figure 3.5a, which we attributed to fluorotrimethylsilane based on previous literature reporting ^{19}F -NMR of this species.³⁶ In 1F-OSN, the multiplet shown in Figure 3.5b has a chemical shift of -130.7 ppm with $J=6.3$ Hz, consistent with prior studies of difluorodimethylsilane.³⁵⁻³⁶ The prebreakdown peak oxidation species in 2F-OSN appears at -134.2 ppm (quartet, $J=4.2$ Hz) shown in Figure 3.5c; we attribute this species to trifluoromethylsilane based on prior studies.³⁵⁻³⁶ Each of these species represents the fluorosilane ($\text{SiF}_x\text{Me}_{4-x}$) that results from fluorination at the silicon and Si-methylene bond cleavage, a

reaction product consistent with the computationally-predicted mechanism of OSN+PF₆⁻ oxidation shown in Equation 3.1.

Figure 3.5e shows the SiF_xMe_{4-x} concentration as a function of voltage for each OSN, calculated as each species' peak area in ¹⁹F-NMR normalized to the total area of the LiPF₆ peak and its decomposition product peaks (see Experimental Section for more details). In 3F-OSN we also quantified the concentration of SiF₄, which species appears as a singlet at -163.3 ppm as shown in Figure 3.5d, consistent with previous reports.³⁶ The voltages indicated by the dashed lines represent the pre-breakdown peak voltage for each OSN, as shown in the Figure 3.4 inset. As indicated by the dashed lines, the concentration of each small fluorosilane increases for NoF, 1F, and 2F-OSN electrolytes at the same voltage as the corresponding pre-breakdown peak voltage shown in the Figure 3.4 inset. 3F-OSN, which does not have an observable pre-breakdown peak, shows an increase in SiF₄ at 5.8 V, where the current begins to increase during full electrolyte breakdown, shown in the LSV of Figure 3.4 inset. We previously reported the formation of fluorotrimethylsilane as a thermal degradation product of the NoF-OSN electrolyte.¹⁹ As is shown in Figure 3.5e with the increase of fluorosilane as voltage increases, we show that in addition to the thermal mechanism of fluorosilane formation,¹⁹ there is also an oxidatively-induced pathway for all OSN electrolytes.

As the Figure 3.4 inset shows, the pre-breakdown features occur at different voltages for each electrolyte: as the degree of fluorination is increased, the oxidative stability is also increased. This trend matches the oxidation potential trend predicted computationally in Figure 3.2. Additionally, the chemical identity of the degradation products observed in Figure 3.5a are consistent with those expected from our calculations predicting a coupled oxidation-fluorination mechanism to produce fluorosilane. The experimental and computational data therefore show

that the organosilicon nitriles studied here undergo anodic fluorination at the pre-breakdown peak voltage and likely release a propyl nitrile radical as shown in Scheme 3.1. This mechanism may occur with a fluorine abstracted directly from PF_6 as shown in the computational study and Equation 3.1, or through free fluoride. Previous studies demonstrating the formation of fluorosilanes from oxidation of tetraalkylsilanes in the presence of fluoride are consistent with our proposed mechanism of coupled oxidation-fluorination.³⁷

If the propyl nitrile radical proposed in Scheme 3.1 remained in solution, it might be expected to extract a hydrogen to form an alkyl nitrile molecule such as butyronitrile, which would produce distinct peaks in the ^1H -NMR spectra. Figure 3.6a shows the ^1H -NMR of commercial butyronitrile added to a pristine sample of 1F-OSN with 1 M LiPF_6 and the 3 peaks from distinct butyronitrile hydrogens that appear at 2.6 ppm (methylene adjacent to the nitrile, $\text{CH}_3\text{CH}_2\text{CH}_2\text{CN}$), 1.9 ppm (middle methylene, $\text{CH}_3\text{CH}_2\text{CH}_2\text{CN}$), and 1.3 ppm (terminal methyl, $\text{CH}_3\text{CH}_2\text{CH}_2\text{CN}$) in the organosilicon nitrile solvent. Since butyronitrile produced from Scheme 3.1 should be equivalent to the concentration of $\text{SiF}_x\text{Me}_{4-x}$ detected in the ^{19}F -NMR spectra, Figure 3.6b shows that commercial butyronitrile added to 1F-OSN with 1 M LiPF_6 at a concentration of 6×10^{-4} M is above the limit of detection. Additionally, Figure 3.6k shows butyronitrile added to a pristine sample of 3F-OSN + 1 M LiPF_6 to show any changes in the butyronitrile peak chemical shifts due to the different solvent. In this solvent, the butyronitrile peaks appear at 2.6 ppm, 1.8 ppm, and 1.2 ppm.

These butyronitrile-containing standards are compared in Figures 3.6c-j to the ^1H -NMR spectra of all OSN electrolytes, before and after a voltage hold at the pre-breakdown peak voltage. Some regions of the expected butyronitrile peaks overlap with chemical shifts with the solvent; however, the butyronitrile methyl peak region is clearly visible in 1F-OSN and 3F-OSN

and no change is observed in these regions before and after a voltage hold. While we cannot conclusively say that butyronitrile doesn't appear in solution for NoF-OSN and 2F-OSN due to peak overlap, we see no evidence of its formation in these electrolytes. Furthermore, we can state conclusively that butyronitrile is not formed in solution in 1F-OSN at the prebreakdown potential, suggesting a different fate for the propyl nitrile expected to be formed in Scheme 3.1. One possibility is adsorption or reaction of the nitrile fragment with the electrode surface.

The starting reactants shown in Scheme 3.1 are the main solvent species in each electrolyte (not additives or impurities). Yet, the pre-breakdown feature is clearly a peak and not a continuous current onset, since as shown in the Figure 3.4 inset the current reaches a maximum then decreases, and the onset of full electrolyte breakdown occurs at a higher potential. These data show the pre-breakdown redox event to be self-limiting, indicating the electrode surface becomes protected from further solvent decomposition. We performed CV on NoF-OSN and 1F-OSN electrolytes to test the rate dependence of the pre-breakdown peak (Figure S3.5) and found that the peak current has a linear relationship with scan rate, characteristic of a surface-limited and not diffusion-limited process.³⁸ These data support our hypothesis that the pre-breakdown peak and subsequent higher potential of full oxidative breakdown may involve formation of a protective surface layer.

3.3.4 Electrode surface species analysis by XPS

Based on the evidence that the pre-breakdown peak is surface-limited reaction and lack of evidence of alkylnitriles in solution by ¹H-NMR, we examined the electrode surfaces after the voltage holds with x-ray photoelectron spectroscopy (XPS) to assess the formation of surface species from electrolyte decomposition. The electrodes were rinsed in dimethyl carbonate and dried under vacuum before transferring to the XPS using an air-free sample holder. We then

analyzed the atomic percent of silicon and nitrogen in the composition of the surface layers, since these elements provide unique indicators of whether the organosilicon nitrile solvent molecules form part of the surface layer, yielding the result shown in Figure 3.7. The calculation of atomic percent is described in detail in the Experimental Section.

Figure 3.7a shows the changes in % atomic concentration of silicon as a function of voltage, while Figure 3.7b shows the same analysis for nitrogen. As Figures 3.7a and 3.7b show, the silicon % remained 0 for NoF-OSN and decreases in 1F-OSN and 2F-OSN at the pre-breakdown peak voltage relative to the voltage immediate prior. By comparison, the nitrogen % increased relative to the earlier voltage from 4.0% to 6.5% for NoF-OSN; 5.5% to 9% for 1F-OSN; and 6.0% to 7.6% for 2F-OSN. If the propyl nitrile radical produced in Scheme 3.1 were to deposit on the surface, the electrode surface composition would be expected to show an increase in the % concentration of nitrogen at this potential, without a corresponding increase in silicon, consistent with the XPS results shown in Figures 3.7b-3.7c. The increase in nitrogen species from the control sample to the pre-breakdown peak voltage (5.6 V) can be seen in the N1s spectra of NoF-OSN (Figure 3.7c), 1F-OSN (Figure 3.7d), 2F-OSN (Figure 3.7e), as well as 3F-OSN at 5 V, lower than the electrolyte breakdown potential (Figure 3.7f). The nitrogen peaks at the prebreakdown voltages are fit with two components at 399.2 eV and 400.2 eV (NoF-OSN), 399.2 eV and 400.6 eV (1F-OSN), 399.1 eV and 400.7 eV (2F-OSN), and 399.8 eV and 401.2 eV (3F-OSN) binding energies. Literature of binding energies for different nitrogen functional groups report imines, imides, lactams, amines, amides, nitriles, and nitrosos all within the narrow range 399.1-400.4 eV, with varying binding energies of adsorbed nitriles reported (after scaling to adventitious carbon at 284.8 eV) from 399.3 to 400.4 eV.³⁹⁻⁴² Therefore, we do not attempt to assign the nitrogen components to specific functional groups. Furthermore, due to the low signal-

to-noise of the control sample nitrogen signal, it is not conclusive whether there are two nitrogen components in the control sample as well. However, overall the nitrogen and silicon spectra show that the surface film formed during the pre-breakdown peak reaction contains nitrogen but not silicon.

The percent composition of additional elements (fluorine, lithium, and phosphorus) forming part of the surface film are analyzed as a function of voltage in Figure S3.7. Unlike N1s and Si2p, there are no consistent trends in the atomic percentage of these elements observed at the prebreakdown peak voltage.

In addition to surface composition analysis, we calculated the thickness of surface species from the attenuation of the platinum substrate signal according to Equation 3.2:⁴³

$$I = I_0 \exp(-d/[L \cdot \cos(\theta)]) \quad (3.2)$$

Where I is the attenuated platinum 4f signal intensity, I_0 is the (non-attenuated) platinum signal intensity on a bare platinum sample, d is the thickness of a surface film in nanometers, L is the surface film attenuation length in nanometers, and θ is the electron emission angle. As determined by Seah,⁴³ L can be estimated to good accuracy as Equation 3.3:

$$L = (0.65 + 0.007 \cdot KE_{Pt}^{0.93}) / Z^{0.38} \quad (3.3)$$

Where L is in nanometers, KE_{Pt} is the kinetic energy of the platinum 4f peak in eV, and Z is the average atomic number of the surface layer. We used a Z value of 6 since the primary surface film components by atomic concentration were carbon, lithium, and fluorine.

Table 3.1 shows the surface layer thickness for OSN samples held at the indicated voltages for 24 hours, obtained by measuring the Pt intensity (I) from the samples, and a control sample of clean Pt (I_0), and using Equations 3.2 and 3.3. Control samples that were exposed to the electrolyte with no applied voltage show 0.3-2.2 nm of surface species even without applied voltages, likely the result of physisorbed electrolyte species remaining even after the DMC rinse

described in the experimental section. After polarizing the electrode to a moderately positive potential (below the potential at which the pre-breakdown peaks are observed), the surface film thickness remained below 2 nm for NoF, 1F, and 2F-OSN. Increasing the voltage to the pre-breakdown peak voltage resulted in an increase in surface film thickness for each of these electrolytes, suggesting formation of a surface film concurrent with the pre-breakdown peak and consistent with the rate-dependent CV data in Figure S3.5 that indicated a surface-limited redox reaction.

The mechanism shown in Scheme 3.1 predicts that oxidation should be accompanied by the formation of propyl nitrile radicals. Yet, in the $^1\text{H-NMR}$ spectra in Figure 3.6, we do not observe alkyl nitrile species. The absence of alkyl nitriles in solution and the increase of nitrogen % in the surface film at the pre-breakdown peak voltage suggests that the propyl nitrile radical is forming part of the surface film. Previous studies on cyano-containing electrolytes and additives have shown that under oxidizing conditions nitriles frequently form surface layers that inhibit further electrolyte oxidation.⁴⁴⁻⁴⁹ Various mechanisms have been proposed to explain this phenomenon, including nitrile adsorption,⁴⁶ complexation to electrode metal atoms blocking active sites,^{44, 49} and oxidation to form a thin protective layer.^{45, 47-48}

Our results show that OSN compounds produce surface layers on the positive electrode as the voltage increases. While we have not examined the impact of these layers on battery performance, our data show that the pre-breakdown peak observed in our electrochemical studies arises from a surface-limited oxidation reaction associated with formation of the fluorosilane. Furthermore, the XPS attenuation data and the N(1s) spectra show the electrochemical processes at the pre-breakdown peak lead to the formation of an N-containing surface layer. Therefore, we propose that the increased experimental oxidative stability of organosilicon nitriles relative to the

oxidation potentials predicted by DFT derives from the ability of the solvent molecule to react with fluoride ions or the PF_6^- ion to form fluorosilane and a propyl nitrile radical, leading to a self-limited surface protecting film that delays the bulk electrolyte oxidative degradation.

3.4 Conclusions

In this chapter, we present a series of four organosilicon nitriles with high intrinsic oxidative stability ($> 6.8 \text{ V vs Li/Li}^+$) against platinum electrodes, exceeding the oxidation potentials predicted by DFT calculations. These organosilicon nitriles contain 0-3 fluorines substituted at the silicon, and we show that these electrolytes also have an unusual trend of increasing oxidative stability with decreasing fluorination. NMR, XPS, and electrochemical data indicate that the high oxidative stability of these electrolytes is associated with a self-limiting surface oxidation reaction that produces a fluorosilanes in solution and a thin protective surface film on the electrode that delays the onset of full electrolyte breakdown. The anodic fluorination mechanism of fluorosilane formation is confirmed by DFT calculations and is seen experimentally at voltages that increase with increasing degree of solvent fluorination, consistent with the trend predicted by computation.

In order to achieve a future of energy storage where battery cells maintain high performance at high voltages and at elevated temperatures, new electrolytes must be pioneered that evince advanced stability properties. The superior oxidative stability of low-fluorine organosilicon nitriles shown in this study, and the high thermal stability of fluorinated organosilicon nitriles shown previously,^{15, 19} together highlight the potential of organosilicon nitriles with 1-2 fluorines to provide exceptional stability when used in lithium-ion battery cells.

This study of the intrinsic stability and decomposition mechanisms of organosilicons can inform future research in more complex electrolyte and electrode systems.

3.5 Figures

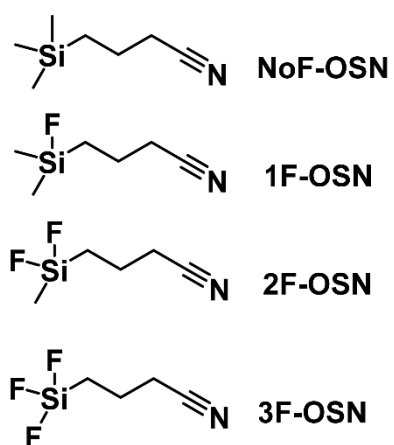


Figure 3.1 Chemical structures of the OSN solvent series

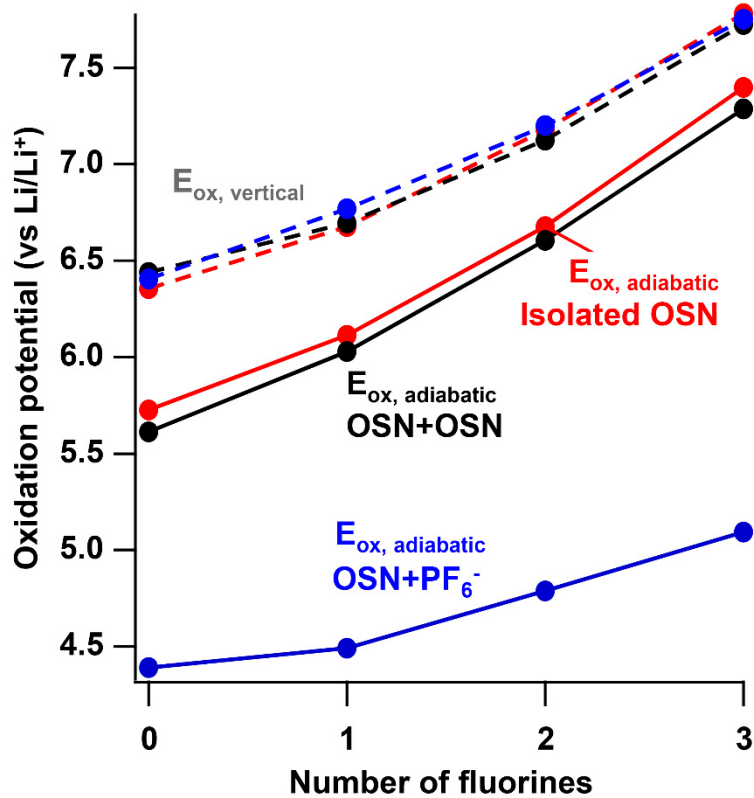


Figure 3.2 Calculated oxidation potentials of isolated OSN (red), OSN+OSN (black), and OSN+PF₆⁻ (blue) as a function of fluorination at the silicon: vertical oxidation (dashed lines) and adiabatic oxidation (solid lines)

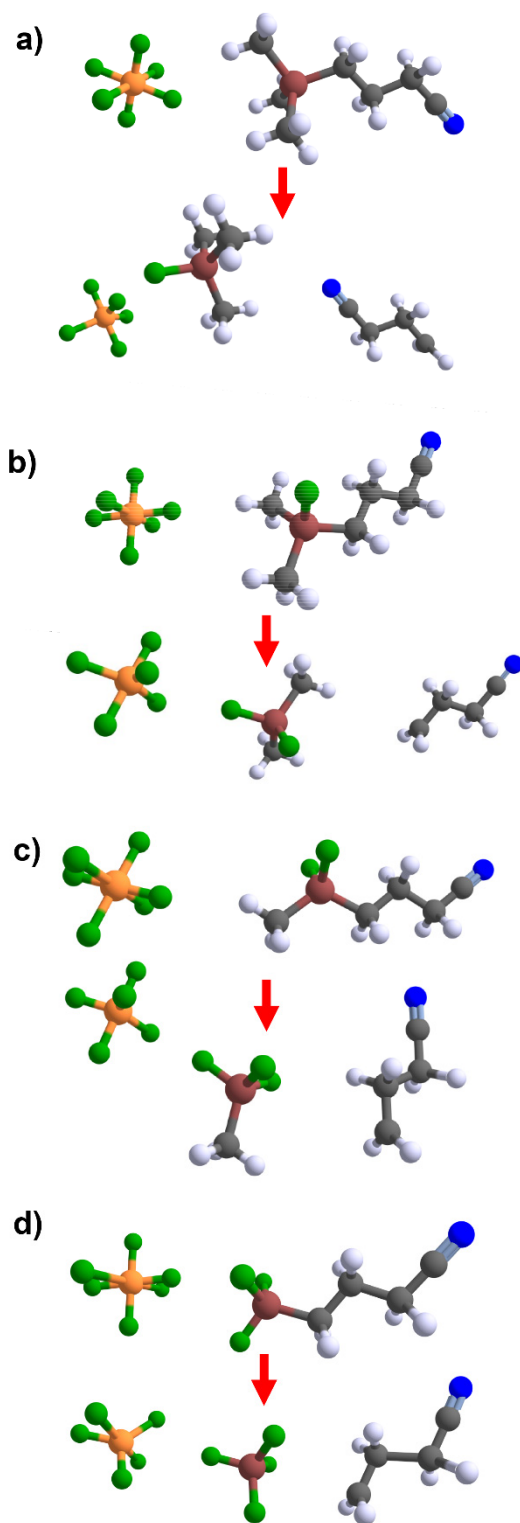


Figure 3.3 Changes from starting geometry to final optimized geometry in adiabatic PCM

oxidation of (a) NoF-OSN, (b) 1F-OSN, (c) 2F-OSN, and (d) 3F-OSN

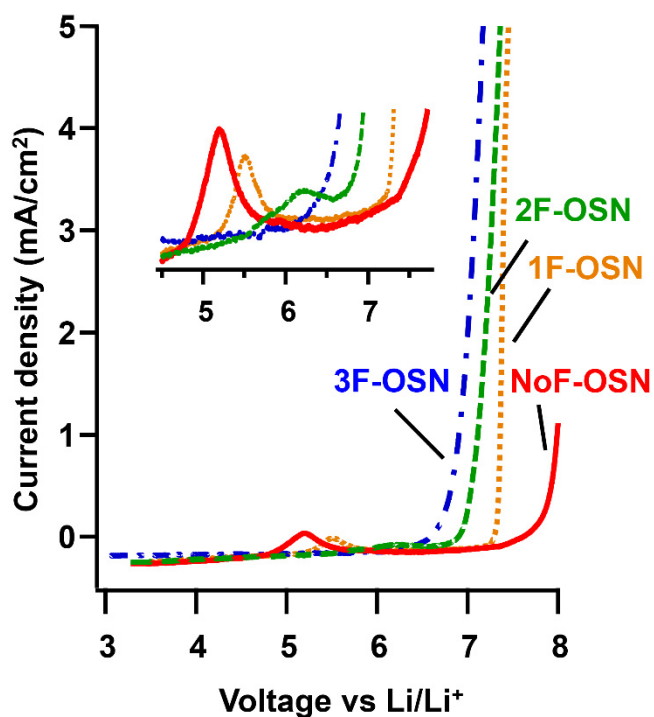


Figure 3.4 Linear sweep voltammograms from 3 to 8 V vs Li/Li⁺ of OSN series; NoF-OSN (red solid trace), 1F-OSN (orange small dash trace), 2F-OSN (green dash trace), and 3F-OSN (blue dot-dash trace). Inset shows expanded LSV region of pre-breakdown peaks. All electrolytes were formulated with 1M LiPF₆. LSVs were collected in a 3-electrode cell with Pt WE, Li RE, and Li CE at 10 mV/s.

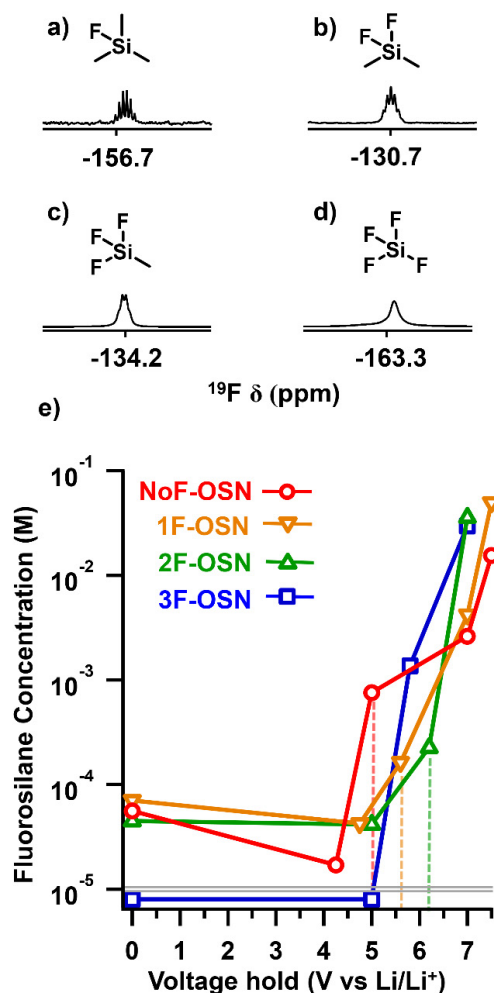


Figure 3.5 Expanded ^{19}F -NMR of the fluorosilane primary oxidation product for each OSN+1M LiPF_6 electrolyte after holding at 7 V vs Li/Li^+ for 24 hours: (a) NoF-OSN; (b) 1F-OSN; (c) 2F-OSN; and (d) 3F-OSN. (e) Concentration of fluorosilane in each solvent quantified from ^{19}F -NMR spectra after 24-hr hold at each voltage. NoF-OSN (red circles); 1F-OSN (orange inverted triangles); 2F-OSN (green triangles); 3F-OSN (blue squares). Dashed lines indicate the voltage of the pre-breakdown peak for each electrolyte that has this feature. Note y-axis is plotted on a logarithmic scale to emphasize changes in concentration. The double line at 10^{-5} M represents the approximate limit of detection for these spectra; points below the line are not observed in the spectra.

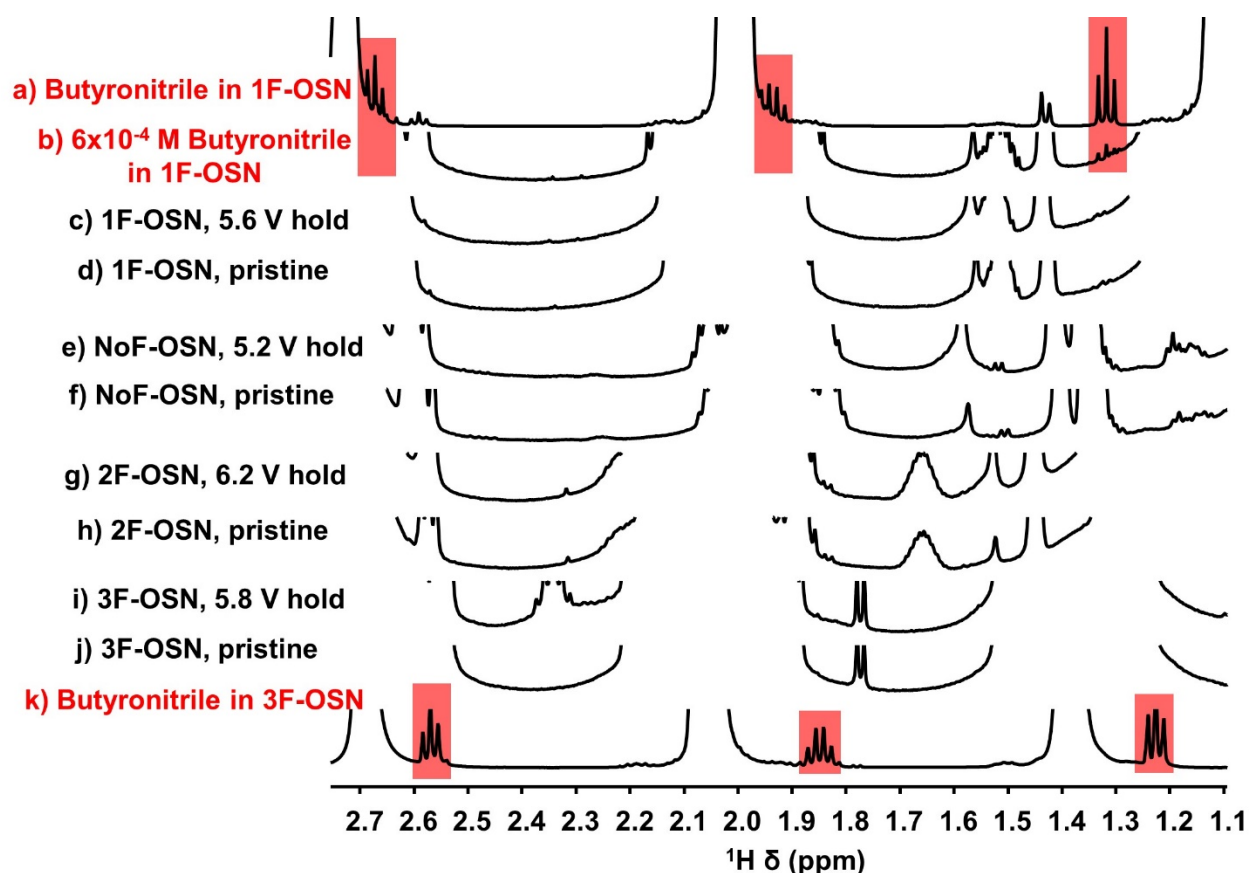
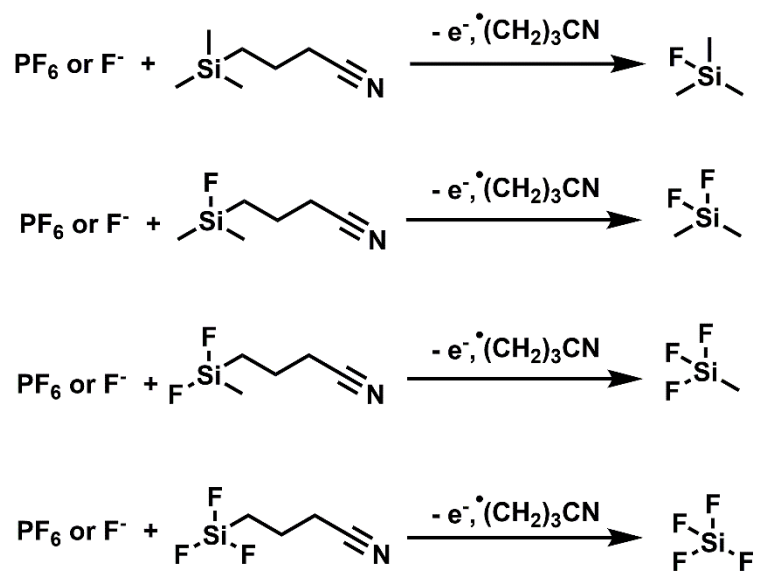


Figure 3.6. ^1H -NMR spectra showing comparisons of the peak regions of alkyl nitriles for a) commercial butyronitrile added to 1F-OSN to show expected peaks shape and chemical shift and b) 6×10^{-4} M commercial butyronitrile added to 1F-OSN at the same magnitude of concentration that $\text{SiF}_x\text{Me}_{4-x}$ species are observed in ^{19}F -NMR spectra. These standards are compared with the following OSN after and before a 24-hour voltage hold at the pre-breakdown peak voltage: c) 1F-OSN, 5.6V hold; d) 1F-OSN, pristine; e) NoF-OSN, 5.2V hold; f) NoF-OSN, pristine; g) 2F-OSN, 6.2V; h) 2F-OSN, pristine. Additionally, for comparison 3F-OSN (no prebreakdown peak) is shown after i) a 5.8V hold and j) pristine 3F-OSN, and k) commercial butyronitrile added to 3F-OSN to show the range of chemical shift in different OSN solvents. All samples contained 1 M LiPF_6 .

Scheme 3.1 Proposed primary mechanism of fluorosilane formation in each OSN electrolyte through coupled oxidation-fluorination



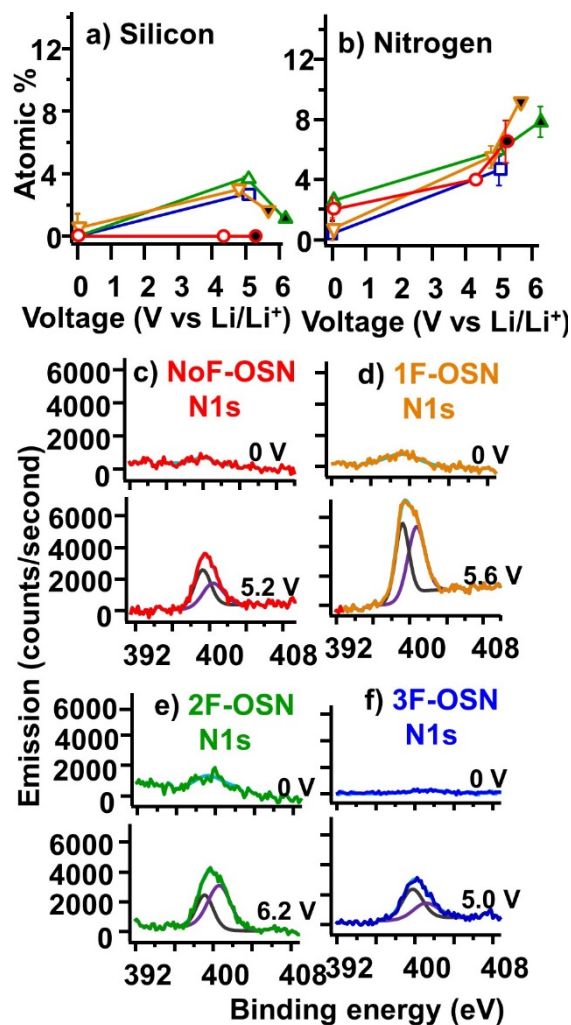


Figure 3.7. $^1\text{H-NMR}$ spectra showing comparisons of the peak regions of alkyl nitriles for a) commercial butyronitrile added to 1F-OSN to show expected peaks shape and chemical shift and b) 6×10^{-4} M commercial butyronitrile added to 1F-OSN at the same magnitude of concentration that $\text{SiF}_x\text{Me}_{4-x}$ species are observed in $^{19}\text{F-NMR}$ spectra. These standards are compared with the following OSN after and before a 24-hour voltage hold at the pre-breakdown peak voltage: c) 1F-OSN, 5.6V hold; d) 1F-OSN, pristine; e) NoF-OSN, 5.2V hold; f) NoF-OSN, pristine; g) 2F-OSN, 6.2V; h) 2F-OSN, pristine. Additionally, for comparison 3F-OSN (no prebreakdown peak) is shown after i) a 5.8V hold and j) pristine 3F-OSN, and k) commercial butyronitrile added to

3F-OSN to show the range of chemical shift in different OSN solvents. All samples contained 1 M LiPF₆.

Table 1. Calculated surface layer thickness (nm) on Pt positive electrodes from Pt4f signal attenuation after different voltage holds in OSN electrolytes.

Electrolyte	Control (0 V)	Potential lower than prebreakdown peak ^a	Prebreakdown peak potential ^b
NoF-OSN + 1M LiPF ₆	1.0	0.26	2.6
1F-OSN + 1M LiPF ₆	1.7	0.5	3.3
2F-OSN + 1M LiPF ₆	0.3	1.1	3.7
3F-OSN + 1M LiPF ₆	2.2	2.6	3.0

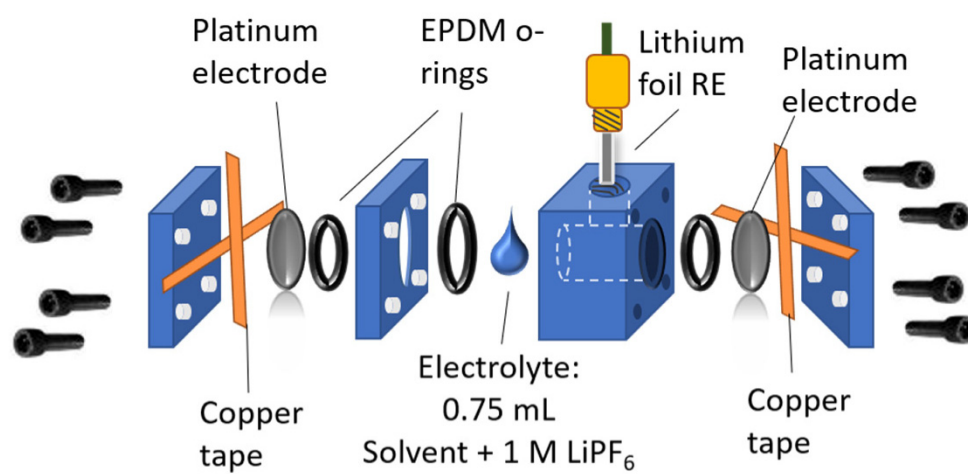


Figure S3.1 Schematic of the electrochemical cell used for voltage hold experiments

Table S3.1 Dielectric constants of OSN solvent molecules

Solvent molecule	Dielectric constant
NoF-OSN	12.57
1F-OSN	16.82
2F-OSN	18.2
3F-OSN	16.7

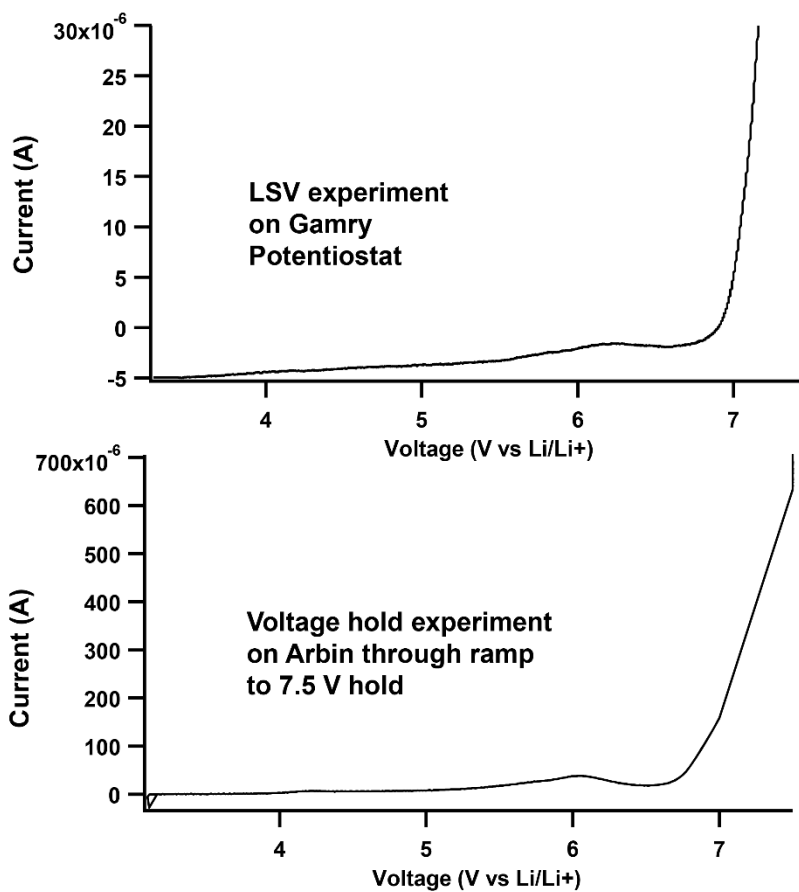


Figure S3.2 Validation of electrochemical cell for voltage hold experiments

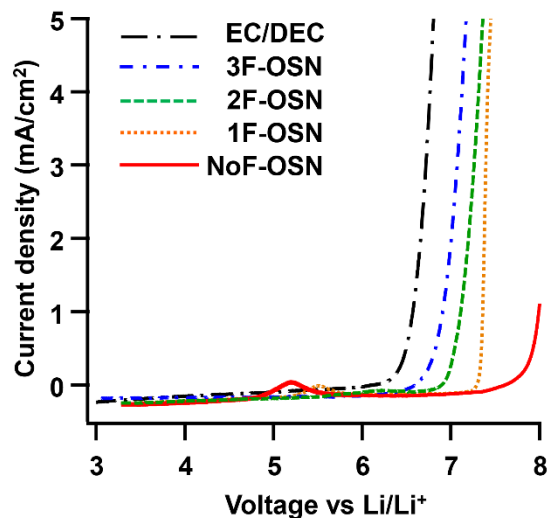


Figure S3.3 Linear sweep voltammograms of carbonate control EC/DEC3/7 v/v (black dot-long dash trace) compared with all OSN electrolytes: 3F-OSN (blue dot-dash trace), 2F-OSN (green dash trace), 1F-OSN (orange small dash trace), and NoF-OSN (solid red trace). All electrolytes were formulated with 1 M LiPF₆. LSVs were collected in a 3-electrode cell with Pt WE, Li RE, and Li CE at 10 mV/s.

Table S3.2 ^{19}F -NMR spectroscopic data for OSN solvent and primary oxidation species

Species	^{19}F ppm, mult (Hz)
$\text{SiF}_2(\text{CH}_3)_2$ (1F-OSN primary oxidation species)	-130.7, m ($J_{\text{H-F}}=6.3$)
SiF_3CH_3 (2F-OSN primary oxidation species)	-134.2, q ($J_{\text{H-F}}=4.2$)
3F-OSN	-135.5, m ($J_{\text{H-F}}= 6.0$)
$\text{SiF}(\text{CH}_3)_3$ (NoF-OSN primary oxidation species)	-156.7, m ($J_{\text{H-F}}=7.5$)
1F-OSN	-160.6, m ($J_{\text{H-F}}= 7.3$)
2F-OSN	-161.3, m ($J_{\text{H-F}}= 6.3$)
SiF_4 (3F-OSN primary oxidation species)	-163.3, s

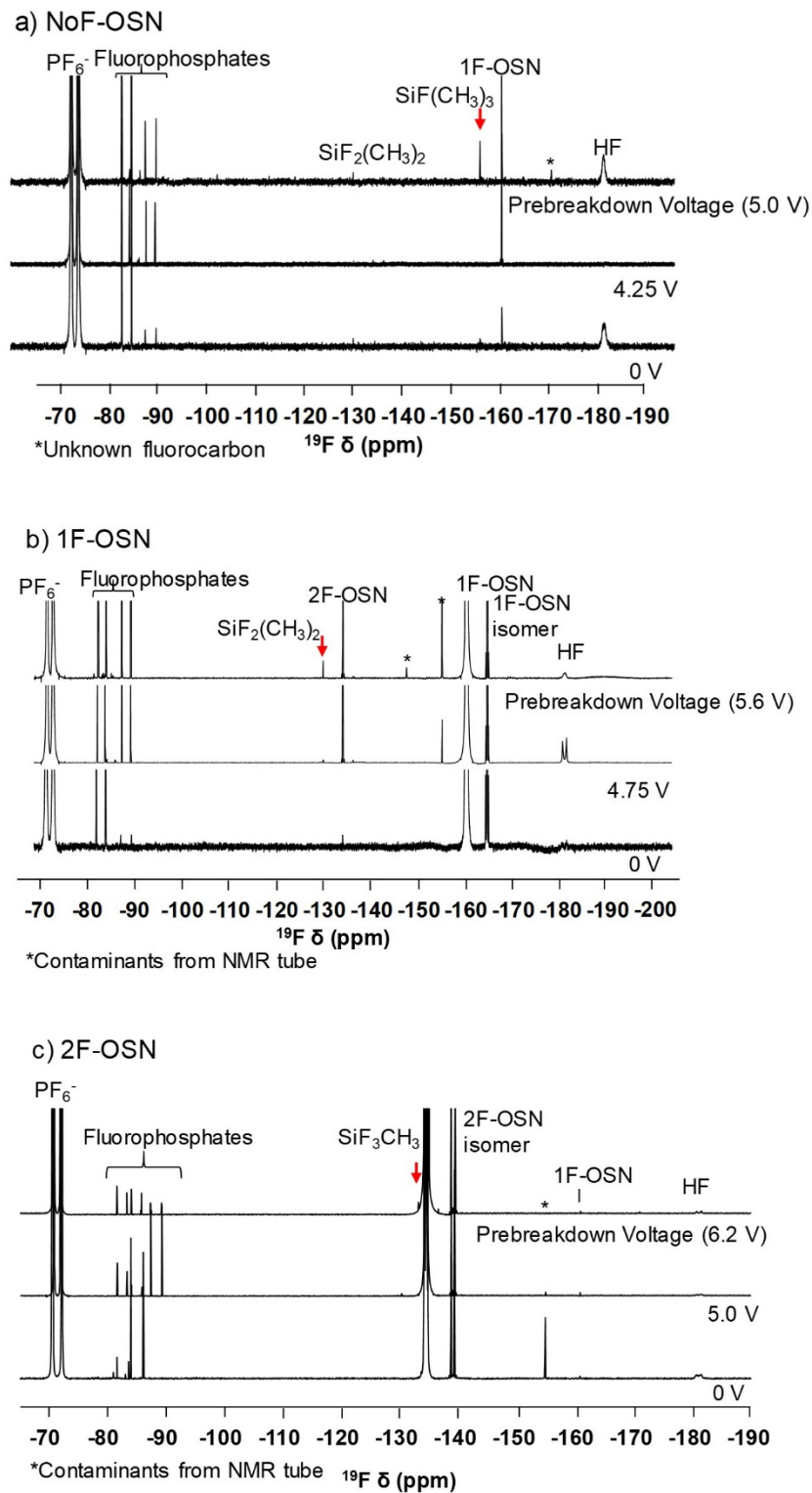


Figure S3.4. ¹⁹F-NMR of a) NoF-OSN, b) 1F-OSN, and c) 2F-OSN after different potential holds for 24 hours in the electrochemical cell shown in Figure S3.1: control sample with no voltage

applied (bottom spectra for all figures), voltage below prebreakdown potential (middle spectra for all figures), voltage at prebreakdown potential (top spectra for all figures). Red arrow indicates the primary oxidation species formed at the prebreakdown potential. All electrolytes have 1 M LiPF₆.

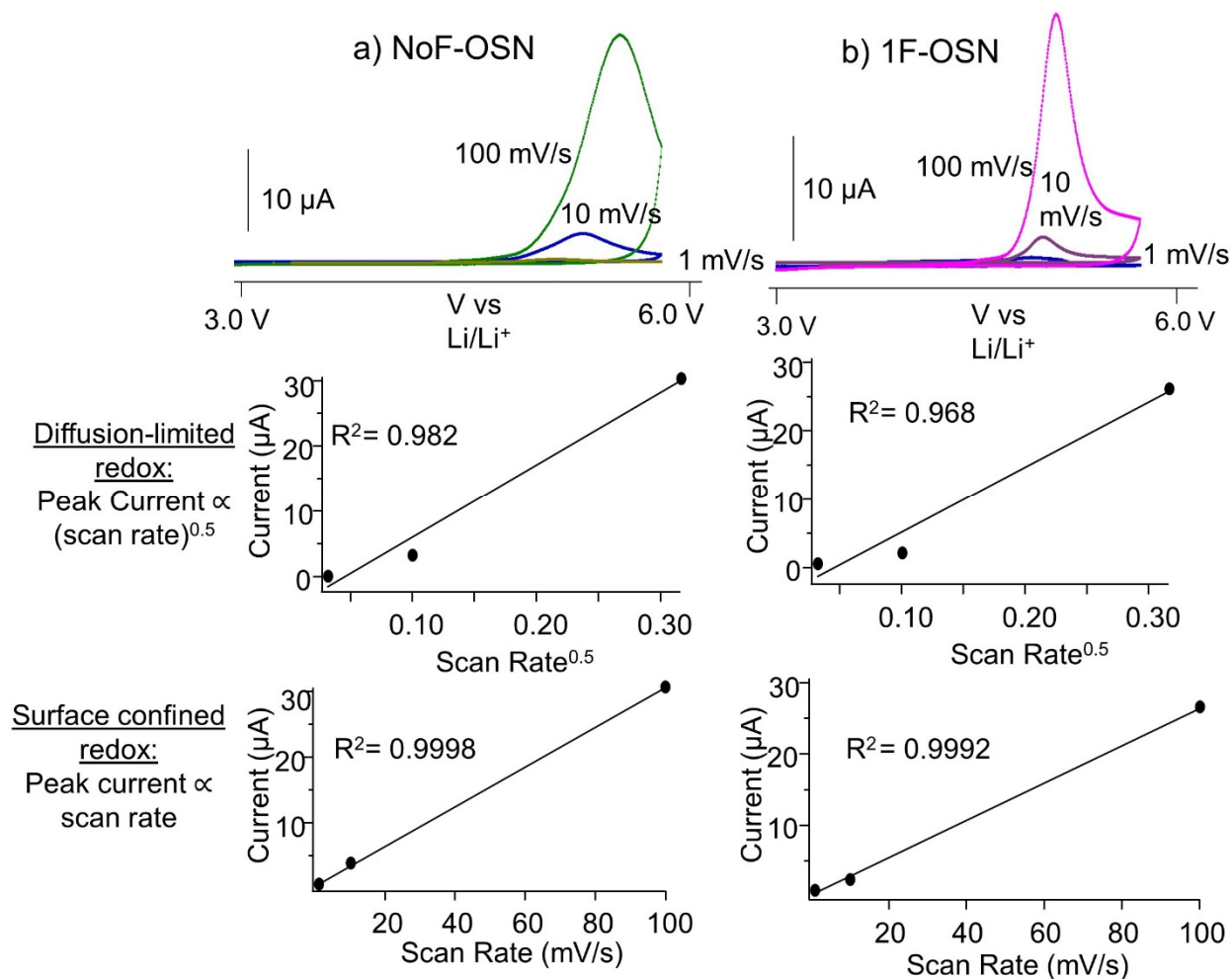


Figure S3.5. Cyclic voltammetry of the prebreakdown peaks for a) NoF-OSN + 1 M LiPF₆ and b) 1F-OSN + 1 M LiPF₆, at scan rates 100 mV/s, 10 mV/s, and 1 mV/s. The peak currents at each scan rate were plotted vs scan rate^{0.5} and vs scan rate to compare fits of the prebreakdown peaks to a diffusion limited or surface confined redox process respectively. CVs were collected in a 3-electrode cell with Pt WE, Li RE, and Li CE.

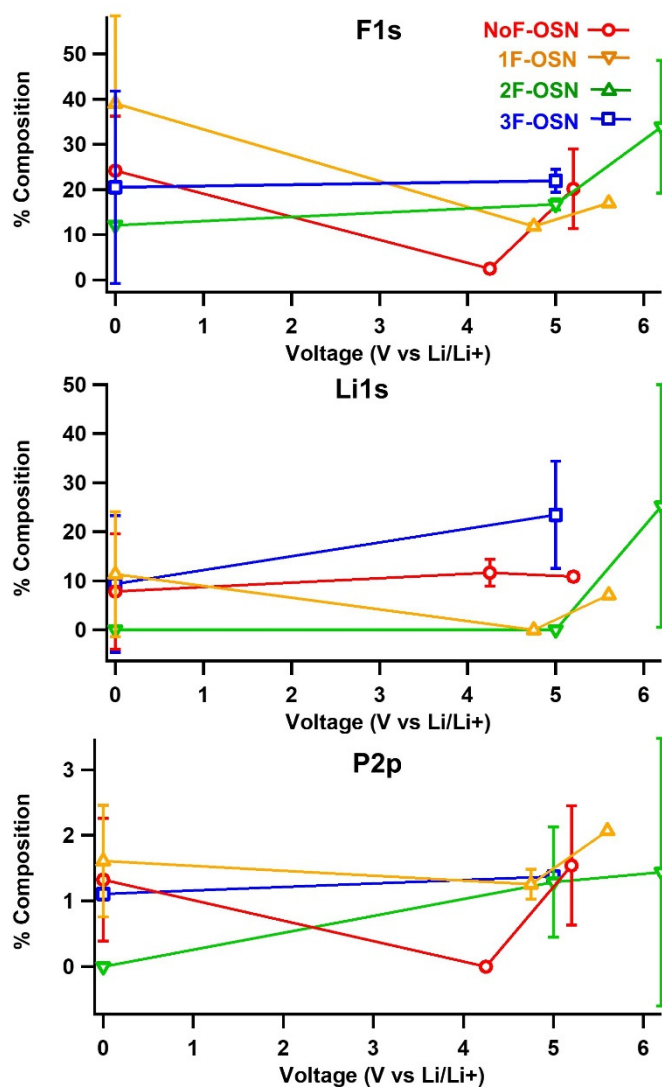


Figure S3.6. Percent composition of F1s, Li1s, and P2p from XPS on platinum positive electrodes after different voltage holds in OSN electrolytes (all with 1 M LiPF₆).

3.6 References

1. Xu, K., Electrolytes and Interphases in Li-Ion Batteries and Beyond. *Chemical Reviews* 2014, 114 (23), 11503-11618.
2. Goodenough, J. B.; Park, K.-S., The Li-Ion Rechargeable Battery: A Perspective. *Journal of the American Chemical Society* 2013, 135 (4), 1167-1176.
3. Shen, C.; Xiong, D.; Ellis, L. D.; Gering, K. L.; Huang, L.; Dahn, J. R., Using the Charge-Discharge Cycling of Positive Electrode Symmetric Cells to Find Electrolyte/Electrode Combinations with Minimum Reactivity. *Journal of The Electrochemical Society* 2017, 164 (13), A3349-A3356.
4. Tan, S.; Ji, Y. J.; Zhang, Z. R.; Yang, Y., Recent Progress in Research on High-Voltage Electrolytes for Lithium-Ion Batteries. *ChemPhysChem* 2014, 15 (10), 1956-1969.
5. Henderson, W. A., Nonaqueous Electrolytes: Advances in Lithium Salts. In *Electrolytes for Lithium Ion Batteries*, Jow, T. R.; Xu, K.; Borodin, O.; Ue, M., Eds. Springer: 2014; pp 1-92.
6. Smith, A. J.; Burns, J. C.; Zhao, X.; Xiong, D.; Dahn, J. R., A High Precision Coulometry Study of the SEI Growth in Li/Graphite Cells. *Journal of The Electrochemical Society* 2011, 158 (5), A447-A452.
7. Self, J.; Aiken, C. P.; Petibon, R.; Dahn, J. R., Survey of Gas Expansion in Li-Ion NMC Pouch Cells. *Journal of The Electrochemical Society* 2015, 162 (6), A796-A802.
8. Jung, R.; Metzger, M.; Maglia, F.; Stinner, C.; Gasteiger, H. A., Chemical versus Electrochemical Electrolyte Oxidation on NMC111, NMC622, NMC811, LNMO, and Conductive Carbon. *The Journal of Physical Chemistry Letters* 2017, 8 (19), 4820-4825.
9. Joho, F.; Novák, P., SNIFTIRS investigation of the oxidative decomposition of organic-carbonate-based electrolytes for lithium-ion cells. *Electrochimica Acta* 2000, 45 (21), 3589-3599.
10. Smith, A. J.; Burns, J. C.; Dahn, J. R., A High Precision Study of the Coulombic Efficiency of Li-Ion Batteries. *Electrochemical and Solid-State Letters* 2010, 13 (12), A177-A179.
11. Yu, Y.; Karayaylali, P.; Katayama, Y.; Giordano, L.; Gauthier, M.; Maglia, F.; Jung, R.; Lund, I.; Shao-Horn, Y., Coupled LiPF₆ Decomposition and Carbonate Dehydrogenation Enhanced by Highly Covalent Metal Oxides in High-Energy Li-Ion Batteries. *The Journal of Physical Chemistry C* 2018, 122 (48), 27368-27382.
12. Giordano, L.; Karayaylali, P.; Yu, Y.; Katayama, Y.; Maglia, F.; Lux, S.; Shao-Horn, Y., Chemical Reactivity Descriptor for the Oxide-Electrolyte Interface in Li-Ion Batteries. *The Journal of Physical Chemistry Letters* 2017, 8 (16), 3881-3887.

13. Wang, L.; Liu, S.; Zhao, K.; Li, J.; Yang, Y.; Jia, G., Improving the rate performance and stability of $\text{LiNi}_0.6\text{Co}_0.2\text{Mn}_0.2\text{O}_2$ in high voltage lithium-ion battery by using fluoroethylene carbonate as electrolyte additive. *Ionics* 2018, 24 (11), 3337-3346.
14. Xu, X.; Deng, S.; Wang, H.; Liu, J.; Yan, H., Research Progress in Improving the Cycling Stability of High-Voltage $\text{LiNi}_0.5\text{Mn}_1.5\text{O}_4$ Cathode in Lithium-Ion Battery. *Nano-Micro Letters* 2017, 9 (2), 22.
15. Chen, X.; Usrey, M.; Peña-Hueso, A.; West, R.; Hamers, R. J., Thermal and electrochemical stability of organosilicon electrolytes for lithium-ion batteries. *Journal of Power Sources* 2013, 241, 311-319.
16. Zhang, L.; Lyons, L.; Newhouse, J.; Zhang, Z.; Straughan, M.; Chen, Z.; Amine, K.; Hamers, R. J.; West, R., Synthesis and characterization of alkylsilane ethers with oligo(ethylene oxide) substituents for safe electrolytes in lithium-ion batteries. *J. Mater. Chem.* 2010, 20 (38), 8224-8226.
17. Zhang, L.; Zhang, Z.; Harring, S.; Straughan, M.; Butorac, R.; Chen, Z.; Lyons, L.; Amine, K.; West, R., Highly conductive trimethylsilyl oligo(ethylene oxide) electrolytes for energy storage applications. *J. Mater. Chem.* 2008, 18 (31), 3713-3717.
18. Lyons, L. J.; Pena-Hueso, A.; Johnson, T.; West, R., Silyl and silyl/carbonate blend electrolytes for lithium-ion battery applications. *ECS Trans.* 2016, 73 (1, 18th International Meeting on Lithium Batteries (IMLB 2016)), 281-288.
19. Guillot, S. L.; Peña-Hueso, A.; Usrey, M. L.; Hamers, R. J., Thermal and Hydrolytic Decomposition Mechanisms of Organosilicon Electrolytes with Enhanced Thermal Stability for Lithium-Ion Batteries. *Journal of The Electrochemical Society* 2017, 164 (9), A1907-A1917.
20. Zhang, Z.; Hu, L.; Wu, H.; Weng, W.; Koh, M.; Redfern, P. C.; Curtiss, L. A.; Amine, K., Fluorinated electrolytes for 5 V lithium-ion battery chemistry. *Energy & Environmental Science* 2013, 6 (6), 1806-1810.
21. Sasaki, Y.; Satake, H.; Tsukimori, N.; Nanbu, N.; Takehara, M.; Ue, M., Physical and Electrolytic Properties of Partially Fluorinated Methyl Propyl Carbonate and Its Application to Lithium Batteries. *Electrochemistry* 2010, 78 (5), 467-470.
22. Su, C.-C.; He, M.; Redfern, P. C.; Curtiss, L. A.; Shkrob, I. A.; Zhang, Z., Oxidatively stable fluorinated sulfone electrolytes for high voltage high energy lithium-ion batteries. *Energy & Environmental Science* 2017, 10 (4), 900-904.
23. M. J. Frisch, G. W. T., H. B. Schlegel, G. E. Scuseria, M. A. Robb, J. R. Cheeseman, G. Scalmani, V. Barone, G. A. Petersson, H. Nakatsuji, X. Li, M. Caricato, A. Marenich, J. Bloino, B. G. Janesko, R. Gomperts, B. Mennucci, H. P. Hratchian, J. V. Ortiz, A. F. Izmaylov, J. L. Sonnenberg, D. Williams-Young, F. Ding, F. Lipparini, F. Egidi, J. Goings, B. Peng, A. Petrone, T. Henderson, D. Ranasinghe, V. G. Zakrzewski, J. Gao, N. Rega, G. Zheng, W. Liang, M. Hada, M. Ehara, K. Toyota, R. Fukuda, J. Hasegawa, M. Ishida, T. Nakajima, Y. Honda, O. Kitao, H. Nakai, T. Vreven, K. Throssell, J. A. Montgomery, Jr., J. E. Peralta, F. Ogliaro, M.

Bearpark, J. J. Heyd, E. Brothers, K. N. Kudin, V. N. Staroverov, T. Keith, R. Kobayashi, J. Normand, K. Raghavachari, A. Rendell, J. C. Burant, S. S. Iyengar, J. Tomasi, M. Cossi, J. M. Millam, M. Klene, C. Adamo, R. Cammi, J. W. Ochterski, R. L. Martin, K. Morokuma, O. Farkas, J. B. Foresman, and D. J. Fox, Gaussian 09, Revision A.02. Gaussian, Inc., Wallingford CT, 2016.

24. Borodin, O.; Ren, X.; Vatamanu, J.; von Wald Cresce, A.; Knap, J.; Xu, K., Modeling Insight into Battery Electrolyte Electrochemical Stability and Interfacial Structure. *Accounts of Chemical Research* 2017, 50 (12), 2886-2894.
25. Borodin, O.; Behl, W.; Jow, T. R., Oxidative Stability and Initial Decomposition Reactions of Carbonate, Sulfone, and Alkyl Phosphate-Based Electrolytes. *The Journal of Physical Chemistry C* 2013, 117 (17), 8661-8682.
26. Trasatti, S., The absolute electrode potential: an explanatory note (Recommendations 1986). *Journal of Electroanalytical Chemistry and Interfacial Electrochemistry* 1986, 209 (2), 417-428.
27. Harris, R. K.; Becker, E. D.; Menezes, S. M. C. D.; Granger, P.; Hoffman, R. E.; Zilm, K. W., Further Conventions for NMR Shielding and Chemical Shifts (IUPAC Recommendations 2008). *Magnetic Resonance in Chemistry* 2008, 46 (6), 582-598.
28. Borodin, O.; Olguin, M.; Spear, C. E.; Leiter, K. W.; Knap, J., Towards high throughput screening of electrochemical stability of battery electrolytes. *Nanotechnology* 2015, 26 (35), 354003.
29. Delp, S. A.; Borodin, O.; Olguin, M.; Eisner, C. G.; Allen, J. L.; Jow, T. R., Importance of Reduction and Oxidation Stability of High Voltage Electrolytes and Additives. *Electrochimica Acta* 2016, 209, 498-510.
30. Xing, L.; Borodin, O., Oxidation induced decomposition of ethylene carbonate from DFT calculations – importance of explicitly treating surrounding solvent. *Physical Chemistry Chemical Physics* 2012, 14 (37), 12838-12843.
31. Xing, L.; Borodin, O.; Smith, G. D.; Li, W., Density Functional Theory Study of the Role of Anions on the Oxidative Decomposition Reaction of Propylene Carbonate. *The Journal of Physical Chemistry A* 2011, 115 (47), 13896-13905.
32. Yan, G.; Li, X.; Wang, Z.; Guo, H.; Peng, W.; Hu, Q.; Wang, J., Fluorinated solvents for high-voltage electrolyte in lithium-ion battery. *Journal of Solid State Electrochemistry* 2017, 21 (6), 1589-1597.
33. Koch, V. R.; Dominey, L. A.; Nanjundiah, C.; Ondrechen, M. J., The Intrinsic Anodic Stability of Several Anions Comprising Solvent-Free Ionic Liquids. *Journal of The Electrochemical Society* 1996, 143 (3), 798-803.

34. Zhang, Y.; Shi, C.; Brennecke, J. F.; Maginn, E. J., Refined Method for Predicting Electrochemical Windows of Ionic Liquids and Experimental Validation Studies. *The Journal of Physical Chemistry B* 2014, 118 (23), 6250-6255.
35. Frankiss, S. G., Fluorine magnetic resonance spectra of methylfluorosilanes. *J. Phys. Chem.* 1967, 71 (11), 3418-21.
36. Suvorov, B., Intramolecular electronic interaction in a series of organosilicon compounds. *Russian Journal of General Chemistry* 2006, 76 (9), 1401-1406.
37. Alyev, I. Y.; Rozhkov, I. N.; Knunyants, I. L., Anode chemistry of organosilanes. Oxidative replacement of alkyl group by fluoride ion. *Tetrahedron Letters* 1976, 17 (28), 2469-2470.
38. Bard, A. J.; Faulkner, L. R., *Electrochemical Methods: Fundamentals and Applications*. 2nd ed.; John Wiley & Sons: New York, 2001.
39. Jansen, R. J. J.; van Bekkum, H., XPS of nitrogen-containing functional groups on activated carbon. *Carbon* 1995, 33 (8), 1021-7.
40. Pels, J. R.; Kapteijn, F.; Moulijn, J. A.; Zhu, Q.; Thomas, K. M., Evolution of nitrogen functionalities in carbonaceous materials during pyrolysis. *Carbon* 1995, 33 (11), 1641-53.
41. Schwartz, M. P.; Barlow, D. E.; Russell, J. N., Jr.; Butler, J. E.; D'Evelyn, M. P.; Hamers, R. J., Adsorption of Acrylonitrile on Diamond and Silicon (001)-(2 μ 1) Surfaces: Effects of Dimer Structure on Reaction Pathways and Product Distributions. *J. Am. Chem. Soc.* 2005, 127 (23), 8348-8354.
42. Sexton, B. A.; Avery, N. R., Coordination of acetonitrile (CH₃CN) to platinum(111): evidence for an η^2 (C,N) species. *Surf. Sci.* 1983, 129 (1), 21-36.
43. Seah, M. P., Simple universal curve for the energy-dependent electron attenuation length for all materials. *Surface and Interface Analysis* 2012, 44 (10), 1353-1359.
44. Duncan, H.; Salem, N.; Abu-Lebdeh, Y., Electrolyte Formulations Based on Dinitrile Solvents for High Voltage Li-Ion Batteries. *Journal of The Electrochemical Society* 2013, 160 (6), A838-A848.
45. Liao, B.; Hu, X.; Xu, M.; Li, H.; Yu, L.; Fan, W.; Xing, L.; Liao, Y.; Li, W., Constructing Unique Cathode Interface by Manipulating Functional Groups of Electrolyte Additive for Graphite/LiNi_{0.6}Co_{0.2}Mn_{0.2}O₂ Cells at High Voltage. *The Journal of Physical Chemistry Letters* 2018, 9 (12), 3434-3445.
46. Di Censo, D.; Exnar, I.; Graetzel, M., Non-corrosive electrolyte compositions containing perfluoroalkylsulfonyl imides for high power Li-ion batteries. *Electrochemistry Communications* 2005, 7 (10), 1000-1006.

47. Wang, X.; Xue, W.; Hu, K.; Li, Y.; Li, Y.; Huang, R., Adiponitrile as Lithium-Ion Battery Electrolyte Additive: A Positive and Peculiar Effect on High-Voltage Systems. *ACS Applied Energy Materials* 2018, 1 (10), 5347-5354.
48. Zhi, H.; Xing, L.; Zheng, X.; Xu, K.; Li, W., Understanding How Nitriles Stabilize Electrolyte/Electrode Interface at High Voltage. *The Journal of Physical Chemistry Letters* 2017, 8 (24), 6048-6052.
49. Kim, Y.-S.; Kim, T.-H.; Lee, H.; Song, H.-K., Electronegativity-induced enhancement of thermal stability by succinonitrile as an additive for Li ion batteries. *Energy & Environmental Science* 2011, 4 (10), 4038-4045.

Chapter 4. Competitive Solvation in Mixed Organosilicon and Carbonate Electrolytes

4.1 Introduction

Lithium ion batteries are ubiquitous form of energy storage in today's mobile electronics and electric vehicles. Enhancing lithium ion battery voltage, capacity, lifetime and safety is necessary to meet growing energy needs. The battery electrolyte plays a significant role in these properties. In batteries above 4 V, the electrodes are poised at potentials such the electrolyte at the solid/liquid interface is not thermodynamically stable, leading to the formation of passivating solid-electrolyte interphase (SEI) layers that dominate battery cell impedance and capacity loss.¹ The composition of the SEI layer is dependent on the nature of the interfacial species, which relies on the molecules composing the lithium ion solvation shell. The dominance of one solvent in the solvation shell of a mixed electrolyte has been shown to dictate the speciation of the SEI and solvent cointercalation.² Additionally, bulk properties of solvents can dictate important electrolyte characteristics such as viscosity, conductivity, and thermal stability.³

Conventional battery electrolytes utilize lithium hexafluorophosphate (LiPF₆) as the salt, due to its high dissociation in nonaqueous polar solvents combined with its stability in contact with aluminum current collectors. A combination of linear and cyclic carbonates are typically used for electrolyte solvents to achieve a balance of low viscosity and high conductivity.⁴ Additionally, a number of additive species may be added to enhance battery performance in different ways, including cathode or anode film-formers, flame retardants, and overcharge preventatives.⁵

Organosilicon solvents have previously shown promise as lithium-ion battery electrolytes, with good conductivity,⁶ high thermal and hydrolytic stability,⁷⁻⁸ and excellent oxidative stability.⁹ It is therefore of interest to understand the nature of lithium solvation in organosilicon-based electrolytes, and in mixed organosilicon-carbonate electrolytes. In this study, we probe the

solvation structure of fluorinated-organosilicon-nitrile-based lithium-ion electrolytes (1F-OSN) mixed with ethylene carbonate (EC) and diethyl carbonate (DEC) using density functional theory (DFT) calculations, Fourier Transform infrared spectroscopy (FTIR), and nuclear magnetic resonance spectroscopy (NMR). In DEC/1F-OSN electrolytes we show through NMR and FTIR that lithium solvation is shared by both solvents, and that the degree of salt dissociation increases with added 1F-OSN. By contrast, in EC/1F-OSN mixed electrolytes, EC dominates more strongly over 1F-OSN within the solvation shell; however, organosilicons are still involved in the lithium solvation shell even at very low concentrations (<10 mol%). These studies unveil the challenges of analyzing even simple electrolyte solutions and provide a foundation of techniques and solvation structure that can be used in understanding electrolyte systems of greater complexity and application.

4.2 Materials and Methods

4.2.1 Chemicals

All chemicals were anhydrous or dried and stored in an argon-atmosphere glovebox immediately upon receipt. The organosilicon compounds were received from Silatronix, Inc. Lithium hexafluorophosphate was purchased from BASF and Sigma Aldrich. Ethylene carbonate and diethyl carbonate were purchased from SoulBrain and from Sigma Aldrich. Anhydrous dimethyl carbonate was purchased from Sigma-Aldrich.

4.2.2 Fourier Transform Infrared Spectroscopy (FTIR).

FTIR samples were measured in a Screw-Type Demountable cell Mount liquid transmission cell (New Era) with 2 calcium fluoride windows (25.4 m diameter, 3 mm thick, ISP Optics). One optical window had a spacer ring of 800 nm silicon dioxide deposited through dielectric evaporation. To achieve this spacer, the center of the optical window was covered with a round glass slide adhered to the sample surface with photoresist during dielectric evaporation of

silicon dioxide. After the SiO₂ deposition, the cover slip and photoresist were removed by soaking in ethyl acetate. Samples were prepared by pipetting 1 uL of sample between the optical windows. Samples were prepared in an argon atmosphere glovebox. Transmission FTIR spectra were acquired with a Bruker Vertex 70 FTIR instrument at 2 cm⁻¹ resolution and averaging 500 scans per spectrum. A spectrum of the blank cell was used as the background when calculating absorbance. FTIR peaks were deconvoluted using FitYK software.¹⁰ Each part of the liquid transmission cell was cleaned by rinsing in 2 mL dimethyl carbonate and dried under vacuum for 30 minutes.

4.2.3 Nuclear Magnetic Resonance (NMR) Spectroscopy.

NMR samples were prepared in an Ar glovebox in polytetrafluoroethylene/fluorinated ethylene polypropylene copolymer (PTFE-FEP) 5 mm tube liners (Wilmad Glass), which were placed into 7" 5 mm NMR tubes and sealed with Superior High Pressure Caps (Wilmad Glass). Samples were analyzed with a Bruker Avance III 500 MHz spectrometer with a BBFO PLUS probe. All spectra were referenced using a substitution reference standard of 1% TMS in CDCl₃ and processed with MestreNova 9.1.0. The calibration was applied during processing by absolute referencing.¹¹ DOSY (diffusion) measurements were made at 298 K with the Jerschow-Müller convection-compensated pulse sequence.¹² Diffusion coefficients were measured by fitting the appropriate NMR signal peak area (⁷Li or ¹⁹F for Li⁺ and PF₆⁻ respectively) as a function of the log magnetic gradient according to the equation:¹³

$$\ln A = -\gamma^2 \delta^2 G_z^2 D \left(\Delta + \frac{4\delta}{3} + \frac{3\tau}{2} \right) \quad (4.1)$$

Where A is the peak area, γ is the gyromagnetic ratio of the nuclei under observation in radians² s⁻² G⁻², δ is the bipolar gradient pulse width in s, G_z is the gradient strength in G cm⁻¹, D is the

diffusion coefficient in $\text{cm}^2 \text{s}^{-1}$, Δ is the pulse delay in s, and τ is the gradient ringdown delay in s. A list of the delays used for each sample is shown in Table S4.1.

4.2.4 DFT calculation methods.

All calculations were performed with Gaussian 09 software¹⁴ on the UW-Madison Chemistry Department High-Performance Computing cluster. The structures were optimized with B3LYP with a 6-31+G* basis set. The optimized structures had zero negative eigenvalues by frequency analyses. Zero-point vibrational energy corrections were taken into account when calculating solvation binding energies. Implicit solvation was modeled with a Polarizable Continuum Model (PCM) using acetone as the model solvent (dielectric constant = 20).

4.3 Results and discussion

4.3.1 Computation

To aid in understanding lithium-ion electrolyte solvation structure, there has been extensive research on computation of solvation energy for various single solvent and mixed carbonates.¹⁵⁻²⁰ We ran DFT calculations on lithium solvated by DEC, EC and 1FOSN. Solvation binding energies were calculated from the equation

$$E_B = E_{LiX} - (E_{Li} + E_X) \quad (4.2)$$

Where E_B is the binding energy, E_{LiX} is the energy of the lithium-solvent cluster, E_{Li} is the energy of the lithium ion, and E_X is sum of the energies of the individual solvent molecules that make up the lithium-solvent cluster. The results of these calculations are shown in Table 4.1. Considering the case of a lithium coordinated by a single solvent molecule in the gas phase, the preference for lithium solvation is shown to be $EC > 1F\text{-OSN} > DEC$. When the same solvent cluster is calculated in a simulated Polarizable Continuum Model solvent with the dielectric constant of acetone ($\epsilon =$

20), the trend is consistent with the gas-phase results. The calculations performed with a PCM represent modeling of the impact of the solvent environment beyond the first solvation shell.

Reports on the solvation number of lithium vary from 3-6,^{16, 21-23} but typically 4 solvent molecules is cited as the preferred number.^{19, 23} Additionally, computation has shown that mixed solvent clusters can show varying degrees of stability that cannot simply be determined as the sum of the binding energies of the individual solvents.¹⁵ Therefore, we also performed calculations of the solvation binding energies for clusters with on four solvent molecules around lithium, $\text{Li}(\text{1F-OSN})_{4-n}(\text{X})_n$ where X is EC or DEC and $n=0-4$ (Table 4.1). The binding energies of solvent clusters in the gas phase with four of the same solvent follow the same trend as the single-solvent-lithium clusters, with the greatest binding energy for $\text{Li}^+(\text{EC})_4$ (-123.5 kcal/mol), followed by $\text{Li}^+(\text{1F-OSN})_4$ (-117.7 kcal/mol), and $\text{Li}^+(\text{DEC})_4$ with the smallest binding energy (-113.1 kcal/mol). These results are consistent with computational and experimental results showing that EC is a strong solvating molecule.²⁰ For mixed solvent clusters, $\text{Li}^+(\text{EC})_{4-n}(\text{1F-OSN})_n$ ($n=1-3$) complexes all have very similar binding energies to pure $\text{Li}^+(\text{EC})_4$, with $\text{Li}^+(\text{EC})_3(\text{1F-OSN})$ having a slightly greater binding energy (-123.8 kcal/mol). When the solvation cluster contains both DEC and 1F-OSN, $\text{Li}(\text{DEC})_2(\text{1F-OSN})_2$ has the largest binding energy, greater than pure $\text{Li}^+(\text{1F-OSN})$. The binding energy of $\text{Li}(\text{DEC})_3(\text{1F-OSN})$ is intermediate between pure DEC and pure 1F-OSN, while $\text{Li}(\text{DEC})(\text{1F-OSN})_3$ has a smaller binding energy of -112.1 kcal/mol.

These results suggest that without considering any effects of the solvent environment beyond the first solvation shell, for mixed EC/1F-OSN electrolytes the most favorable interactions with lithium occur with a solvation cluster composed of three EC molecules and one 1F-OSN molecule, although all clusters that contain at least one EC molecule are close in energies. For

mixed DEC/1F-OSN electrolytes the most favorable solvation shell contains two DEC molecules and two 1F-OSN molecules.

Several 4-solvent-molecule lithium clusters in an acetone implicit solvent did not converge to an optimized geometry with no negative eigenvalues, so this series for comparison is not complete. However, we will discuss all those complexes that did converge with zero negative frequencies. Comparing the mixed $\text{Li}^+(\text{EC})_{4-n}(\text{1F-OSN})_n$ ($n=1-3$) solvation clusters, all have similar binding energies (-15.5 to -15.8 kcal/mol) and there is an increase in the solvation binding energy relative to $\text{Li}^+(\text{1F-OSN})_4$ (-13.8 kcal/mol), similar to the gas-phase calculations. Also in concurrence with gas-phase calculations, $\text{Li}^+(\text{DEC})_2(\text{1F-OSN})_2$ has a larger binding energy than $\text{Li}^+(\text{1F-OSN})_4$, and $\text{Li}^+(\text{DEC})(\text{1F-OSN})_3$ has the smallest binding energy. One notable difference between the gas phase and PCM calculations trends is the smaller binding energy for all $\text{Li}^+(\text{EC})_{4-n}(\text{1F-OSN})_n$ ($n=1-3$) clusters compared to $\text{Li}^+(\text{DEC})_2(\text{1F-OSN})_2$. These results may reflect the influence of a moderately high dielectric constant implicit solvent on stabilizing individual solvent molecules of high to moderate polarity (EC, $\epsilon = 90$ and 1F-OSN, $\epsilon = 16$), while in the tetrahedral solvation structure the individual solvent molecules' dipole vectors may be partially cancelled.¹⁶ Therefore, it may be more relevant to compare solvation binding energies within a binary solvent series and not between series.

These results suggest that when including the effect of a moderately polar solvent environment beyond the first solvation shell ($\epsilon = 20$), for mixed EC/1F-OSN electrolytes the most favorable interactions with lithium occur with a solvation cluster composed of either three EC molecules and one 1F-OSN molecule or two EC and two 1F-OSN molecules, although all clusters that contain at least one EC molecule are close in energies. For mixed DEC/1F-OSN electrolytes the most favorable solvation shell contains two DEC molecules and two 1F-OSN molecules.

Overall, the DFT data we have collected suggest that a primary lithium solvation shell with equal amounts of DEC and 1F-OSN may be the most stable for DEC/1F-OSN mixed electrolytes, while all solvation shells containing at least one EC molecule may be approximately equally favorable for EC/1F-OSN mixed electrolytes. Importantly, the solvation binding energies for the four solvent molecules surrounding a lithium do not represent a linear combination of the of a single solvent molecule coordinating to lithium, reflecting the effects of individual dipole canceling and steric/electronic repulsive effects^{1, 15-16, 24} and indicating that in mixed solvents it will be unlikely that all solvation shells will contain only the one type of solvent that shows the most favorable single-solvent interaction by DFT (e.g. EC in mixed EC/1F-OSN, EC; 1F-OSN in mixed DEC/1F-OSN). These calculations represent an initial effort to understand the electronic, thermal, and steric factors involved in lithium stability in different solvation clusters. In order to fully assess the robustness and accuracy of these computational results, additional calculations will be performed with different methods, basis sets, and implicit solvation models.

4.3.2 ⁶Li- NMR assessment of the solvation sphere

The chemical shift of a specific nuclide is dependent on its surrounding chemical environment.²⁵ When separate chemical species or conformers are present in dynamic equilibrium faster than the timescale of the NMR measurement, the chemical shift appears as a weighted average of the individual components according to the equation:²⁶

$$\delta_{\text{obs}} = n_1/(n_1+n_2)*\delta_1 + n_2/(n_1+n_2)*\delta_2 \quad (4.3)$$

Where δ_{obs} is the observed chemical shift, δ_1 is the chemical shift of pure species 1, δ_2 is the chemical shift of pure species 2, and n_1 and n_2 are the quantities of species 1 and species 2 respectively in the sample under study.

In this manner, NMR observation of the lithium ion can provide insight into the surrounding solvation structure. In this study, we measured the ${}^6\text{Li}$ -NMR signal of 1M LiPF_6 in two series of mixed solvents with 1) DEC/1F-OSN and 2) EC/1F-OSN mole ratios ranging from 10/1 to 1/5, as well as 1M LiPF_6 in the individual EC, DEC, and 1F-OSN solvents. From these NMR spectra the relative concentrations of carbonate-Li and 1F-OSN-Li contributions to the ${}^6\text{Li}$ chemical shift in ppm were calculated as a function of 1F-OSN mole fraction as shown in Equation 3:

$$\text{1F-OSN-Li fraction of } {}^6\text{Li signal} = (\delta_{\text{obs}} - \delta_{\text{1F-OSN}}) / (\delta_{\text{carbonate}} - \delta_{\text{1F-OSN}}) \quad (4.4)$$

Where δ_{obs} is the chemical shift of the mixed solvent system under observation, $\delta_{\text{1F-OSN}}$ is the chemical shift of 1M LiPF_6 in pure 1F-OSN (-2.2 ppm), and $\delta_{\text{carbonate}}$ is the chemical shift of 1M LiPF_6 in EC (-0.6 ppm) or DEC (-0.4 ppm), depending on the carbonate of the mixed solvent system.

Figure S4.1 shows the superimposed ${}^6\text{Li}$ -NMR spectra for each sample the two data series under analysis. Figure 4.1 shows the calculated fractional 1F-OSN contribution to the ${}^6\text{Li}$ peak chemical shift for each mixed solvent composition when paired with EC (Fig. 4.1a) and with DEC (Fig 4.1b). The values for these graphs are shown in Table S4.2. The grey dashed line in these graphs represents the expected result if the fraction of 1F-OSN contributing to the solvation shell were equivalent to its fraction of composition. Points above this line correspond to a 1F-OSN fractional contribution to the ${}^6\text{Li}$ chemical shift greater than its fractional composition in solution, while points below this line correspond to a 1F-OSN contribution to the ${}^6\text{Li}$ shift that less is than its fractional composition. For both EC/1F-OSN and DEC/1F-OSN, 1F-OSN contributes less than its composition in solution for all electrolyte mixtures studied. For example, when EC and OS3 are present in a 1:1 mol ratio (1F-OSN fraction of composition = 0.5), the result of Equation 4.4

indicates that 63% of the lithium chemical shift comes from EC coordination and 37% from 1F-OSN coordination. When DEC and OS3 are present in a 1:1 mol ratio (1F-OSN fraction of composition = 0.5), the result of Equation 4.4 indicates that 57% of the lithium chemical shift comes from DEC coordination and 43% from 1F-OSN coordination. These ^6Li -NMR results suggest that each carbonate has a majority share of the solvation sphere in mixed carbonate/1F-OSN electrolytes. The solvation dominance by DEC is minor and solvation is shared by both DEC and 1F-OSN, while EC dominates to a greater degree over 1F-OSN in the solvation sphere.

4.3.3 Calculation of Ionic Dissociation

Equation 4.4 is valid only when the change in the chemical shift of lithium is determined solely by the variation in the average coordination sphere between two solvents, and there is no other factor influencing the ^6Li chemical shift as a function of solvent composition. As Figure S4.2 shows, the chemical shift of Li^+ in 1F-OSN moves downfield as the salt concentration increases as a result of the increasing association of Li^+ with the PF_6^- anion. Equation 4.4 therefore assumes that the degree of Li^+ dissociation from PF_6^- does not vary as a function of solvent composition in the electrolytes analyzed here. To test this assumption and therefore the validity of Equation 4.4, we calculated the degree of dissociation for all electrolyte systems studied using Equation 4.5:²⁷⁻

29

$$\alpha = \frac{\sigma_{\text{measured}}}{\sigma_{\text{NMR}}} = \frac{\sigma_{\text{measured}}}{\frac{e^2 N}{kT} (D_{\text{Li}} + D_{\text{PF}_6}) * 1000} \quad (4.5)$$

Where α is the degree of salt dissociation, σ_{measured} is the conductivity in mS/cm measured by a conductivity probe at 298 K, σ_{NMR} is the calculated conductivity in mS/cm, e is the electric charge in C, N is the ions per volume in mol/mL, k is the Boltzmann constant in J/K, T is the temperature in K, D_{Li} is the Li^+ diffusion coefficient in $\text{cm}^2 \text{s}^{-1}$, and D_{PF_6} is the PF_6^- diffusion coefficient in cm^2

s⁻¹. The relationship between the diffusion coefficients of the ions and the conductivity as shown in σ_{NMR} is the Nernst-Einstein equation. The diffusion coefficients were measured using a convection-compensated NMR pulse sequence as described in the Materials and Methods section. A representative ¹⁹F DOSY NMR series of spectra, and the linear fit to extract the diffusion coefficient, are shown in Figure S4.3. It is important to note that Equation 4.5 is an underestimate of the degree of dissociation, since the diffusion coefficients measured by NMR are an average of the free and paired ionic species' diffusion coefficients.²⁸ However, relative changes in the degree of dissociation between electrolyte samples should be valid.

Table 4.2 shows the results of the diffusion coefficient and conductivity measurements, and σ_{NMR} and α calculations from Equation 4.5. The degree of dissociation for single solvent electrolytes is greatest for EC (0.62), followed by 1F-OSN (0.45), followed by DEC (0.16). The α values for EC and DEC are close to the values reported in literature of 0.71 and 0.17 respectively.³⁰ The trend of ionic dissociation follows the trend of dielectric constants for each solvent: EC = 90, 1F-OSN = 16, DEC = 3, and is also consistent with the calculated single solvent binding energies presented earlier.

For low (0.09-0.67) mole fractions of 1F-OSN with EC, the calculated degree of dissociation increases from 0.62 in pure EC to 0.64-0.79. As the mole fraction of 1F-OSN increases further, the degree of dissociation falls to a value (0.50) that is intermediate between that of pure 1F-OSN and pure EC. Similarly, in the DEC/1F-OSN series, the addition of 1F-OSN leads to an increase in ionic dissociation to 0.21-0.26 when DEC is the majority solvent species by mol%. At equimolar DEC/1F-OSN, the dissociation increases to 0.39, and when 1F-OSN is the majority solvent species the degree of dissociation is approximately equivalent to that in pure 1F-OSN (0.44-0.45).

These calculated degrees of dissociation for mixed electrolyte systems show that ionic dissociation is not constant with varying mole fractions of organosilicon and carbonate solvents. The largest change in the degree of dissociation from pure EC to mixed EC/1F-OSN was 27%, which might not be significant enough to impact the ^6Li chemical shift in Equation 4.3. However, the degree of dissociation in 1/5 and 1/2 DEC/1F-OSN was a 181% increase in the ionic dissociation for pure DEC. Therefore, we postulate that at least part of the downfield shift of the lithium peak with increasing mole fraction of DEC in DEC/1F-OSN mixtures, and indeed the chemical shift of lithium in pure DEC, is due to greater ionic association and the possible formation of contact ion pairs, and not solely due to lithium coordination by the DEC carbonyl. At this time we have not assessed a way of deconvoluting the ionic association and the carbonate deshielding contributions to the ^6Li chemical shift through NMR.

4.3.4 Fourier transform infrared spectroscopy qualitative analysis of solvation

We utilized Fourier transform infrared spectroscopy (FTIR) as a second analytical technique to further elucidate the nature of solvation in organosilicon and mixed organosilicon-carbonate lithium electrolytes. Previous studies have shown that the coordination of lithium by a carbonyl³¹⁻³² or nitrile³³⁻³⁵ can be detected through FTIR as a red- or blue-shift of the functional stretching frequency. We utilized liquid transmission FTIR to analyze pure EC, DEC, and 1F-OSN electrolytes and mixed solvent EC/1F-OSN and DEC/1F-OSN electrolytes, and gain an understanding of the solvation structure. Figure 4.2 shows the FTIR spectra of a series of LiPF_6 concentrations dissolved in DEC (Fig. 4.2a) or 1F-OSN (Fig. 4.2b). EC is a solid at room temperature and does not easily form solutions when mixed as a single solvent with LiPF_6 , especially with low salt concentrations, therefore we did not measure a corresponding concentration series of LiPF_6 in EC. The spectral region of the solvating functionality (carbonyl

for DEC and nitrile for 1F-OSN) shows two peaks for each solvent, representing separate species where the functionality is free, and where the functional group is coordinating to lithium.^{31, 33-35} Due to the high absorbance cross section of the DEC and EC carbonyl stretching frequencies, the transmission cell must utilize an ultrathin pathlength (<1 μm) to avoid total light absorbance at the carbonyl absorbance frequency, as described in the Materials and Method section. This cell showed nonnegligible sample-to-sample variability of the absorbance values. In Figure 4.2, the spectra are therefore scaled to the absorbance of the free peak to more clearly see the change in free/coordinating peak ratios.

In Figure 4.2a, the spectra show a series of 0.3-1.4M LiPF_6 dissolved in DEC. The peak observed at 1747 cm^{-1} was assigned to the free carbonyl, while the peak at $1712\text{-}1714\text{ cm}^{-1}$ was assigned to the carbonyl coordinating lithium, as reported previously.³¹⁻³² The red-shift of the carbonyl frequency upon binding to lithium is due to the donation of electron density to the cation from a solvent bonding orbital, leading to a decrease in the C=O bond order and decreased stretching frequency. The λ_{max} of the coordinating peak also shows a small blue-shift of 2 cm^{-1} with increasing salt concentration across the series studied. In Figure 4.2b, the spectra show a series of 0.1-1M LiPF_6 dissolved in 1F-OSN. The peak at 2247 cm^{-1} was assigned to the free nitrile, while the peak at 2271 cm^{-1} was assigned to the lithium-coordinating nitrile, as reported previously for lithium in other nitrile solvents.³³⁻³⁴ There is a smaller additional peak at $\sim 2285\text{ cm}^{-1}$ that was assigned to a combination band from a C-C stretch and CH_3 deformation, as reported in the literature.³⁴

The mixed electrolyte series EC/1F-OSN was analyzed by FTIR as shown in Figure 4.3. The carbonyl region in EC has an interfering Fermi resonance overlapping the coordinated carbonyl peak,³² so the carbonyl region was not included in this analysis. Figure 4.3a shows the

nitrile region for these mixed electrolytes, with the expected free nitrile (2247 cm^{-1}) and coordinated nitrile (2271 cm^{-1}) peaks. The peaks were fit using FitYK software as described in the experimental section (see Figure S4.4 for an example spectral fit) and the absorbance ratio of the free solvent and coordinating solvent peaks was calculated to give the results shown in the graph in Figure 4.3b. As the mole fraction of 1F-OSN in solution decreases from 1.0 to 0.5 (increasing EC content), the relative amount of coordinating to free nitrile decreases as well. Figure 4.3b shows the change in coordinating/free ratio peak absorbances of the nitrile with changing mole fraction of 1F-OSN, compared with the same peak ratio for different concentrations of LiPF_6 in pure 1F-OSN. In the 1/1 EC/1F-OSN electrolyte, the coordinating/free absorbance ratios are slightly less than for 0.5M LiPF_6 in pure 1F-OSN. As the mole fraction of 1F-OSN decreases further from 0.5 to 0.09, the relative ratios of coordinating and free nitrile do not significantly change. These data show that adding EC to a 1F-OSN electrolyte causes a decrease in the amount of solvating nitrile, suggesting it is favorable for the solvation shell in mixed EC/1F-OSN electrolytes to include EC, consistent with the NMR results showing that addition of the decreased the 1F-OSN contribution to the ^6Li chemical shift.

The mixed electrolyte series DEC/1F-OSN was analyzed by FTIR, and the results are shown in Figure 4.4. Figure 4.44a shows the change in the carbonyl region for DEC as a function of changing mole ratios of the two solvents. At low mole fractions of 1F-OSN (0.09 – 0.33), the ratio of coordinating/free carbonyl peaks remains approximately constant and close to the absorbance ratio measured in 1M LiPF_6 in pure DEC. As the mole fraction of 1F-OSN is further increased, the relative ratio of coordinating/free DEC increases as well, above the absorbance ratio measured for 1.8 M LiPF_6 in pure DEC (Figure 4.4c). Additionally, the free carbonyl peak shows a red shift and the coordinating carbonyl peak shows a blue shift, such that for 1/2 DEC/1F-OSN

and 1/5 DEC/1F-OSN the distinct peaks begin to merge; however, the peak fitting allows deconvolution of the separate species.

Figure 4.4b shows the change in the nitrile region for 1F-OSN in the DEC/1F-OSN series. Similar to the carbonyl region, the ratio of the coordinating and free nitrile peaks does not significantly change for mole ratios of 1F-OSN 0.09 – 0.67. In 1/5 DEC/1F-OSN, the coordinating/free nitrile peak ratio increases relative to the other mixed electrolytes to a similar value to the absorbance ratio in 1M LiPF₆ in pure 1F-OSN. Similar to EC, these results show that the addition of DEC to 1F-OSN causes a decrease in the amount of solvating nitrile. However, as is shown by comparing Figure 4.3b and Figure 4.4d, the decrease in the amount of solvating nitrile caused by EC is more significant than that caused by the same mole ratio of DEC/1F-OSN. These results could indicate DEC is preferentially part of the solvation sphere in mixed DEC/1F-OSN, but to a smaller extent than the preference for EC in EC/1F-OSN. These results are consistent with the NMR data shown in Figure 4.1.

The increase in solvating DEC with addition of 1F-OSN could also be partly explained by the increase in salt dissociation when 1F-OSN is added to DEC, as shown in Table 4.2: the degree of solvating DEC increases because there are more lithium ions available for solvation, while the degree of solvating 1F-OSN decreases when DEC is added because ionic dissociation increases and fewer lithium ions are available for solvation. In order to deconvolute the different possible contributions to the observed trends, we made an effort to quantitatively analyze the FTIR data.

4.3.4 Fourier transform infrared spectroscopy quantitative analysis of solvation

In order to quantify the speciation of the lithium solvation shell, we first determined the relative IR sensitivities of the free and lithium-coordinating peaks for each coordinating

functionality (carbonyl for DEC and nitrile for 1F-OSN) from the LiPF₆ concentration series spectra shown in Figure 4.2. Due to the overlapping Fermi resonance in the carbonyl spectral region of EC as stated earlier,³² this analysis was not performed for EC. We base this analysis on the notion that the concentration of solvent remains constant for all samples within each salt concentration series, and therefore any loss in signal from the free solvent peak must be balanced by a gain in signal for the coordinating solvent peak. If the IR sensitivities of the two peaks were equal, the ratio of the rate of change of each of the two peaks would be described by Equation 4.6:

$$\text{Absorbance Ratio Free/Coordinating Peaks} = \frac{x+b}{x} \quad (4.6)$$

Where x is the concentration of lithium, as long as the spectra are measured within a concentration range where the change in each of the species is linear as a function of lithium concentration. If the IR sensitivities of the two peaks are not equal, their relative sensitivities can be determined by the follow Equation 4.6 modification:

$$\text{Absorbance Ratio Free/Coordinating Peaks} = \frac{ax+b}{cx} = \frac{b}{x} + \frac{a}{c} \quad (4.7)$$

Where a is the slope of the line describing the decrease in the free solvent peak and c is the slope of the line describing the corresponding increase in the lithium coordinating peak, both as a function of increasing lithium concentration. The relative ratio of a to b describes the rate of change in free solvent peak relative to the rate of change of the coordinating solvent peak, and therefore the relative IR intensities of these bands. While the sample-to-sample absorbance variability precluded directly measuring either individual function $ax + b$ or cx , as Equation 4.7 shows, a plot of $\frac{1}{x}$ (inverse of the lithium concentration) vs the absorbance ratio of free/coordinating peaks will give the relative IR intensities as the y -intercept of the resulting linear line. If Equation 4.7 does not describe the relationship between inverse lithium concentration and the peak absorbance ratios,

the linear fit should be poor; therefore, we use the goodness of a linear fit as a check to assess the validity of Equation 4.7 for these electrolytes.

Figure 4.5 shows the results of this analysis for a concentration series of LiPF_6 in DEC (Fig. 4.5a) and a concentration series of LiPF_6 in 1F-OSN (Fig. 4.5b). The range of lithium concentrations analyzed here were $\leq 1\text{M}$, to avoid any nonlinearity due to significant ion pairing that may occur at high salt concentrations. The linear fit of both DEC and 1F-OSN data series give $R^2 > 0.995$. For DEC, the y-intercept (a/c) is -2.680 ± 0.560 and for 1F-OSN, the y-intercept is -0.541 ± 0.187 . Therefore, to normalize the measured free solvent peak for its relative IR sensitivity to the coordinating peak, we multiplied the free DEC peak absorbance by 0.373 and the free 1F-OSN peak by 1.85. The sensitivity-normalized absorbances were then used to calculate mol% of free solvent and mol% of coordinating solvent for DEC and for 1F-OSN. Based on the known concentrations of each solvent in the electrolyte, the total concentration of solvent coordinating to lithium, $[\text{Solvent--Li}^+]$ (equal to the nominal solvation number, given the lithium concentration of 1M) for each sample was also calculated. Finally, the % organosilicon present in the solvation shell was determined from the $[\text{CN--Li}^+]$ fraction of the total $[\text{Solvent--Li}^+]$. The results of these calculations are shown in Table 4.3. In the single-solvent electrolyte 1F-OSN + 1M LiPF_6 , 56% of the total solvent is coordinating lithium (average solvation number of 3.3). In DEC + 1M LiPF_6 , 65% of the total solvent is coordinating lithium (average solvation number of 5.4). Considering that we calculated a greater ionic dissociation for 1F-OSN + 1M LiPF_6 (0.45) than DEC + 1M LiPF_6 (0.16), these results suggest that a greater number of solvent molecules are required to solvate lithium in pure DEC than in pure 1F-OSN. In mixed EC/1F-OSN, the percentage of 1F-OSN coordinating to lithium is strongly dependent on the mole fraction of EC, with only 25% of 1F-OSN coordinating at 10/1 EC/1F-OSN. In mixed DEC/1F-OSN the percentage of 1F-OSN

coordinating to lithium drops to ~50% when the mole fraction of 1F-OSN is less than 0.83, but remains constant with further decreasing 1F-OSN mole fraction. These results are consistent with the previous data showing that EC contributes more strongly than DEC over 1F-OSN to the solvation shell.

Figure 4.6a shows the 1F-OSN % of the solvation shell in the DEC/1F-OSN series plotted against the 1F-OSN composition in solution. This graph shows that 1F-OSN participates in the solvation shell to a degree that is slightly less than its fraction in composition, and therefore DEC slightly dominates the composition of the solvation shell. For example, when DEC and 1F-OSN are present in equimolar quantities, the solvation shell is 58% DEC and 42% 1F-OSN. We note that this measurement includes a large degree of uncertainty due to the error in the linear fits from Figure 4.5 (the error bars in Figure 4.6a and 4.6b). However, these results are in excellent agreement with the 1F-OSN fraction of the ^6Li -NMR chemical shift shown in Figure 4.1. Figure 4.6b shows the calculated nominal solvation number based on the ratio of the to the concentration of LiPF_6 in solution (1M for all samples), also as a function of the 1F-OSN mole fraction in solution. At 91 mol% DEC, the lithium is coordinated on average by 5.0 solvent molecules. As the mole fraction of 1F-OSN in solution increases, the solvation number decreases correspondingly, and in 83% 1F-OSN, the lithium is coordinated on average by 3.8 solvent molecules.

4.4 Conclusions

In this study, we analyzed the nature of the solvation shell in binary electrolytes with a fluorinated organosilicon nitrile solvent (1F-OSN) mixed with either EC or DEC in varying mole ratios of solvents, with 1M LiPF_6 . We used DFT calculations to determine the solvation binding energies of lithium solvation clusters in the gas phase and in a dielectric medium model. We measured the contribution of each solvent species to the ^6Li -NMR signal and determined the

degree of dissociation using the solution conductivity and the ion diffusion coefficients measured by ^7Li - and ^{19}F -NMR. Finally, we used FTIR to qualitatively assess changes in each solvent's coordination to lithium with changing 1F-OSN mole fraction in solution, and we further describe efforts to quantify the speciation of the solvation shell in mixed-solvent electrolytes.

The preliminary DFT calculations suggest that a primary lithium solvation shell with equal amounts of DEC and 1F-OSN may be the most stable for DEC/1F-OSN mixed electrolytes, while all solvation shells containing at least one EC molecule may be approximately equally favorable for EC/1F-OSN mixed electrolytes. Both NMR and FTIR show that the lithium solvation sphere in DEC/1F-OSN mixed electrolytes has a greater % of DEC relative to its composition in the solution than 1F-OSN. In EC/1F-OSN, the % of carbonate in the solvation shell is even greater than in DEC/1F-OSN. Importantly, 1F-OSN is yet a non-negligible component of the solvation shell (5-8%) even at a low concentration in solution (9 mol%). Calculations of the degree of dissociation from measured ion diffusion coefficients and solution conductivity show that adding a mol fraction of 1F-OSN to a lithium electrolyte of either EC or DEC causes an increase in the ionic dissociation. Therefore, despite the lower % solvation shell contribution of the organosilicon, we show 1F-OSN to have an impact on the bulk solvation properties of these binary electrolytes. The presence of 1F-OSN also impacts the nominal solvation number in DEC/1F-OSN mixed electrolytes, with the addition of 1F-OSN decreasing the preferred or required solvation number of lithium. The impact of 1F-OSN on the nominal solvation number of EC/1F-OSN electrolytes was not assessed. The lower solvation number but higher ionic dissociation of 1F-OSN-containing lithium electrolytes relative to DEC electrolytes may suggest that fewer 1F-OSN molecules in the solvation shell are more favored and yet overall the 1F-OSN has a greater impact on solvation, and

suggests that purely quantifying % of different solvent species in the primary solvation shell in mixed electrolytes cannot capture the full role of each different solvent.

We propose that the organosilicon has a significant impact on the solvation shell of lithium electrolytes even when present at a lower % of the solvation sphere, due to a more favorable lower solvation number and impact on the dissociation of the salt. Future solvation studies may focus on how the bulk lithium solvation changes at the electrode-electrolyte interface, for different electrode materials, and under varying electrode polarizations.

4.5 Figures

Table 4.1 Solvation cluster binding energies (in kcal mol⁻¹) from DFT calculations

Solvent cluster	Gas-phase	Implicit solvation ($\epsilon = 20$)
Li ⁺ 1F-OSN	-46.9	-3.82
Li ⁺ EC	-49.2	-3.73
Li ⁺ DEC	-40.7	-3.37
Li ⁺ (1F-OSN) ₄	-117.7	-13.8
Li ⁺ (EC) ₄	-123.5	-*
Li ⁺ (DEC) ₄	-113.1	-*
Li ⁺ (EC) ₃ (1F-OSN)	-123.8	-15.8
Li ⁺ (EC) ₂ (1F-OSN) ₂	-123.4	-15.8
Li ⁺ (EC)(1F-OSN) ₃	-123.2	-15.5
Li ⁺ (DEC) ₃ (1F-OSN)	-116.5	-*
Li ⁺ (DEC) ₂ (1F-OSN) ₂	-118.9	-16.5
Li ⁺ (DEC)(1F-OSN) ₃	-108.9	-4.6

*Geometries did not converge to optimized minimum with zero negative eigenvalues

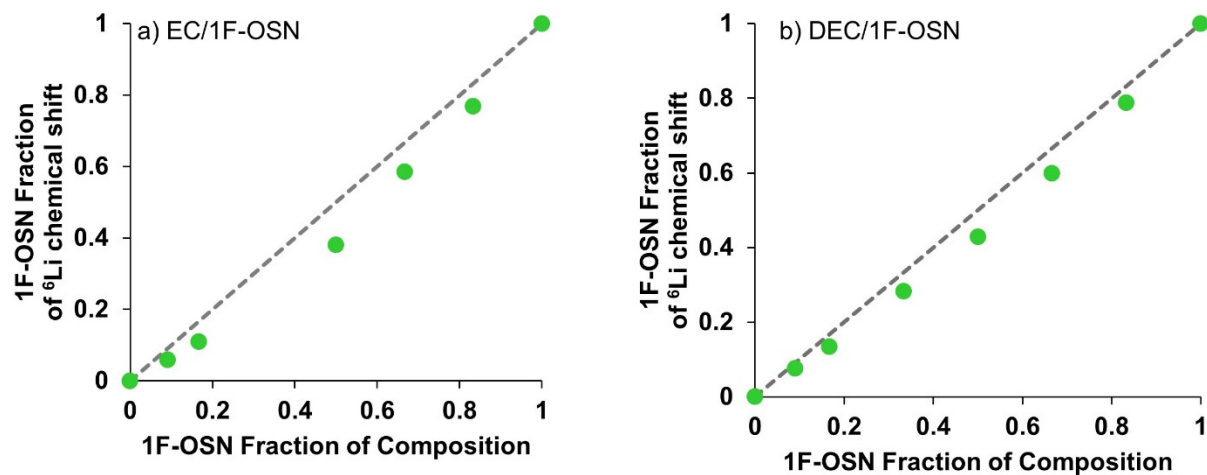


Figure 4.1 Calculated fraction of 1F-OSN contributing to the ${}^6\text{Li}$ peak chemical shift in a) EC/1F-OSN and b) DEC/1F-OSN mixed solvent electrolytes. All electrolytes have 1M LiPF_6 . Grey dashed line represents the expected result if the fraction of 1F-OSN contributing to the solvation shell were equivalent to its fraction of composition.

Table 4.2 Diffusion coefficients of the cation (D_{Li}) and anion (D_{PF6}), calculated conductivity from the diffusion coefficients (σ_{NMR}), measured conductivity ($\sigma_{measured}$), and degree of dissociation (α)

Electrolyte (all with 1M LiPF₆)	D_{Li} ($10^{-6} \text{ cm}^2 \text{ s}^{-1}$)	D_{PF6} ($10^{-6} \text{ cm}^2 \text{ s}^{-1}$)	Calculated Conductivity σ_{NMR} (mS/cm)	Measured Conductivity $\sigma_{measured}$ (mS/cm)	Degree of Dissociation α
1F-OSN	0.67	0.74	5.3	2.38	0.45
EC	1.7	1.6	12.2	7.63 ¹	0.62
DEC	2.4	2.9	19.8	3.22 ¹	0.16
10/1 EC/1F-OSN	0.86	1.6	9.2	7.05	0.77
5/1 EC/1F-OSN	0.69	1.5	8.1	6.38	0.79
1/1 EC/1F-OSN	0.51	0.91	5.3	4.03	0.76
1/2 EC/1F-OSN	0.48	0.90	5.2	3.33	0.64
1/5 EC/1F-OSN	0.53	0.94	5.5	2.79	0.50
10/1 DEC/1F-OSN	2.0	1.5	13.2	3.38	0.26
5/1 DEC/1F-OSN	2.2	2.5	17.5	3.62	0.21
2/1 DEC/1F-OSN	1.3	2.6	14.7	3.73	0.25
1/1 DEC/1F-OSN	1.4	1.1	9.3	3.65	0.39
1/2 DEC/1F-OSN	0.9	1.0	7.2	3.23	0.45
1/5 DEC/1F-OSN	0.5	1.2	6.4	2.84	0.44

¹Values from Hayamizu, K. *Electrochim. Acta*, 254, 2017, Supporting Information, calculated at 25 °C from linear trendline of conductivity with surrounding temperatures.

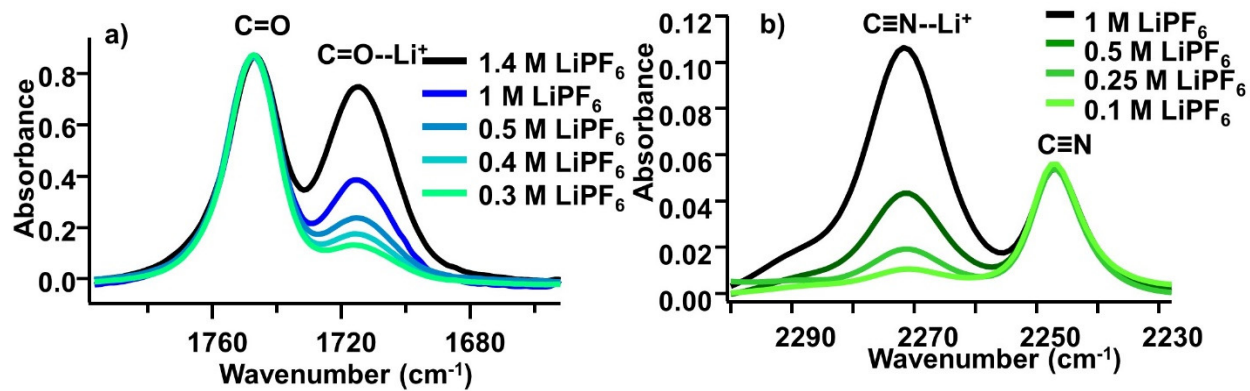


Figure 4.2 FTIR spectra of concentration series of LiPF_6 in a) DEC and b) 1F-OSN. Spectra are scaled to the free solvent peak.

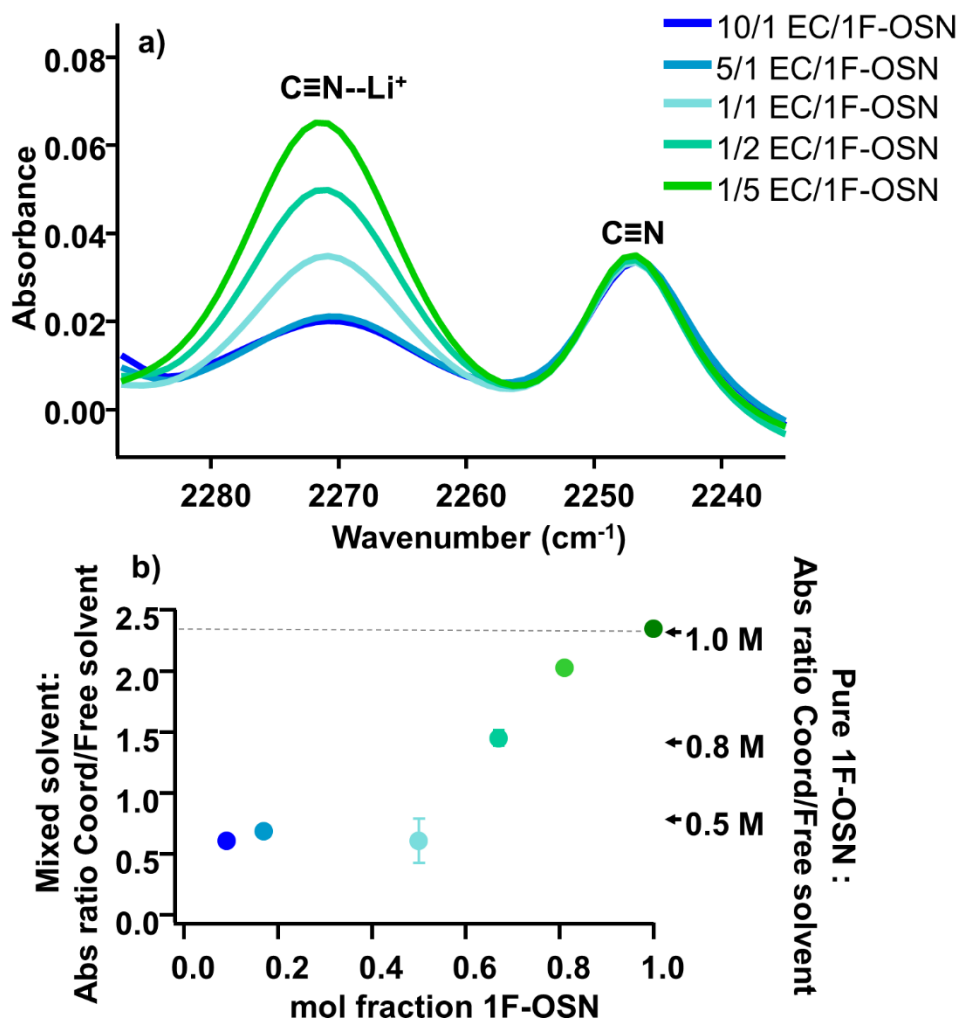


Figure 4.3 a) FTIR spectra of the EC/1F-OSN mixed electrolyte series nitrile region, all with 1M LiPF₆, and b) the corresponding graph of the ratio of coordinating/free solvent peak absorbances as a function of mole fraction of 1F-OSN. The left y-axis represents the peak absorbance ratios for the mixed solvent electrolytes, while the arrows on the right indicate the corresponding absorbance ratio for the labeled lithium salt concentration in 1F-OSN single solvent electrolyte.

The grey dashed line represents the peak absorbance ratio for 1M LiPF₆ in 1F-OSN.

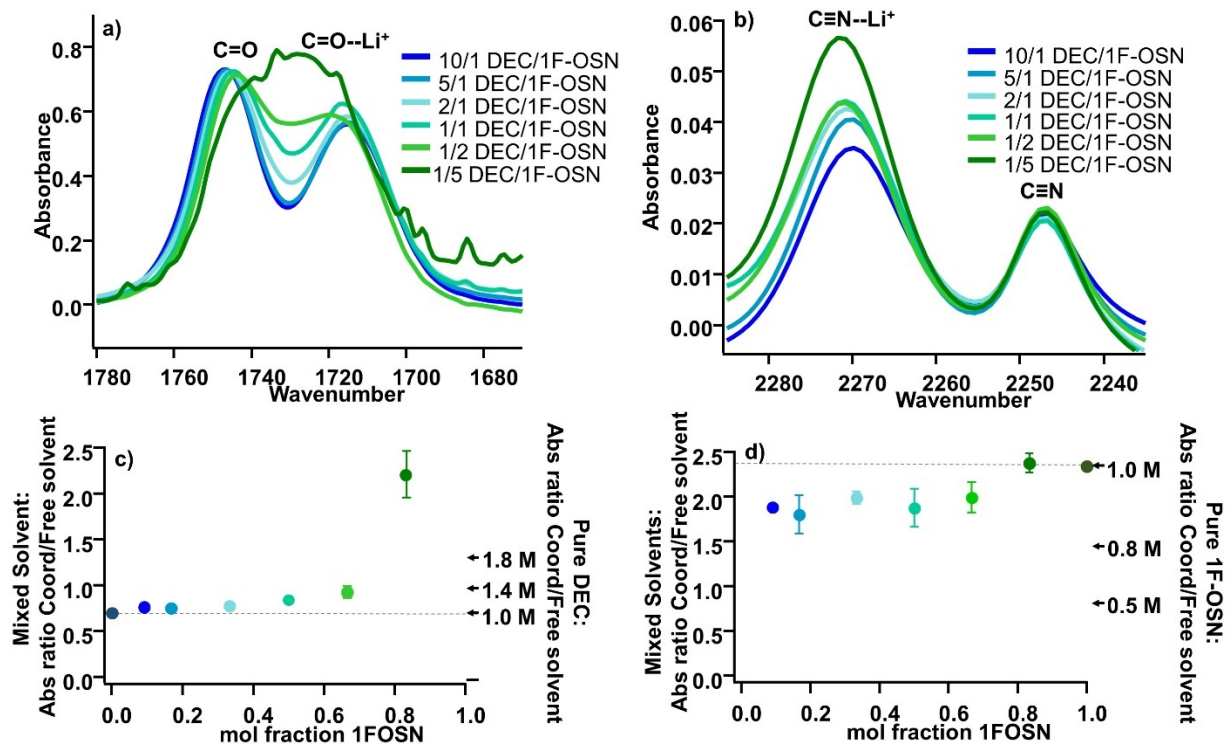


Figure 4.4 FTIR spectra of DEC/1F-OSN mixed electrolytes with varying mole ratios of DEC and 1F-OSN, scaled to the absorbance of the free solvent peak for each spectral region: a) DEC carbonyl region and b) 1F-OSN nitrile region, all with 1M LIPF₆. Corresponding graphs of the ratio of coordinating/free solvent peak absorbances as a function of mole fraction of 1F-OSN for c) the DEC carbonyl peaks and d) the 1F-OSN nitriles peaks. Left y-axes represent the peak absorbance ratios for the mixed solvent electrolytes, while the arrows on the right indicate the corresponding absorbance ratio for the labeled lithium salt concentration in the single solvent electrolyte. The grey dashed line represents the peak absorbance ratio for 1M LIPF₆ in the single solvent.

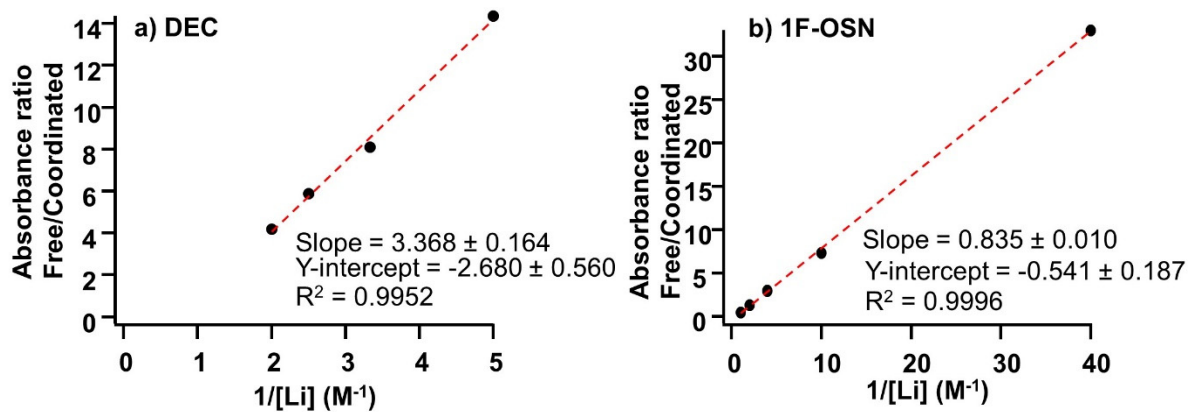


Figure 4.5 Graphs of the absorbance ratio of free/coordinated solvent peaks as a function of inverse lithium concentration.

Table 4.3 Quantitative Speciation of the Solvation Shell from FTIR analysis¹

Electrolyte (all with 1M LiPF ₆)	% of organosilicon coordinating to Li	% of carbonate coordinating to Li	Solvation number	% organosilicon composition	% organosilicon in solvation shell
1F-OSN	56 ±15%	-	3.3 ±1	100%	100%
DEC	-	65 ±7%	5.4 ±0.6	0%	0%
10/1 DEC/1F- OSN	51 ±17%	67 ±7%	5.0 ±0.5	9 %	7 ±3%
5/1 DEC/1F- OSN	49 ±18%	67 ±7%	4.7 ±0.5	17%	13 ±5%
2/1 DEC/1F- OSN	52 ±17%	68 ±6%	4.4 ±0.5	33%	28 ±10%
1/1 DEC/1F- OSN	50 ±18%	70 ±6%	4.0 ±0.7	50%	42 ±17%
1/2 DEC/1F- OSN	52 ±18%	71 ±3%	3.7 ±0.8	67%	59 ±24%
1/5 DEC/1F- OSN	56 ±15%	86 ±7%	3.8 ±0.8	83%	77 ±26%
10/1 EC/1F-OSN	25 ±26%	-	-	-	-
5/1 EC/1F-OSN	27 ±25%	-	-	-	-
1/1 EC/1F-OSN	32 ±26%	-	-	-	-
1/2 EC/1F-OSN	44 ±20%	-	-	-	-
1/5 EC/1F-OSN	52 ±17%	-	-	-	-

¹ ± values represent uncertainty based on the uncertainty in the y-intercept of the fit line in Figure 4.5

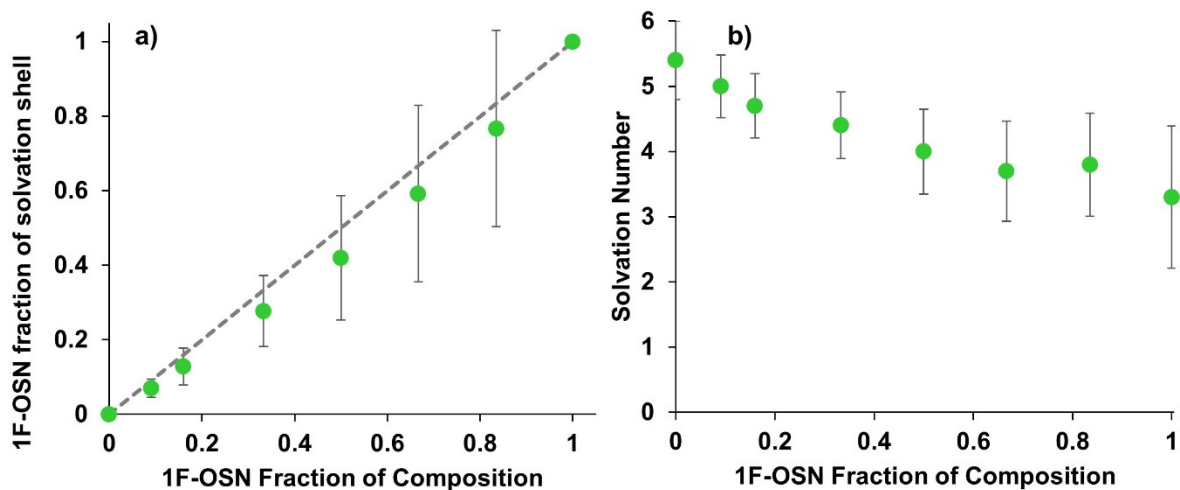


Figure 4.6 As a function of 1F-OSN fraction of composition in mixed DEC/1F-OSN + 1M LiPF₆ electrolytes, a) 1F-OSN fraction of solvation shell and b) solvation number, calculated from FTIR absorbance ratios of free and coordinating 1F-OSN and DEC peaks. The error bars here represent the uncertainty of each value from the standard deviation of the fit line y-intercepts in

Figure 4.5.

Table S4.1. DOSY NMR parameters for each electrolyte sample

Sample	$^7\text{Li } \delta$ (μs)	$^7\text{Li } \Delta$ (s)	$^{19}\text{F } \delta$ (μs)	$^{19}\text{F } \Delta$ (s)
1 M LiPF_6 in EC	3200	1.0	2000	0.36
1 M LiPF_6 in OS3	3000	0.35	3000	1.0
1 M LiPF_6 in DEC	3000	0.8	2000	0.4
10:1 EC:OS3 + 1 M LiPF_6	3000	1.0	3000	1.0
5:1 EC:OS3 + 1 M LiPF_6	4400	1.0	2000	0.5
1:1 EC:OS3 + 1 M LiPF_6	6000	0.7	4000	0.9
1:2 EC:OS3 + 1 M LiPF_6	6000	0.45	2000	0.5
1:5 EC:OS3 + 1 M LiPF_6	5000	0.4	2000	0.5
10:1 DEC:OS3 + 1 M LiPF_6	3000	0.5	2000	0.5
5:1 DEC:OS3 + 1 M LiPF_6	5000	0.7	2000	0.5
2:1 DEC:OS3 + 1 M LiPF_6	5700	0.5	2000	0.5
1:1 DEC:OS3 + 1 M LiPF_6	2000	0.5	2000	0.5
1:2 DEC:OS3 + 1 M LiPF_6	4000	0.4	2000	0.5
1:5 DEC:OS3 + 1 M LiPF_6	5000	0.4	2000	0.5

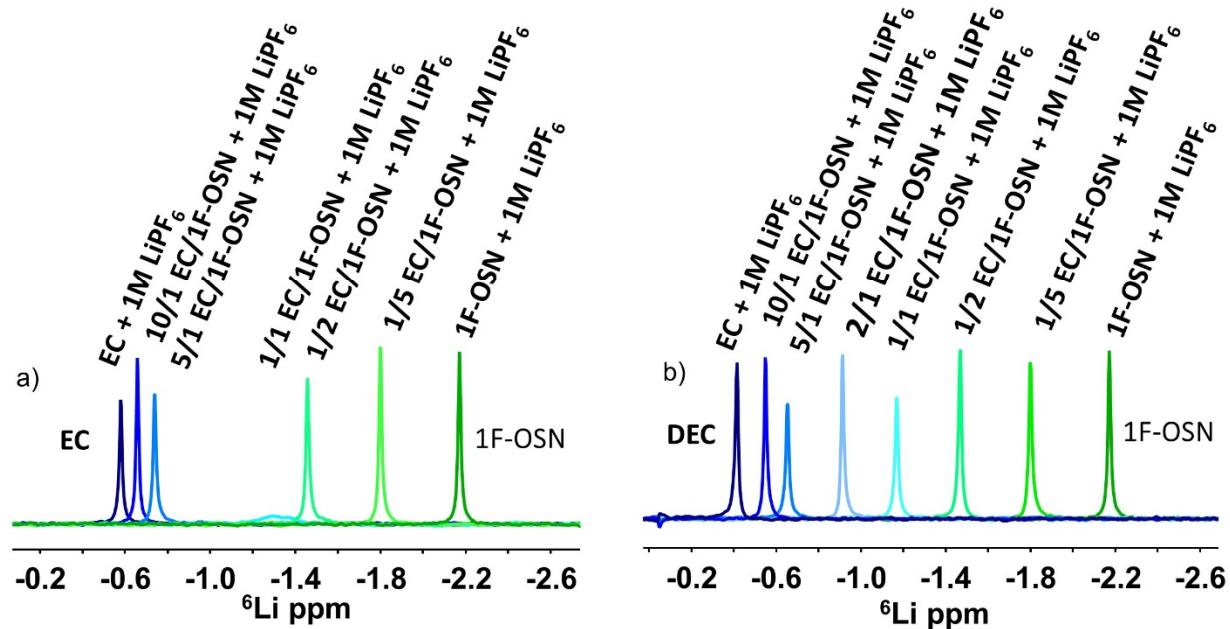


Figure S4.1 ^6Li -NMR of a) EC/1F-OSN and b) DEC/1F-OSN mixed electrolytes, along with corresponding single-solvent EC, DEC, and 1F-OSN electrolytes. All electrolytes have 1M LiPF₆.

Table S4.2 ^6Li -NMR chemical shifts and calculated contribution to the lithium solvation environment for varying 1F-OSN composition fractions in a) EC/1F-OSN electrolyte mixtures and b) DEC/1F-OSN electrolyte mixtures

a)

Composition (mol%)		^6Li (ppm)	Solvation (mol%)	
EC	OS3		EC	OS3
100%	-	-0.58	100%	-
91%	9%	-0.66	95.1%	4.94%
83%	17%	-0.74	90.0%	10.0%
50%	50%	-1.2	62.7%	37.3%
33%	67%	-1.5	41.9%	58.1%
17%	83%	-1.8	23.4%	76.6%
-	100%	-2.2	-	100%

b)

Composition (mol%)		^6Li (ppm)	Solvation (mol%)	
DEC	OS3		DEC	OS3
100%	-	-0.41	100%	-
91%	9%	-0.55	92%	8%
83%	17%	-0.65	86%	14%
67%	33%	-0.91	72%	28%
50%	50%	-1.2	57%	43%
33%	67%	-1.5	40%	60%
17%	83%	-1.8	21%	79%
-	100%	-2.2	-	100%

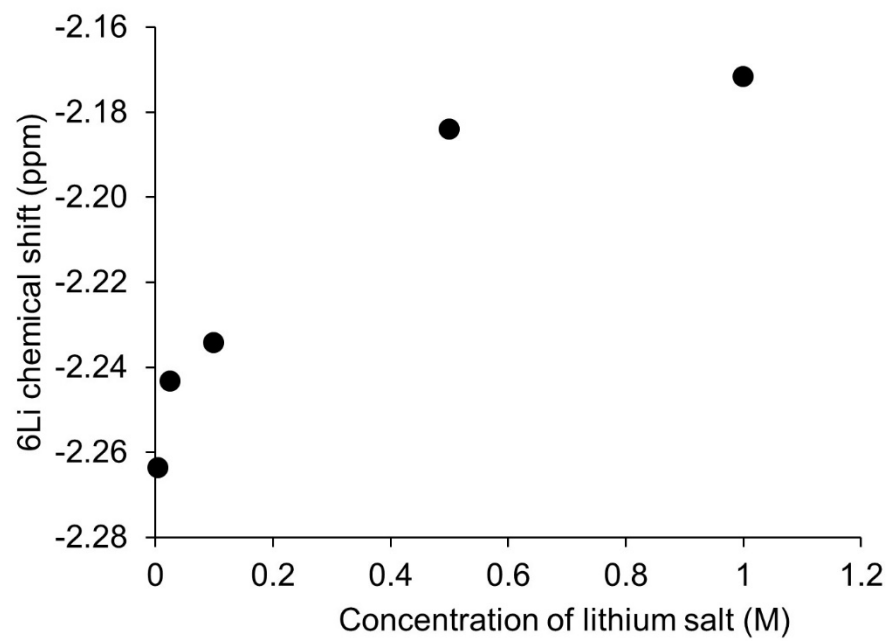
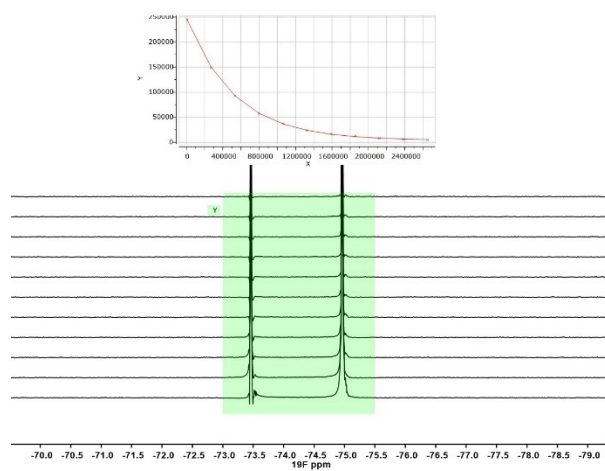


Figure S4.2 ${}^6\text{Li}$ -NMR chemical shift in 1F-OSN as a function of LiPF_6 concentration

^{19}F -DOSY NMR of 10/1 DEC/1F-OSN + 1M LiPF_6



Linear fit of ^{19}F -DOSY NMR of 10/1 DEC/1F-OSN + 1M LiPF_6 for D_{PF_6}

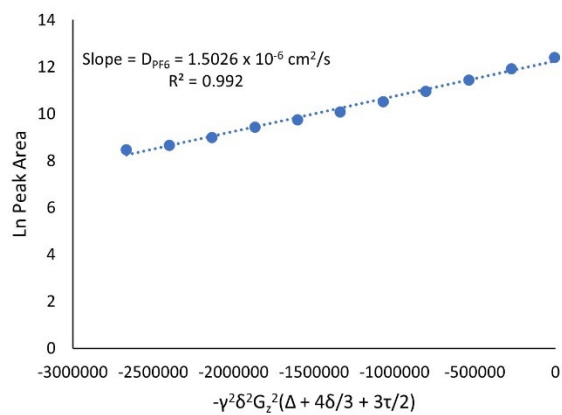


Figure S4.3. Sample DOSY ^{19}F -NMR spectra of PF_6 doublet and peak area decay as a function of gradient strength (left); linear fit to give diffusion coefficient (right)

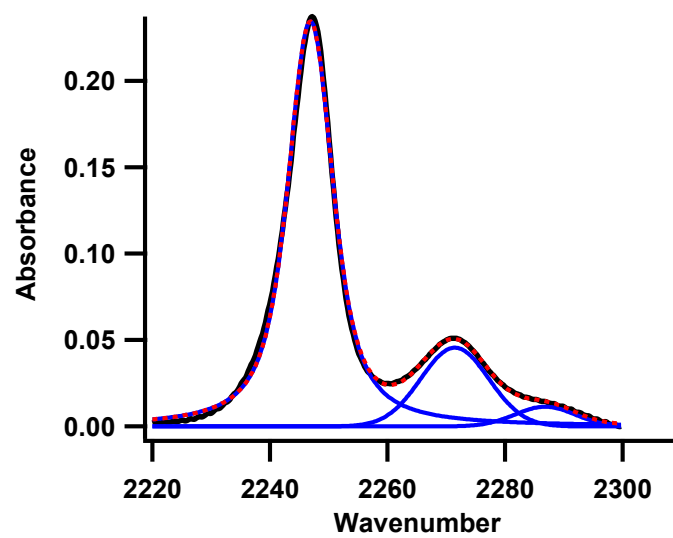


Figure S4.4 Example of peak fitting with FitYK software for 0.2M LiPF₆ in 1F-OSN

4.6 References

1. Tasaki, K.; Goldberg, A.; Winter, M., On the difference in cycling behaviors of lithium-ion battery cell between the ethylene carbonate- and propylene carbonate-based electrolytes. *Electrochimica Acta* **2011**, *56* (28), 10424-10435.
2. Zhuang, G. V.; Xu, K.; Yang, H.; Jow, T. R.; Ross, P. N., Jr., Lithium ethylene dicarbonate identified as the primary product of chemical and electrochemical reduction of EC in 1.2 M LiPF₆/EC:EMC electrolyte. *J Phys Chem B* **2005**, *109* (37), 17567-73.
3. Xu, K., Electrolytes and Interphases in Li-Ion Batteries and Beyond. *Chemical Reviews* **2014**, *114* (23), 11503-11618.
4. Ue, M.; Sasaki, Y.; Tanaka, Y.; Morita, M., Nonaqueous Electrolytes with Advances in Solvents. In *Electrolytes for Lithium Ion Batteries*, Jow, T. R.; Borodin, O.; Xu, K.; Ue, M., Eds. Springer Science: New York, 2014; pp 93-166.
5. Abe, K., Nonaqueous Electrolytes and Advances in Additives. In *Electrolytes for Lithium and Lithium-Ion Batteries*, Jow, T. R.; Xu, K.; Borodin, O.; Ue, M., Eds. Springer: New York, 2014; pp 167-210.
6. Zhang, L.; Zhang, Z.; Harring, S.; Straughan, M.; Butorac, R.; Chen, Z.; Lyons, L.; Amine, K.; West, R., Highly conductive trimethylsilyl oligo(ethylene oxide) electrolytes for energy storage applications. *J. Mater. Chem.* **2008**, *18* (31), 3713-3717.
7. Chen, X.; Usrey, M.; Peña-Hueso, A.; West, R.; Hamers, R. J., Thermal and electrochemical stability of organosilicon electrolytes for lithium-ion batteries. *Journal of Power Sources* **2013**, *241*, 311-319.
8. Guillot, S. L.; Peña-Hueso, A.; Usrey, M. L.; Hamers, R. J., Thermal and Hydrolytic Decomposition Mechanisms of Organosilicon Electrolytes with Enhanced Thermal Stability for Lithium-Ion Batteries. *Journal of The Electrochemical Society* **2017**, *164* (9), A1907-A1917.
9. Guillot, S. L.; Pena-Hueso, A.; Usrey, M. L.; Yu, Z.; Hamers, R. J., Mechanistic Insights into High Oxidative Stability of Organosilicon Nitrile Electrolytes for Lithium-ion Batteries. Manuscript in Prep, 2019.
10. Wojdyr, M., Fityk: a general-purpose peak fitting program. *Journal of Applied Crystallography* **2010**, *43* (5 Part 1), 1126-1128.
11. Harris, R. K.; Becker, E. D.; Menezes, S. M. C. D.; Granger, P.; Hoffman, R. E.; Zilm, K. W., Further Conventions for NMR Shielding and Chemical Shifts (IUPAC Recommendations 2008). *Magnetic Resonance in Chemistry* **2008**, *46* (6), 582-598.
12. Jerschow, A.; Müller, N., Convection Compensation in Gradient Enhanced Nuclear Magnetic Resonance Spectroscopy. *Journal of Magnetic Resonance* **1998**, *132* (1), 13-18.

13. Jerschow, A.; Muller, N., Suppression of convection artifacts in stimulated-echo diffusion experiments. Double-stimulated-echo experiments. *J. Magn. Reson.* **1997**, *125* (2), 372-375.
14. M. J. Frisch, G. W. T., H. B. Schlegel, G. E. Scuseria, M. A. Robb, J. R. Cheeseman, G. Scalmani, V. Barone, G. A. Petersson, H. Nakatsuji, X. Li, M. Caricato, A. Marenich, J. Bloino, B. G. Janesko, R. Gomperts, B. Mennucci, H. P. Hratchian, J. V. Ortiz, A. F. Izmaylov, J. L. Sonnenberg, D. Williams-Young, F. Ding, F. Lipparini, F. Egidi, J. Goings, B. Peng, A. Petrone, T. Henderson, D. Ranasinghe, V. G. Zakrzewski, J. Gao, N. Rega, G. Zheng, W. Liang, M. Hada, M. Ehara, K. Toyota, R. Fukuda, J. Hasegawa, M. Ishida, T. Nakajima, Y. Honda, O. Kitao, H. Nakai, T. Vreven, K. Throssell, J. A. Montgomery, Jr., J. E. Peralta, F. Ogliaro, M. Bearpark, J. J. Heyd, E. Brothers, K. N. Kudin, V. N. Staroverov, T. Keith, R. Kobayashi, J. Normand, K. Raghavachari, A. Rendell, J. C. Burant, S. S. Iyengar, J. Tomasi, M. Cossi, J. M. Millam, M. Klene, C. Adamo, R. Cammi, J. W. Ochterski, R. L. Martin, K. Morokuma, O. Farkas, J. B. Foresman, and D. J. Fox, Gaussian 09, Revision A.02. Gaussian, Inc., Wallingford CT, 2016.
15. Borodin, O.; Olguin, M.; Ganesh, P.; Kent, P. R. C.; Allen, J. L.; Henderson, W. A., Competitive lithium solvation of linear and cyclic carbonates from quantum chemistry. *Physical Chemistry Chemical Physics* **2016**, *18* (1), 164-175.
16. Skarmoutsos, I.; Ponnuchamy, V.; Vetere, V.; Mossa, S., Li⁺ Solvation in Pure, Binary, and Ternary Mixtures of Organic Carbonate Electrolytes. *J. Phys. Chem. C* **2015**, *119* (9), 4502-4515.
17. Ikezawa, Y.; Nishi, H., In situ FTIR study of the Cu electrode/ethylene carbonate+dimethyl carbonate solution interface. *Electrochimica Acta* **2008**, *53* (10), 3663-3669.
18. Borodin, O.; Smith, G. D., Quantum Chemistry and Molecular Dynamics Simulation Study of Dimethyl Carbonate: Ethylene Carbonate Electrolytes Doped with LiPF₆. *The Journal of Physical Chemistry B* **2009**, *113* (6), 1763-1776.
19. Wang, Y.; Balbuena, P. B., Theoretical studies on cosolvation of Li ion and solvent reductive decomposition in binary mixtures of aliphatic carbonates. *International Journal of Quantum Chemistry* **2005**, *102* (5), 724-733.
20. Shakourian-Fard, M.; Kamath, G.; Sankaranarayanan, S. K. R. S., Evaluating the Free Energies of Solvation and Electronic Structures of Lithium-Ion Battery Electrolytes. *ChemPhysChem* **2016**, *17* (18), 2916-2930.
21. Yuan, K.; Bian H Fau - Shen, Y.; Shen Y Fau - Jiang, B.; Jiang B Fau - Li, J.; Li J Fau - Zhang, Y.; Zhang Y Fau - Chen, H.; Chen H Fau - Zheng, J.; Zheng, J., Coordination number of Li⁺ in nonaqueous electrolyte solutions determined by molecular rotational measurements. (1520-5207 (Electronic)).
22. Yuan, K.; Bian, H.; Shen, Y.; Jiang, B.; Li, J.; Zhang, Y.; Chen, H.; Zheng, J., Coordination number of Li⁺ in nonaqueous electrolyte solutions determined by molecular rotational measurements. *J Phys Chem B* **2014**, *118* (13), 3689-95.

23. Su, C.-C.; He, M.; Amine, R.; Chen, Z.; Amine, K., Internally Referenced DOSY-NMR: A Novel Analytical Method in Revealing the Solution Structure of Lithium-Ion Battery Electrolytes. *The Journal of Physical Chemistry Letters* **2018**, *9* (13), 3714-3719.
24. Günther, H., *NMR Spectroscopy : Basic Principles, Concepts and Applications in Chemistry*. John Wiley & Sons, Incorporated: Somerset, GERMANY, 2013.
25. Jacobsen, N. E., NMR Spectroscopy Explained: Simplified Theory, Applications and Examples for Organic Chemistry and Structural Biology. In *Advanced NMR Theory: NOESY and DQF-COSY* [Online] Wiley: 2007.
26. Lyons, L. J.; Pena-Hueso, A.; Johnson, T.; West, R., Silyl and silyl/carbonate blend electrolytes for lithium-ion battery applications. *ECS Trans.* **2016**, *73* (1, 18th International Meeting on Lithium Batteries (IMLB 2016)), 281-288.
27. Aihara, Y.; Sugimoto, K.; Price, W. S.; Hayamizu, K., Ionic conduction and self-diffusion near infinitesimal concentration in lithium salt-organic solvent electrolytes. *The Journal of Chemical Physics* **2000**, *113* (5), 1981-1991.
28. Hayamizu, K., Direct relations between ion diffusion constants and ionic conductivity for lithium electrolyte solutions. *Electrochimica Acta* **2017**, *254*, 101-111.
29. Hayamizu, K., Temperature Dependence of Self-Diffusion Coefficients of Ions and Solvents in Ethylene Carbonate, Propylene Carbonate, and Diethyl Carbonate Single Solutions and Ethylene Carbonate + Diethyl Carbonate Binary Solutions of LiPF₆ Studied by NMR. *Journal of Chemical & Engineering Data* **2012**, *57* (7), 2012-2017.
30. Chapman, N.; Borodin, O.; Yoon, T.; Nguyen, C. C.; Lucht, B. L., Spectroscopic and Density Functional Theory Characterization of Common Lithium Salt Solvates in Carbonate Electrolytes for Lithium Batteries. *The Journal of Physical Chemistry C* **2017**, *121* (4), 2135-2148.
31. Seo, D. M.; Reiningger, S.; Kutcher, M.; Redmond, K.; Euler, W. B.; Lucht, B. L., Role of Mixed Solvation and Ion Pairing in the Solution Structure of Lithium Ion Battery Electrolytes. *The Journal of Physical Chemistry C* **2015**, *119* (25), 14038-14046.
32. Barthel, J.; Buchner, R.; Wismeth, E., FTIR Spectroscopy of Ion Solvation of LiClO₄ and LiSCN in Acetonitrile, Benzonitrile, and Propylene Carbonate. *Journal of Solution Chemistry* **2000**, *29* (10), 937-954.
33. Xuan, X.; Zhang, H.; Wang, J.; Wang, H., Vibrational Spectroscopic and Density Functional Studies on Ion Solvation and Association of Lithium Tetrafluoroborate in Acetonitrile. *The Journal of Physical Chemistry A* **2004**, *108* (37), 7513-7521.
34. Seo, D. M.; Borodin, O.; Han, S.-D.; Boyle, P. D.; Henderson, W. A., Electrolyte Solvation and Ionic Association II. Acetonitrile-Lithium Salt Mixtures: Highly Dissociated Salts. *Journal of The Electrochemical Society* **2012**, *159* (9), A1489-A1500.

Chapter 5. Conclusions and Future Directions

Our energy needs today require batteries that are higher-voltage, longer-lasting, and safer. Lithium-ion energy cells have the potential to meet these needs in many applications, but the development of new materials to meet these demanding metrics is an ongoing, worldwide investigation. While many advances have been made in battery electrode materials, the battery electrolyte, historically based on LiPF_6 and carbonate solvents, remains one of the primary limiting factors in battery stability and performance. This thesis describes a class of novel lithium-ion battery solvents and additives, organosilicons. Herein, we undertake an investigation of the fundamental thermal, electrochemical, and solvation properties of organosilicons, compare them with traditional carbonates solvents, and shed light on mechanisms and molecular origins of their thermal, electrochemical, and solvation behavior.

We began by studying the electrolyte thermal stability, which in traditional carbonate electrolytes is a source of significant performance and safety issues in the battery. LiPF_6 will thermally degrade to irreversibly lose lithium and form HF, which goes on to degrade the electrode; additionally, gaseous thermal degradation products can form. We show that in organosilicons, the degradation of LiPF_6 and the formation of HF is eliminated or mitigated. By investigating the mechanisms of stability, we find that there are two main mechanisms of LiPF_6 thermal stabilization in organosilicons: 1) elimination of the catalytic degradation cycle seen in carbonates, due to the lack of reactivity between downstream hydrolysis products and organosilicons, and 2) formation of a reversible PF_5 complex in organosilicons that stabilizes this highly reactive Lewis acid. Further investigation of the thermal stability of fluorinated vs nonfluorinated organosilicon nitriles found that there is a thermal mechanism of fluorination of nonfluorinated organosilicons, and organosilicon glycols undergo a thermal intramolecular cyclization pathway. Therefore, we

ultimately conclude that all organosilicon-based electrolytes provide thermal protection for LiPF_6 even at very high (100 °C) temperatures, and within the series of organosilicons studied, the thermal stability was highest for fluorinated organosilicon nitriles. The exceptional thermal stability shown by organosilicon electrolytes show promise for these novel solvents in high-temperature battery applications.

In addition to thermal stability, high electrochemical stability is an important property of battery electrolytes. We investigated the mechanisms of oxidative stability for organosilicon nitrile-based electrolytes with 0-3 fluorines at the silicon atom using computation, voltammetry, NMR, and XPS. DFT calculations indicated that greater fluorination would be expected to increase oxidative stability and all organosilicon nitriles expected to have relatively low oxidative stability; however, unexpected, linear sweep voltammetry showed greater oxidative stability of organosilicon nitriles compared to carbonates and a higher oxidation potential for organosilicons with lower fluorination. We show that the presence of a peak in the voltammetry at a voltage lower than the full electrolyte breakdown that is associated with a surface-limited reaction may be key to providing oxidative protection in these electrolytes. Evidence in the NMR that the prebreakdown peak is associated with a coupled fluorination-oxidation resulting in Si-C bond cleavage to form a fluorosilane in solution, simultaneous formation of a surface film containing nitrogen, suggest a self-limiting surface film forms at moderate oxidizing potentials in organosilicon nitriles that promotes superior oxidative stability. These results show promise for organosilicon nitriles containing 0-1 fluorines at the silicon for applications in high-voltage battery electrolytes. Important next steps towards furthering our molecular-level understanding of the electrochemistry of organosilicon electrolytes would include expanding these studies into battery-relevant systems such as oxidation studies against complex metal oxides. Additionally, an

important complementary work on the electrochemical stability of organosilicons would be to investigate their mechanisms of reduction. Finally, the evidence that organosilicons can react to form an oxidatively-induced protective film suggest that the organosilicon structure may be easily tuned to be an intentional film-forming additive to provide additional oxidative stability.

Finally, we investigated the nature of lithium solvation in mixed organosilicon-carbonate electrolytes. We found by both NMR and FTIR that both of the carbonates studied seem to form a greater percentage of the solvation shell relative to the organosilicon. However, the presence of the organosilicon causes a greater degree of ionic dissociation, and the organosilicon appears to prefer a smaller solvation shell, suggesting that the impact of solvation is not limited simply to the majority solvent within the primary solvation shell. Future studies on organosilicon solvation will include more complex systems including ternary and additive-containing electrolytes, as well as investigations using *in situ* FTIR techniques to understand how the solvation shell changes at the electrode-electrolyte interface and under applied potentials.

This work provides a fundamental understanding of the thermal, oxidative, and solvation properties of novel organosilicon-containing lithium-ion electrolytes, that can now be used as a foundation to design better organosilicons and understand their properties in more complex and realistic battery environments.